LABORATORY VALIDATION AND INITIAL FIELD EVALUATION OF A VIBRATION-BASED TECHNIQUE FOR CONDITION ASSESSMENT OF TIMBER UTILITY POLES

by

Steven Dulin

A thesis submitted to the faculty of
The University of North Carolina at Charlotte
in partial fulfillment of the requirements
for the degree of Masters of Science in
Civil and Environmental Engineering

Charlotte

2018

Approved by:

_____
Dr. Matthew J. Whelan

_____
Dr. David Young

_____
Dr. Nicole Braxtan

ABSTRACT

STEVEN DULIN. Laboratory Validation and Initial Field Evaluation of a Vibration-Based Technique for Condition Assessment of Timber Utility Poles. (Under the direction of DR. MATTHEW J. WHELAN)

Timber is the most common material used for the utility poles that support the transmission and distribution lines of the electrical grid in the United States. Timber is well-suited for use in utility poles but is subject to decay from fungi and other organisms, particularly in the area directly beneath the ground line where the high moisture and oxygen levels provide an environment suitable for the growth of these organisms. Utilities develop pole inspection and maintenance programs in order to extend the lifespan of decayed but serviceable poles through the addition of reinforcement and remedial treatment as well as identify poles that are unfit for service and present a danger of immediate collapse, resulting in interruptions in service and costly emergency repairs. Severely decayed poles also create an occupational hazard for the utility workers who climb the poles to perform maintenance on the electrical and telecommunications infrastructure supported above. Conventional inspection methods used by maintenance workers to identify decay in poles rely on a combination of visual inspection and crude nondestructive evaluation that is limited in identifying decay below ground. Recently, a nondestructive test method that utilizes natural frequency measurements of a utility pole along with parameter identification of a physics-based Rayleigh-Ritz model and through a genetic algorithm and local gradient optimization. In this thesis, the method is validated on a second set of laboratory poles, and an initial assessment of the method in field conditions is performed on a set

of five poles. Additionally, the performance of the method is evaluated in the laboratory on poles encased in asphalt. Refinements to the method are explored, including a weighted objective function recommended to reduce error caused by the uncertainty associated with the estimation of higher frequencies in the measured bandwidth. Additionally, independent vibration measurements from two orthogonal axes are used instead of an average response in order to evaluate the ability of the method to locate asymmetric patterns of decay. Decay in the poles is characterized through destructive testing in order to evaluate the performance of the method in these laboratory and field scenarios. A first-generation prototype utilizing a MEMS accelerometer interfaced with a single-board computer is developed to record vibration measurements, and the performance of the prototype is evaluated. Recommendations for future iterations of the device and strategies for field implementation and refinement of the condition assessment algorithm are presented.

ACKNOWLEDGMENTS

The completion of this thesis would not have been possible without support from a number of individuals and groups. I would like to thank my advisor and committee chair, Dr. Matthew J. Whelan, for the opportunity to work on this research effort and for the high standard of quality that he has demonstrated and expected throughout my graduate research assistantship. I appreciate his teaching and the time and effort he has put into guiding the development of this thesis. I would like to thank Mr. Mike Moss and Dr. Youngjin Park for their assistance in performing the required experimental work for this thesis. Their knowledge and flexibility were instrumental in the completion of this work. I would like to thank my committee members, Dr. David Young and Dr. Nicole Braxtan, for their review of my thesis and their suggestions for revisions. I would like to recognize Duke Energy for their financial assistance and for their interest, support, and engagement throughout my research experience. In particular, I would like to thank Mr. Jerry Ivey for his invaluable support and guidance. I would like to thank the Energy Production and Infrastructure Center (EPIC) at University of North Carolina at Charlotte for the use of the Structural High Bay Laboratory. The performance of this research would not be possible without this excellent facility. I would like to thank my lab mates in the Experimental Dynamics and Structural Health Monitoring Laboratory for their companionship and for their part in making my research an enjoyable endeavor. Finally, I would like to thank my family and friends who give me the love and support that make my achievements possible.

TABLE OF CONTENTS

LIST OF FIGURES

LIST OF TABLES

CHAPTER 1: INTRODUCTION

Timber is the most common material used in the poles that support electrical infrastructure and above ground utility lines. There are an estimated 160 to 180 million timber poles supporting the electrical transmission and distribution systems in the United States. These systems can represent up to 40% of a utility's net value (Mankowski et al., 2002). The structural integrity of these timber poles is critical to the operation of utility lines and resilience of the nation's electrical grid to natural hazards. The unexpected collapse of a utility pole can impact customers, cause interruptions in service and the need for costly repairs, and endanger the lives of utility workers who routinely climb timber poles to perform maintenance on the supported electrical infrastructure.

The National Electric Safety Code (NESC) specifies that a timber utility pole must retain 2/3 of its original design strength to remain in service (Rural Utilities Service, 2013). Utilities must regularly inspect and maintain pole systems, and they must remove and replace poles that have declined below the strength requirements specified by the NESC (Rural Utilities Service, 2013; Morrell, 2008; Mankowski et al., 2002). Decay in the cross section of the pole is the primary reason for the removal of timber poles from service (Morrell, 2008). Decay and other damage to the cross section are typically classified into one of five categories: shell rot, pocket rot, heart rot, ring shake, and checking (Figure 1.1). Shell rot is decay that develops in the outer

layers of the cross section of the pole. Pocket rot is decay that develops within the cross section. Heart rot is a special case of pocket rot where the decay develops in the heartwood of the pole. Ring shake occurs when the growth rings of the pole separate from each other. Checking occurs when the sapwood of the pole shrinks around the heartwood of the pole, causing radial cracking from the outer surface to the center of the cross section. Shell rot and shake are of particular concern, since these forms of damage compromise the outer layers of the cross section of the pole, and therefore, have a dramatic effect on the bending strength of the pole. Checking does not have a significant direct effect on the bending strength of timber poles (Wood et al., 1960).

(a) **(b)** **(c)** **(d)**

FIGURE 1.1: Common types of cross section damage: (a) shell rot (b) pocket rot (c) shake (d) checking; heart rot not pictured

The area of a timber pole just below the ground line is at the highest risk of damage from decay, since it is in this region where conditions favorable to decay-causing fungi and organisms are most likely to exist (Birtz, 1979). Timber poles are treated with preservatives such as creosote, pentachlorophenol (Penta), and chromated copper arsenate (CCA) prior to installation to provide protection from decay. Pole inspection and maintenance programs are designed to extend the service life of timber poles by identifying poles with moderate decay in need of remedial treatment. Conventional

inspection methods typically employ a combination of visual examination, sounding and boring, and excavation to assess the condition of in-service poles (Birtz, 1979). These methods are limited in their ability to accurately identify and quantify decay in timber utility poles below the ground line and can even accelerate decay by providing a pathway for microorganisms to enter the cross section. Furthermore, due to the large number of poles in service, the inspection of poles occurs only on a basis of roughly once every eight years, which leaves poles with defects vulnerable to continued deterioration in the interim.

Structural vibration can be used to determine the material properties of timber without destroying the test specimen (ASTM, 2015; Piter et al., 2004; Chui et al., 1999; Franklin et al., 1990). Recently as part of a study preceding this work, Barber (2016) explored thermal imaging, acoustic resonance, guided wave methods, and structural vibration as potential techniques for employment in a low-cost, portable device used to assess the structural health of timber utility poles below the ground line. Barber (2016) concluded that structural vibration was the most promising technique for this application and began the development of a vibration-based method that utilized measured natural frequencies and a physics-based model to identify and quantify decay in timber poles below the ground line.

1.1 Overview of Research Effort and Anticipated Contributions

This study is part of a Phase II effort that continues upon the work of Barber (2016) in the development of a low-cost, portable device that can quickly and ac-

curately assess the condition of timber poles below the ground line. The purpose of this study is to validate the vibration-based method developed in Barber (2016) through laboratory testing of an additional set of ten poles. The full scale poles removed from service are embedded in a geotechnical test pit and vibration testing is conducted to experimentally determine the natural frequencies of the poles. The Rayleigh-Ritz physics-based model developed in Barber (2016) is calibrated using an optimization scheme to develop analytical natural frequencies that are correlated with the experimentally measured natural frequencies to identify a solution for the modulus of elasticity of the pole, an elastic stiffness parameter for the soil, and a decay parameter that models section loss as uniform shell rot spanning the region of the pole located 6 to 18 inches below the ground line. The performance of the method is evaluated by comparing the predicted values of decay with the actual decay in the poles obtained through destructive testing and classification of the cross sections below the ground line. In addition to this laboratory validation, a series of contributions are sought to assist in translating the methodology to use in the field. A first-generation prototype of a low-cost and portable condition assessment device to perform the vibration testing is developed, and the performance of the prototype is evaluated through laboratory testing. The prototype utilizes a MEMS sensor interfaced with a single-board computer to measure and record vibrations and is capable of wireless communication with the end user during the testing routine. The performance of the method in predicting decay in poles encased in asphalt is also explored to identify potential challenges associated with applying the methodology under this condition encountered in the field. A three to five inch layer of hot mix asphalt is

placed in the test pit to encase the set of timber poles at the ground line. The previously described condition assessment procedure is repeated on the poles encased in asphalt, and the performance of the method is evaluated through comparison with the results of the initial laboratory validation testing. Finally, an initial evaluation of the ability of the method to produce accurate natural frequency estimates from vibration measurements of in-service poles is performed. A field validation procedure is developed, and poles scheduled for immediate removal are tested. The frequency spectra and estimated natural frequencies of the poles are analyzed to evaluate the reliability of the vibration measurements.

1.2 Thesis Outline

The outline of this thesis is as follows:

- Chapter 1 provides an introduction to the challenges associated with the in-service inspection of timber utility poles and summarizes the scope of the thesis contributions.

- Chapter 2 presents a literature review on the use and assessment of timber distribution poles, provides an overview of the principles of vibration-based damage identification methods, and summarizes the method developed in Barber (2016) to identify and quantify decay in timber utility poles below the ground line.

- Chapter 3 details the development and performance evaluation of a first-generation prototype to measure and record vibration measurements for the condition assessment routine using a MEMS accelerometer interfaced with a single-board

computer.

- Chapter 4 details the laboratory validation of the method developed in Barber (2016) on a second set of timber poles embedded in a geotechnical test pit. The performance of the method is evaluated for poles in nominally equivalent conditions to those in Barber (2016) and on the same set of poles encased at the ground line with a three to five inch layer of asphalt. Several improvements to the original methodology are suggested and evaluated.

- Chapter 5 provides an initial evaluation of the ability of the method to provide accurate estimates of natural frequencies from vibration measurements of in-service poles. A field testing procedure is developed and documented. The performance of the method is assessed based on qualitative characterization of the condition of the poles below ground.

- Chapter 6 summarizes the conclusions of the study and provides recommendations for the future refinement of the vibration-based condition assessment technique and development of a low-cost and portable device to facilitate field use.

CHAPTER 2: LITERATURE REVIEW

2.1 Timber Poles in Electrical Distribution Networks

Timber poles are commonly used to support electrical infrastructure and above ground utility lines. There are an estimated 160 million to 180 million timber poles supporting the electrical transmission and distribution systems in the United States. These systems can represent up to 40% of a utility's net value (Mankowski et al., 2002). The structural integrity of utility poles is critical to the operation of utility lines. Utility poles are connected in series by conductors, and the failure of one pole can lead to the collapse of other adjacent poles (Datla and Pandey, 2006). Failures of poles can cause interruptions in service along the supported utility lines, resulting in impacted customers and costly emergency repairs (Mankowski et al., 2002).

Utility poles are comparable to cantilever beam-columns that are required to resist both axial and flexural loads. Utility poles support electrical infrastructure including conductors, transformers, and insulators that contribute significant gravity loads. They may support additional infrastructure, such as phone and internet lines or luminaires. Utility poles must also resist environmental loads, including wind, ice, and live loads during installation, inspection, and maintenance (Datla and Pandey, 2006). Timber is the most common material used for utility poles. Common alternative materials to timber are galvanized steel, reinforced concrete, fiberglass, and laminated

wood (Mankowski et al., 2002). Timber is well-suited for use as utility poles, since it is cost effective and not subject to fatigue or corrosion concerns like galvanized steel or concrete (Birtz, 1979). Southern yellow pine accounts for approximately 69% of in-service timber utility poles, while other species that are in widespread use for this purpose are Douglas fir (15%) and western red cedar (13%) (Mankowski et al., 2002). Timber is an orthotropic material; the material properties are primarily dependent on the orientation of the wood grain that runs along the length of the pole (FHWA, 2007). In one study, the elastic modulus of southern yellow pine was measured in directions parallel and perpendicular to the wood grain. The compressive modulus of elasticity in the direction parallel to the grain was determined to be 16,572 MPa, while the compressive modulus in the direction perpendicular to the grain was determined to be only 593 MPa (FHWA, 2007). The material properties of timber related to strength and stiffness also vary between different species, different members of the same species, and within individual timber specimens (Daugherty, 1998). The American National Standards Institute (ANSI) sets specifications and requirements for the timber used for utility poles (Rural Utilities Service, 2011; ANSI, 2017). Timber poles are typically manufactured from premium timber that is a relatively scarce resource (Birtz, 1979).

It is important for utilities to maximize the lifespan of timber utility poles. In addition to managing a scarce resource, extending the life of the timber poles results in an obvious cost savings for a utility (Morrell, 2008). Utilities tend to underestimate the lifespan of timber utility poles. A study by (Mankowski et al., 2002) indicated that most utilities estimate the service life of a timber pole to be 30 to 40 years. However, replacement rate data from Morrell (2008) suggests that the average service

life of a timber pole is actually greater than 80 years in many areas of the country. A more recent study reports that timber poles have an average life expectancy of 69 years (Datla and Pandey, 2006). Morrell (2008) explains that the perceived low lifespan of timber poles in the utility industry is likely based on data intended to estimate the economic lifespan of a pole, i.e. the point at which a pole meets its return on investment. Extending the service life of a pole beyond this point results in an potentially significant cost savings for the utility.

2.1.1 Decay in Timber Utility Poles

Poles may be removed from service for a variety of reasons (Figure 2.1). Decay is the primary reason and the most critical since it is associated with loss of cross section that reduces the stiffness and strength of the pole. Decay in utility poles is typically classified into one of three categories: shell rot, pocket rot, and heart rot. Shell rot is cross sectional loss in the outermost layer of the pole. Pocket rot is cross sectional loss enclosed within the cross section. Heart rot is a specific type of pocket rot that occurs in the center of the cross section. Shell rot is the type of decay that

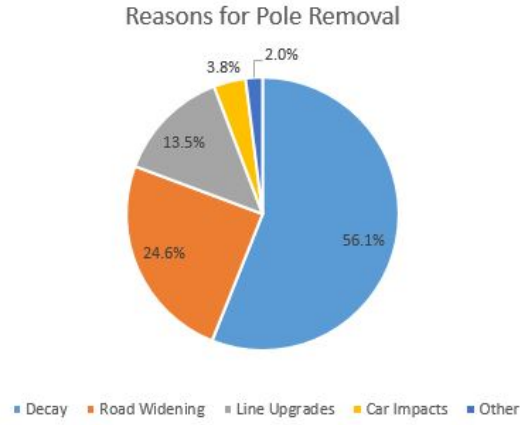

FIGURE 2.1: Reasons for pole removal (Morrell, 2008).

is most debilitating to the flexural strength of a pole and is, therefore, the type of decay that is typically of most concern. The effects of shell rot and heart rot on the sectional properties of a circular cross section are shown in Figure 2.2. As the size of the damaged area in a cross section increases, the cross sectional area and second moment of area of a pole decrease rapidly due to shell rot. The strength of the pole falls below design strength requirements when decay affects just 10-20% of the radial dimension of the cross section of the pole. Heart rot, by contrast, must affect 55-60% of the radial dimension of the cross section in order to reduce the strength of a pole below design requirements.

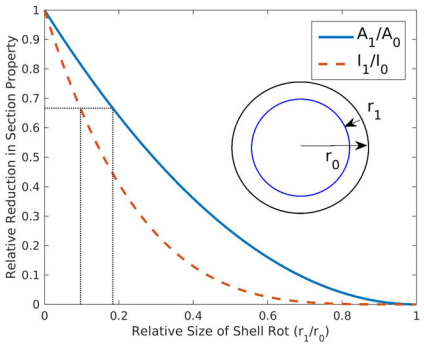

(a)

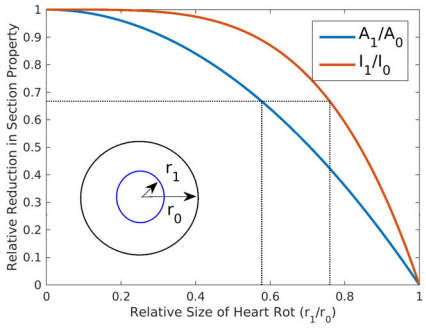

(b)

FIGURE 2.2: Relative reductions in cross sectional area and moment of inertia associated with decay. a) Shell rot; b) Heart rot

The area of a pole just below the ground line is at the highest risk of damage from decay, since it is in this region where decay-causing fungi and organisms are most likely to exist (Birtz, 1979). The microorganisms responsible for decay in timber utility poles prefer warm, wet environments. As a result, decay tends to occur most rapidly in regions with hot, humid climates. The USDA Rural Utilities Service defines Decay Severity Zones according to temperature, humidity, and pole performance data.

These zones are shown in Figure 2.3. Decay in timber poles is most severe in the southeastern United States, particularly in areas adjacent to the Atlantic and Gulf coasts and Hawaii (Rural Utilities Service, 2013; Morrell, 2008).

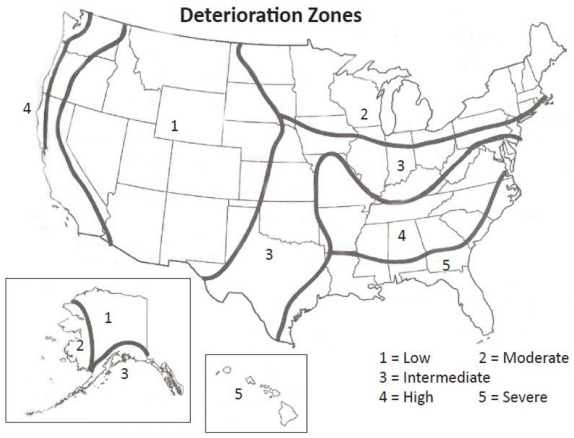

FIGURE 2.3: Decay severity regions as classified by the American Wood Protection Association (Morrell, 2008)

Preservative treatment helps protect timber utility poles from decay. Without preservative treatment, poles made of thick sapwood species, such as southern yellow pine, would deteriorate to the point of failure within two to three years after installation in some parts of the country (Rural Utilities Service, 2013). Preservative treatment extends this lifetime expectancy by mitigating the conditions favorable to decay-causing fungi and organisms. During the first half of the 20th century, pressure treatment with creosote was the primary preservative treatment used for thick sapwood species (Birtz, 1979). Creosote shortages following WWII led to the development and use of other preservation treatments, such as pentachlorophenol (Penta) and chromated copper arsenate (CCA). Penta is now the most widely used preservative treatment for timber utility poles (Rural Utilities Service, 2013). According to a survey performed in 1997, nearly 63% of the 42 million in-service poles owned

by the 244 utility systems surveyed were originally treated with pentachlorophenol compared to 16% for creosote and 16% for chromated copper arsenate (Mankowski et al., 2002). The American Wood Protection Association (AWPA) specifies the requirements for preservative treatment of timber utility poles (Rural Utilities Service, 2013). Adhering to these standards can help maximize the service life of timber poles (Morrell, 2008).

2.1.2 Pole Inspection and Maintenance Programs

Regular inspection of poles provides an economic benefit to the utility by identifying poles with moderate decay that are still serviceable. Serviceable poles contain a large portion of completely sound wood. These poles have strength that is above minimum code requirements but may be in early stages of decay (Rural Utilities Service, 2013). Arresting this decay with remedial treatments can extend the life of these poles and reduce service interruptions and costly emergency replacements. Some remedial treatments involve applying a chemical compound to the exterior surface of a pole. Other treatments seek to arrest internal decay through the use of chemical rods or fumigants inserted with force into the cross section (Mankowski et al., 2002). Serviceable poles with decay are treated to 18" below the ground line. Remedial treatments can extend the service life of timber poles by up to 60% (Morrell, 2008). Lengthening the service life of utility poles reduces the costs associated with electrical transmission and distribution (Birtz, 1979; Morrell, 2008). Pole asset management programs and service life estimates are often based on outdated or incorrect information (Mankowski et al., 2002). As a result, in the absence of regular inspections, utilities miss out on

the potential cost savings from reliable identification of poles with moderate decay. Information gathered during inspections can be used to inform future planning for pole maintenance and condition monitoring (Rural Utilities Service, 2013).

The National Electric Safety Code (NESC) specifies the conditions under which a timber pole is deemed fit for continued service (Rural Utilities Service, 2013). According to this code, a timber utility pole must retain 2/3 of its original design strength, except for when it must maintain 3/4 of its original design strength when installed to resist loads from extreme wind or extreme ice with wind. Reduced pole strength is based on a reduced circumference calculated from various types of cross section loss. Utilities must regularly inspect and maintain pole systems, and they must remove and replace poles that have declined below the strength requirements specified by the NESC (Rural Utilities Service, 2013; Morrell, 2008; Mankowski et al., 2002).

A typical pole inspection and maintenance program has three major components: periodic inspection of poles, remedial treatment of serviceable poles, and removal and replacement of reject poles. The Rural Utilities Service (RUS) makes several recommendations on how these programs should be developed and executed. Spot checking is an initial step that can help a utility develop a program that meets its specific needs. By sampling various continuous groupings of 50 to 100 poles, a utility can identify areas of rapid decay and can adjust its installation, inspection, and maintenance practices accordingly (Rural Utilities Service, 2013). Utilities should perform periodic inspections to monitor the condition of their poles. An eight to ten year inspection cycle is recommended for zones of rapid decay, such as the southeastern United States. A ten to twelve year cycle is recommended in areas where the risk

of decay is lower. In Mankowski et al. (2002), utilities reported an average period between inspections of 7.2 years for transmission poles and 8.1 years for distribution poles. Inspections, in this case, ranged from visual observation to a complete sound and bore with excavation.

Conventional methods for pole inspection, their approximate cost, and effectiveness are summarized in Table 1 (Birtz, 1979). Most utilities use a combination of these methods to monitor the condition of their poles (Mankowski et al., 2002). These methods vary both in their cost and in their reliability in determining poles with moderate to severe decay. Visual inspection is an initial step during the condition assessment process that is useful for correctly identifying obvious defects above the ground line, including splitting, woodpecker damage, and overload at the supports for electrical infrastructure. Pairing visual inspection with sounding and boring is the most common practice for condition assessment of poles. Sounding consists of striking the pole with a 3 lb hammer in a variety of locations that are within arm's reach of the inspector. Striking a location with a solid, healthy cross section produces a sharp, clear sound. Additionally, the hammer responds to the strike with a strong rebound off the wood. When a void exists in the cross section, a hammer strike produces a dull sound and the hammer exhibits a dead response to the impact. An experienced inspector can detect these changes in sound and hammer response and infer that a void exists in the cross section at or near that location (Rural Utilities Service, 2013). Boring consists of drilling into a pole to take a sample of the wood. An experienced inspector can judge the condition of the wood by observing the level of resistance encountered by the drill. The shavings can also be examined to determine

the health of the drilled area. These shavings can be further analyzed to measure preservative penetration and retention. Visual inspection along with sounding and boring can identify most poles that are in immediate danger of collapse but can only detect 50-60% of reject poles (Birtz, 1979). Additionally, this method does a poor job of identifying serviceable poles with moderate decay whose lifespans can be extended with remedial treatments. In southern yellow pine, decay typically starts below ground before progressing inward through the cross section and then upward through the length of the pole into areas above the ground line. By the time decay is detected in a pole using the sound and bore technique, the pole may be deteriorated beyond repair and could even be on the verge of catastrophic failure (Rural Utilities Service, 2013). Consequently, the sound and bore method is more effective when coupled with a partial or full excavation. Excavation allows an inspector to perform the sound and bore technique on regions of the pole that are below the ground line. A partial excavation involves removing one or two shovelfuls of soil from around a portion of the circumference of the pole. In a full excavation, the inspector removes six to eight inches of soil from around the entire circumference of the pole. Excavation exposes the area of the pole where decay is most likely to occur. The practice of visual inspection along with partial excavation and sounding and boring of poles can identify 80-90% of poles in need of replacement. Full excavation increases this success rate to 90-95%. A combination of visual inspection, full excavation, sounding and boring, and ground line treatment is currently the most reliable pole inspection method, capable of identifying 99% of rejects and extending the life of the pole. However, visual inspection, full excavation, sounding and boring, and ground line treatment is the

TABLE 1: Comparison of conventional inspection practices, reproduced from Birtz (1979)

Type of Inspection	Approx. Cost/Pole	Remarks
Visual & Sounding	$0.75	Almost worthless. Even misses danger poles. Does nothing to maintain poles.
Visual, Sound & Bore	$2	Finds 50-60% of reject poles and most danger poles. Does nothing to maintain poles.
Visual, Partial Excavate, Sound & Bore	$2-4	Finds 80-90% of reject poles. Fair inspection but does not prolong life of poles.
Excavate 6-8" around entire circumference, inspect and treat to 18" all poles with decay or defects	$6-7	Finds 90-95% of reject poles. Good inspection and most poles that would fail early are treated.
Visual, Excavate, Sound & Bore, and Groundline Treat	$8-12	Finds 99% of reject poles. Extends life of poles.

most expensive inspection method, costing approximately $8-12 per pole according to a study performed in 1979 (Birtz, 1979).

In addition to potentially being time consuming and expensive, conventional inspection methods are also intrusive and potentially destructive to the pole. Boring creates a pathway for excess moisture and microorganisms to enter the internal cross section of the pole. Excavation can increase the risk of future decay by removing the preservative protection that exists in the soil adjacent to the surface of the pole and replacing it with fresh soil (Morrell, 2008).

2.2 Vibration-Based Nondestructive Methods for Pole Condition Assessment

Numerous methods and commercial devices have been developed that claim to be able to assess the structural health of a timber pole. These approaches are based

on a variety of techniques, including sonic wave propagation (Krause et al., 2015), ultrasonic wave propagation (Krautkrämer and Krautkrämer, 2013), guided wave propagation (Kim et al., 2000; Yan, 2015), and acoustic resonance (Craighead et al., 2001). Utilities have been hesitant to incorporate these devices into their inspection programs. It is unclear if this is due to conservatism within the industry, poor performance of the available devices, or added cost and time necessary to perform such techniques (Mankowski et al., 2002). Since this thesis focuses exclusively on a vibration-based approach for nondestructive evaluation of timber poles, the remainder of the literature review will focus on the use of structural vibration to perform structural condition assessment.

Structural vibration can be used to determine the material properties of timber. ASTM E1876 details the method for using vibration from a single impulse excitation to determine the dynamic modulus of elasticity, dynamic shear modulus, and dynamic Poisson's ratio of elastic material specimens (ASTM, 2015). The method is a simplified approach to direct model updating, where the equations for the natural frequencies of a continuous system model of the test specimen geometry are rearranged to solve for the dynamic material properties as a function of the measured dimensions, mass, and natural frequency. The dynamic modulus of elasticity is proportional to the square of the measured natural frequency for the fundamental longitudinal mode and the fundamental flexural mode. Likewise, the dynamic shear modulus is proportional to the square of the measured natural frequency of the fundamental torsional mode. When applied to timber, the orientation of the grain of the wood must be considered since the material is anisotropic. Through a similar method, Piter et al.(2004) de-

termined the elastic properties of structural sizes of Argentinean *Eucalyptus grandis* and found that the approach was effective in determining the dynamic modulus of elasticity in specimens across a wide variety of conditions. Chui et al. (1999) used a transverse vibration technique to determine the modulus of elasticity of tapered timber utility poles and found that values obtained through this method correlated strongly with those determined through static bending tests. Franklin et al. (1990) developed a method that extends the approach used in ASTM E1876 (2015) to quantify decay in a tapered pole embedded in soil. A rotational spring is used to model the supporting soil and potential decay in the embedded portion of the pole. An actual tapered pole is excited to produce measurements of at least two of the first five natural frequencies. An optimization scheme is used to adjust the spring constant and the taper of the pole until the natural frequencies of the model closely match those measured experimentally. The spring constant represents the resistance offered by the soil and the pole, and a lower than expected value is taken to be indicative of decay in the embedded portion of the pole.

2.3 Use of Rayleigh-Ritz Method and Model Updating to Quantify Decay in Utility Poles Below the Ground Line

In the study most relevant to the current work, Barber (2016) performed non-destructive testing on timber utility poles embedded in a full-scale experimental test bed to identify reliable methods for assessing the condition of timber poles below the ground line. One method that showed promise for use in a low-cost, rapid, and portable device for the condition assessment of timber utility poles utilized the mea-

surement of structural vibrations following impulse excitation with modal analysis to extract the natural frequencies corresponding to the first six to eight bending modes of the poles. A physics-based model of a tapered pole supported in an elastic soil was developed to analytically predict the expected natural frequencies for the bending modes using the Rayleigh-Ritz Method. An iterative process of model updating through global optimization was used to identify values for an unknown set of parameters in the physics-based model such that the analytically predicted frequencies most closely matched those measured experimentally. Among this set of unknown parameters were the elastic stiffness of the timber, the elastic stiffness of the soil, and a decay parameter modeling loss of pole volume below the ground line due to shell rot. When applied to the experimental dataset, the identified decay parameter strongly correlated with the actual decay below the ground line in the 10 poles tested. A more detailed summary of this method is given below, since the current study is an extension of this work.

The Rayleigh-Ritz Method is an extension of the Rayleigh Method. Both methods use conservation of potential and kinetic energy and an assumed mode shape to solve for the natural frequency associated with that mode shape (Tedesco, 1998). While the Rayleigh Method uses a fixed mode shape for each mode, the Rayleigh-Ritz method specifies each mode shape, $\Phi_j(x)$, as a finite series of basis functions, $\phi(x)$, through $\Phi_j(x) = \sum_{i=1}^{h} c_{i,j}\phi_i(x)$. This extended method results in a more accurate estimation of the mode shapes and associated natural frequencies of the system, especially for higher order bending modes. Following the recommendations in Ilanko and Monterrubio (2015), Barber (2016) used first and second order polynomial basis functions

as well as sinusoids for the higher order terms. A total of 250 basis functions were used to develop the Rayleigh-Ritz model using precalculated integrals in a MATLAB routine to provide for solution of natural frequencies of the model in approximately 1/20 of a second.

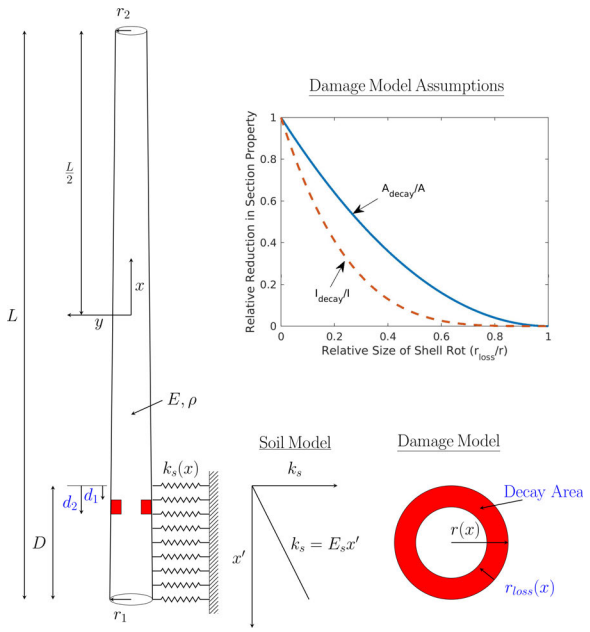

FIGURE 2.4: Rayleigh-Ritz Model with decay parameter, DP (Barber, 2016)

The Rayleigh-Ritz Method is suitable for application to continuous system models, which may contain elastic structural elements, distributed or concentrated springs, and distributed or concentrated masses. Consequently, the method is suitable for application to a range of structural systems and can be adapted to address various boundary conditions and supported masses. This flexibility in the methodology will ultimately be leveraged to extend the basic model to more representative field conditions with supported infrastructure, guy wires, or encasement. Barber (2016) used the model depicted in Figure 2.4 to represent a tapered pole of homogeneous material embedded in an elastic soil with stiffness increasing linearly with depth. In this

model, the length (L), radius ($r(x)$), mass density (ρ), embedment depth (D), and region of potential decay (d_1 and d_2) were treated as known. Decay in the model was assumed to be located in the region 6 to 18 inches below the ground line, which reflects the higher likelihood that decay, if present, will be located in the region of the pole just below the ground line. The set of unknowns consisted of the elastic modulus of the pole (E), the elastic spring constant for the soil (Es), and a decay parameter (DP). In this model, damage was modeled as uniform, exterior cross section loss throughout a specified region below the ground line. This idealized representation of decay mimics typical shell rot losses. In the Rayleigh-Ritz model the decay parameter was calculated as the change in cross sectional area (dA) divided by the original cross sectional area (A). Through this normalization, a decay parameter of zero indicates no section loss while a decay parameter of one would indicate complete section loss. Assembly of the mass (M) and stiffness (K) matrices for the pole-soil model accounted for the decay in the specified region through the associated loss in mass and stiffness.

Analytical natural frequencies were calculated through eigenvalue decomposition of the mass and stiffness matrices of the parameterized Rayleigh-Ritz model, and an objective function was developed to score the model based on the difference between its predicted natural frequencies and those measured experimentally (Figure 2.5). To optimize the model correlation, a genetic algorithm was used to determine the optimal set of assignments for the unknown parameters in the model, including the decay parameter. The genetic algorithm is an iterative approach to solving the parameter identification problem for global optimization of the unknown parameters. The ge-

netic algorithm used a population of 100 individuals, an elite count of 5 individuals, and a cross-over rate of 60%. A fixed stopping criteria of 24 generations was used to terminate the genetic algorithm at the identified values for the unknown parameters E, E_s, and DP within a bounded range of plausible values.

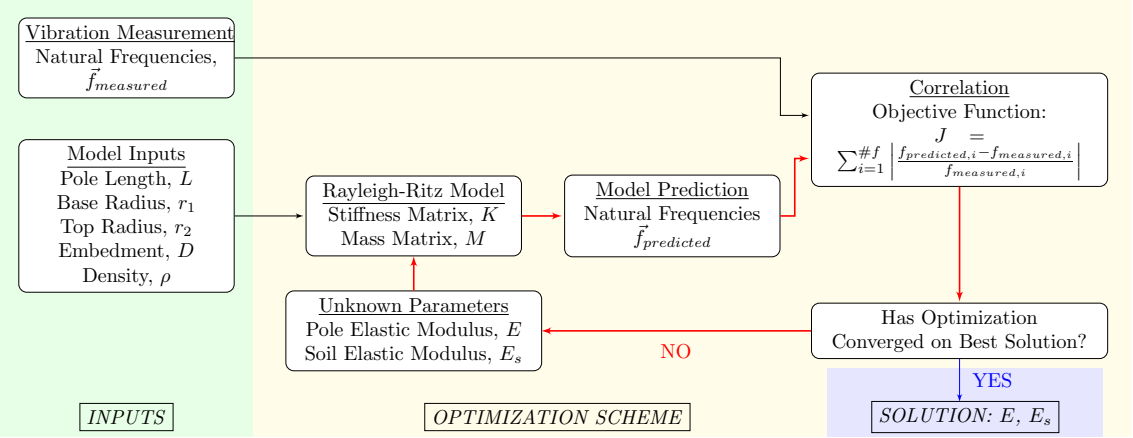

FIGURE 2.5: Parameter identification scheme (Barber, 2016)

A parameter identifiability study was performed in the study to ensure uniqueness in this inverse problem and determine the effectiveness of using model updating of the Rayleigh-Ritz model to in identify the unknown parameters, E, E_s, and DP. In this parameter identifiability study, randomly assigned values for these unknown parameters were entered into the model in order to generate synthetic natural frequency measurements. The genetic algorithm was then used to identify the unknown parameters from the synthetic natural frequency measurements. Consistently low prediction errors between the identified values and the "true" randomly assigned values demonstrated that the developed method could reliably identify the three unknown parameters, E, E_s, and DP, given limited natural frequency measurements.

Following the parameter identifiability study, the methodology was performed on

the experimental data acquired from each of the 10 poles. The approach was shown to be capable of not only identifying the presence of decay below ground, but also producing accurate estimates of the severity of decay through the decay parameter. The experimental results were validated through comparison to the actual extent of decay as measured by destructive characterization of the cross section of each pole below the ground line. All cases of healthy poles without section loss were correctly identified as having no section loss and all poles with severe decay were also correctly identified. For three poles with moderate section loss, two were correctly identified, but the third was incorrectly identified by the method as having no section loss. However, the decay in this pole was deeper than the assumed decay region, which suggests that the developed approach may be limited to detecting decay in only the region close to the ground line. Barber (2016) concluded that the method showed promise for use in a low-cost, rapid, and portable nondestructive evaluation tool for timber utility poles.

2.4 Vibration-Based Damage Detection

Determining the material properties of structural systems and their components in service has important applications for condition assessment, health monitoring, and asset management. Structural failure from unidentified damage can threaten human safety and result in economic loss. Identifying structural damage in situ provides an opportunity for repair and helps prevent sudden failure (Fan and Qiao, 2011). There are four levels of damage identification in a structure: detecting the existence

of damage, determining its location, quantifying its severity, and predicting the effect of the damage on the remaining service life of the structure (Borges et al., 2007). The effectiveness of a damage identification method depends on the goals of the effort and may also require compensation for changes in the environmental conditions, boundary conditions, and the physical and geometric properties of the structure. Researchers and practitioners approach the problem of damage identification using a variety of techniques and technologies, such as structural vibration, thermal imaging, acoustic response, wave propagation, and x-ray imaging. The purpose of these non-destructive evaluation methods is to assess the health of a structure with minimal intrusion.

Structural vibration-based methods are popular in damage identification applications. These techniques rely on the underlying physics that damage causes changes in the physical properties related to the mass and stiffness of a structure and, therefore, can be detected through analysis of the modal characteristics of the structure. Practitioners identify damage by relating experimentally measured modal properties to the unknown physical properties of the structure, including any damage that may be present (Fan and Qiao, 2011). Natural frequencies and mode shapes are the modal properties most commonly used within vibration-based damage identification techniques. Each of these modal properties comes with advantages and disadvantages related to ease of measurement, quality of information provided, and susceptibility to errors resulting from environmental conditions and sampling noise. The primary advantage associated with mode shapes is that they contain local information about the structural response making it easier to directly identify the location(s) of damage. Although sensitive to local changes in the mass or stiffness matrix, natural fre-

quencies provide no direct localized information about the structural response and, consequently, require additional information from inverse modeling of the structure in order to provide any potential to locate the damage.

Peterson et al. (2001) explored the problem of damage identification in a timber beam. Damage was introduced to one beam through saw cuts in the cross section, while another beam with natural damage due to severe decay was also experimentally measured. A finite element model was used to predict the expected mode shapes of the first two vibrational modes. Damage was located in the beam by identifying locations where there were large differences between the mode shape predicted by the model and the experimentally measured mode shape of the damaged beam. This technique performed moderately well in a laboratory setting for the beam with saw cuts, but resulted in several false positives and failed to locate the severe decay in the beam with natural damage. The beam had a short span, and the decay was near the support. Consequently, the mode shape displacements near the decay in this beam were small and did not provide accurate data for an error calculation between the measured and analytically predicted mode shape. Ultimately, the study concluded that the developed method would be impractical for field measurements due to the amount of sensors required for an accurate mode shape measurement. This is the primary disadvantage of direct damage identification methods based solely on mode shape measurements. Acquiring accurate experimental mode shape estimates requires simultaneous measurements obtained across multiple locations along the structure. This presents a practical challenge for many damage identification methods that are intended to assess the health of a structure in situ (Borges et al., 2007; Fan and Qiao,

2011).

Natural frequencies are the easiest modal property of a structure to accurately measure (Khiem and Toan, 2014). Natural frequencies can typically be measured through the use of a sensor at a fixed location. Natural frequencies are also less susceptible errors due to experimental noise than mode shape measurements, though they are more sensitive to environmental factors such as temperature (Fan and Qiao, 2011). Furthermore, natural frequency measurements typically have a low sensitivity to damage and changes from damage may be hidden by errors resulting from measurement noise and environmental effects. According to Salawu (1997), damage must cause a change of 5% or greater in the natural frequencies for damage to be reliably detected. Damage identification problems based on only natural frequencies are often ill-posed and the solution that reflects the damage location and severity of the real structure may not be unique. Knowledge of a certain number of natural frequencies is required to ensure that the correct solution is unique within the relevant domain. Borges et al. (2007) used 12 natural frequencies to identify damage in an aluminum truss composed of 26 elements, and determined that at least 10 measured natural frequencies were needed to identify damage in a three-story frame composed of 13 elements. Hassiotis and Jeong (1995) studied the number of natural frequencies required to detect damage in two different types of structures. In a 10-story, two bay steel frame, five natural frequencies were required to detect damage in floor elements of the frame and ten natural frequencies were required to detect damage in all elements of the frame except those closest to the supports. In another case, this study determined that six natural frequencies were required to detect damage in an

aluminum cantilever beam. Khiem and Toan (2014) used the first six natural frequencies to detect cracks in a beam-like structure. The number of natural frequencies needed to solve the damage identification varies depending on the complexity of the structure and the goals of the damage identification effort. Acquiring the minimum number of natural frequencies may be challenging, since in some cases it may only be feasible to excite and accurately measure the first several modes of vibration.

Although some methods have been developed to identify damage from changes in modal parameters, damage identification without a baseline measurement is more commonly approached as an inverse problem. The physical properties of a structure, including damage location and severity, are determined by correlating the predictions of a corresponding analytical model of the structure with experimental measurements of the modal properties. The majority of developed methods make iterative changes to the model until its dynamic behavior matches that of the real structure. This process is called model updating and is well summarized in Mottershead and Friswell (1993). Within the model updating process, a limited set of unknown parameters in the model are selected to calibrate the model to the measured response, with some of these unknown parameters being used to reflect the structural health. With assumed or iteratively assigned values for the unknown parameters, the analytical model can predict the same set of modal parameters measured in the vibration test. If these analytical results do not match those measured experimentally, then the assumed physical properties of the structure are changed, and the analytical results are recalculated. This iterative process continues until the correlation between the analytical and experimental results converge or no longer improve. The parameter

values within the final version of the updated model are then interpreted as the in-service physical properties of the structure.

The model updating technique has its limitations, and these are well summarized in Mottershead and Friswell (1993). Errors can reduce the effectiveness of vibration-based model updating methods, and these errors can come from several sources. The theoretical basis of the model may be incorrect, incomplete, or have important limitations in its ability to predict the behavior of the structure. Unaccounted for ambient vibrations and accelerometer cable noise can introduce error into test data. Additional error can be introduced during modal analysis from aliasing, spectral leakage, and the linearization of nonlinear effects. To improve the effectiveness of natural frequency-based methods for vibration-based damage detection, care should be taken to eliminate or reduce systematic error in both the analytical model and the experimental measurements.

Vibration-based damage identification problems are often complex and require sophisticated optimization schemes in order to find a solution that matches the damage distribution in the real structure. Genetic algorithms often serve this purpose by optimizing an objective function subject to constraints. Friswell et al. (1998) and Mares and Surace (1996) provide excellent overviews of the use of genetic algorithms for vibration-based damage detection. The optimization procedure in a genetic algorithm mimics the evolutionary processes of reproduction, chromosomal crossover, mutation, and natural selection to arrive at an optimal solution for unknown parameters in a model. First, a population of individual solution candidates is generated. Each individual is ranked according to its "fitness" through the use of an objective

function. Individuals with high fitness have a high likelihood of reproducing and sending genetic information to the next generation of candidate solutions. In the application of damage identification through model updating, the genetic information of the individuals contains the values of unknown parameters. The optimization procedure typically stops after a user-specified number of generations, at which point the genome (parameter assignments) of the individual with the highest fitness is taken as the solution to the damage identification problem. Genetic algorithms are well-suited for difficult problems where multiple local minimums or maximums may exist in addition to the global optimum. An additional advantage of genetic algorithms is their ability to simultaneously optimize both discrete and continuous variables (Friswell et al., 1998). According to Mares and Surace (1996), typical parameter values for genetic algorithms used in vibration-based model updating include a population of 20-30 individuals, a crossover rate of 0.60-0.95, and a random mutation rate of 0.01-0.02. Genetic algorithms with these parameter settings have been shown to provide adequate solutions for most problems. Mares and Surace (1996) used a population of thirty individuals, a crossover rate of 0.65, a mutation rate of 0.01, and a maximum generation number of 70 in their method to identify the location and extent of damage in a MDOF truss structure. They used an elitist version of genetic algorithm, where the most fit individual from the current generation is automatically included in the next generation without modification. This sets a standard where individuals in subsequent generations must improve upon the current best solution to be eligible as the final solution. The method was able to accurately identify the location and quantify the extent of damage in the structure, even in the case of multiple damage

locations. Furthermore, the genetic algorithm was able to arrive at the optimal solution despite the existence of experimental noise, representing an improvement over other optimization techniques.

There are many examples of studies that have pursued damage identification in structures using measured natural frequencies along with model updating. Several methods have been developed for the detection of damage in beam-like structures (Lee, 2009; Hassiotis and Jeong, 1995; Chinchalkar, 2001). Khiem and Toan (2014) developed a method for detecting cracks of unknown number, location, and depth in a Euler-Bernoulli beam with clamped ends and known values for the modulus of elasticity, mass density, length, cross sectional area, and second moment of area. Their work included the derivation of the Rayleigh quotient for a model of the structure to develop an explicit expression for the natural frequencies of the beam. Initially, a certain number of cracks of unknown magnitude were assumed to exist at a user-specified mesh of locations in the beam. A model of the beam was constructed based on these crack locations and the geometric and material properties of the beam. The method then used the measured natural frequencies to determine the crack depth, i.e. severity of damage, at each of these assumed locations. Mesh locations with positive magnitudes were selected as the new mesh of crack locations, and the crack magnitudes were recalculated across this new set of locations. These steps were repeated to iteratively locate and quantify the damage in the beam, with the process terminated when the natural frequencies of the model match the measured natural frequencies of the structure within a certain tolerance. The method performed well for a variety of distributions of small cracks in numerical and experimental examples.

The method was less effective for larger cracks damaging 30% of the cross section of the beam.

As previously mentioned, damage identification problems are often ill-posed, meaning that the solution that represents the damage distribution in the real structure may not be unique. Improving the performance of genetic algorithms requires limiting the search space to realistic values. Using domain knowledge to constrain or eliminate unknown parameters helps improve the effectiveness of damage identification methods by giving greater consideration to values that make physical sense. Similarly, constructing and constraining a suitable model can help bias the search away from solutions that have no physical meaning. One common constraint in damage identification problems limits the number of damage locations to a small number. A real structure is typically damaged in, at most, only a few locations. An optimization scheme should only search for solutions that fit this realistic behavior and disregard solutions that show damage to occur in many locations. Friswell et al. (1998) added a penalty to the objective score of individuals with multiple damage locations, lowering the fitness of these individuals and effectively selecting against this "trait." In Borges et al. (2007), the initial population was generated so that each individual was damaged in only a single location, biasing future generations towards a low number of damage locations. This study also tested additional modifications to a typical genetic algorithm to develop an optimization procedure better suited for the application of damage identification. First, the continuous variable representing loss of stiffness due to damage was changed to a discrete variable with a user-specified domain. This allowed the user to leverage knowledge of the particular structure to bias the search

away from unrealistic damage distributions. Second, mutation operators were applied only to elements that were identified as damaged, creating subtle variations around individual genotypes that were already likely to have high levels of fitness. In this study, the modified genetic algorithm was applied to the damage identification problem explored in Mares and Surace (1996). The method was still unable to identify damage with natural frequencies alone but performed better than the original algorithm that used a combination of natural frequencies and incomplete mode shape data. The method was also tested after noise was introduced into the measurements. While the genetic algorithm still performed well in identifying a global minimum, the noise created solutions in the search space with higher fitness than the solution that best represented the real structure. This result demonstrates the importance of minimizing measurement noise in vibration-based damage identification methods and realizing that the identified parameters will have uncertainties that are affected by the measurement noise and sensitivity of the modal parameters to the noise. Furthermore, the effectiveness of these methods depends on development and use of a model that accurately reflects the underlying mechanics of the structure as well as an effective search algorithm for the parameter identification.

CHAPTER 3: DEVELOPMENT AND PERFORMANCE TESTING OF PROTOTYPE SENSOR

This chapter reports the development of a first generation prototype for a device that utilizes structural vibration to assess the condition of timber utility poles. This device is required to be low-cost, portable, easily operable, and capable of accurately measuring and recording vibration measurements. Natural frequencies extracted from these measurements can be used along with the semi-automated routine developed in Barber (2016) to identify subsurface decay in a utility pole, if present. The first generation prototype is composed of a low-cost MEMS accelerometer that communicates to a single-board computer via a two-wire serial (I^2C) communication bus. The assembly is powered by a lithium polyion battery and encased in a 3D-printed case with curved attachment surface and strap loop for securing the device to the outer surface of a utility pole. The prototype establishes a local wireless network and can be controlled through Secure Shell (SSH) networking on a laptop or smartphone. A user-friendly pole condition assessment routine was written in C and can be run on the prototype in order to record vibration measurements. Direct comparisons with reference measurements recorded with a commercial data acquisition system reveal that the accuracy of the sampling clock within the wireless prototype, and consequently the natural frequency estimates, requires calibration. A method is established to correct the rate of the sampling clock to match that of the high-end

commercial reference system. Measurements obtained by the prototype on a set of ten poles embedded in a laboratory test pit are then compared to those obtained with the reference system.

3.1 Prototype Hardware

The first generation prototype utilizes a Raspberry Pi Zero W single-board computer as the microprocessor to communicate over a WiFi network with the end user and interface with the sensing hardware. The Raspberry Pi Zero W is equipped with a 1 GHz single-core CPU and 5.2 MB of RAM. The open source Raspian Jessie operating system was installed for the development of this prototype. The computer has a Micro-USB power supply, but an off-the-shelf power management circuit, Zero LiPo, was added to allow the CPU to be powered by a rechargeable lithium polyion battery through a 2-pin JST surface mount connector. An Adafruit Industries lithium-ion polymer 500 mAh 3.7V battery was used to power the prototype. The Raspberry Pi Zero W emits an 802.11 b/g/n wireless local area network (LAN) allowing the prototype assembly to be controlled via Secure Shell (SSH) terminal communications over a wireless network. The operating system and user file space are stored on a Kingston Technology 16 GB speed class 4 Micro SD card that serves as the hard drive.

The prototype utilizes a microelectromechanical systems (MEMS) accelerometer to measure vibration (Figure 3.1). The Kionix KX126-1063 is a triaxial digital accelerometer with a user-configurable full-scale acceleration range of $\pm$2g, $\pm 4g$, or $\pm 8g$. It is equipped with several capabilities advantageous for the purpose of structural vibration measurement on timber distribution poles. One feature is tap detection that,

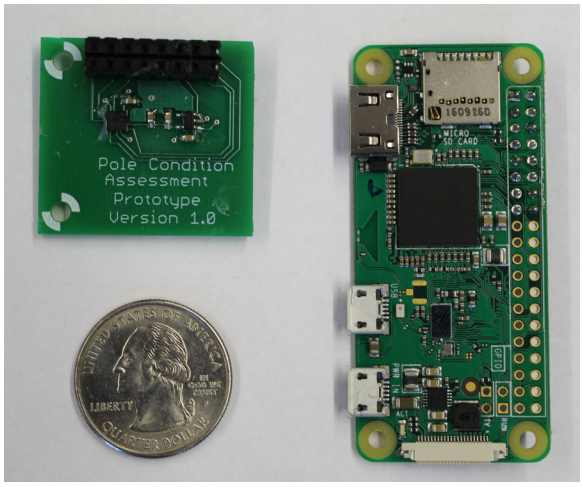

FIGURE 3.1: Photograph of developed sensor board next to a Raspberry Pi Zero W single-board computer

when enabled, can be used to trigger or pre-trigger data measurement upon a sudden change in acceleration. This permits the accelerometer to be programmed to continuously monitor accelerations while on, but only record the vibration time history during impulse excitations provided by the hammer strike. A 2048 byte data buffer can be programmed to store the measurement data, and the accelerometer is capable of continuing to record new data while older data is being read from the buffer on a first-in, first-out (FIFO) basis. The use of this buffer relaxes strict timing requirements for the embedded system, which is important for this particular prototype since the Raspberry Pi does not run a real-time operating system. The accelerometer communicates via a digital I^2C bus at a speed of up to 3.4 MHz, which permits acceleration data to be recorded at sampling rates up to 3200 Hz without data loss. It has high shock survivability and excellent temperature performance and operates from a 1.71 V - 3.6 V DC power supply. A custom circuit board was designed and fabricated to interface the accelerometer to the Raspberry Pi. A voltage regulator

was included in this circuit to condition the power supply provided to the accelerometer to maintain the noise performance and to allow the accelerometer to be remotely powered off when not in use.

The first generation prototype is fully enclosed in a custom designed polylactic acid (PLA) plastic case. The case was designed in Autodesk Inventor and 3-D printed using a Makerbot Replicator+. The case features a removable top to allow easy access to the 2-pin JST power connector for battery charging or wall power during software development and modification. The bottom outer surface of the case was designed to be curved with a radial dimension based on an average radius of a sample of 10 timber utility poles (Figure 3.2). This feature helps develop a secure and stable temporary mounting of the prototype to the utility pole. The top and bottom portions of the case are closed and secured together using a nut and machine screw on each corner. Machine screws are inserted through counter-bored holes in the bottom portion of the case in order to maintain a smooth contact surface between the prototype and the utility pole. A slot on the top side of the case allows the user to secure the prototype to the utility pole with an adjustable hook and loop strap (Figure 3.3). A key-operable on/off switch on the exterior of the case allows the user to open or close the circuit between the prototype and the lithium-ion polymer battery. The case allows the prototype to be operated safely in a laboratory or field setting but does not meet the standards of ruggedization that the final version of the pole condition assessment device must meet. A photograph of the assembled prototype, with the top of the case removed, is shown in Figure 3.4.

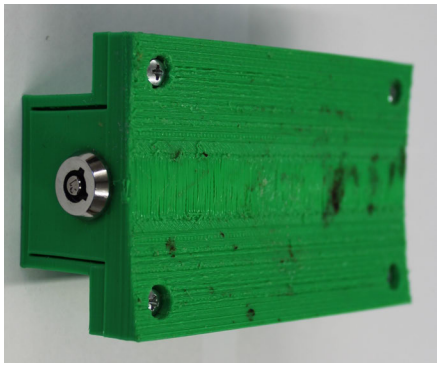

FIGURE 3.2: Photograph of the underside of the prototype showing the curved surface and counter-bored machine screw holes for smooth contact with pole as well as the key-operated power switch.

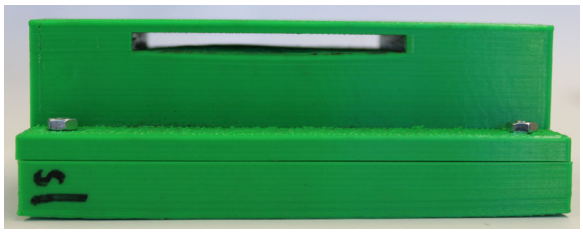

FIGURE 3.3: Strap slot to secure prototype to pole during testing.

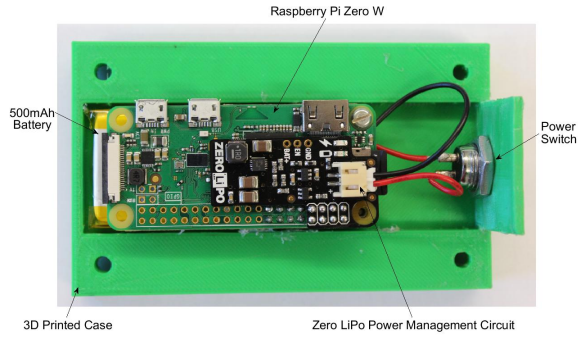

FIGURE 3.4: Photograph of components of the prototype assembled in the case

3.2 Development of Embedded Software

Additions and alterations were made to the default Raspian Jessie operating system installation in order to enable wireless control and access to data recorded by

the prototypes. Additionally, a user-friendly pole condition assessment routine was written in the C programming language in order to communicate with the MEMS accelerometer, record pole vibration data, and respond to remote requests from the operator. Other software modifications were added in order to prolong battery life and reduce the setup time required for a pole condition assessment. These aspects of the embedded software development are detailed in the following subsections.

3.2.1 Wireless Connectivity

The prototype was configured to run a standalone network as a wireless access point. This allows a user to connect to the prototype network using any device with WiFi capability, such as a laptop or smartphone. The single-board computer within the prototype can be controlled over the shared network through SSH. In this study, three nominally identical versions of the first generation prototype were fabricated and used. Each of the prototypes was equipped to serve as an access point for its own unique wireless network but were programmed to respect the existence of already established prototype networks. This measure was taken so that the end user could connect to multiple prototype sensors simultaneously, which would otherwise be prohibited by the SSH communication since WiFi connectivity at the laptop or smartphone can only be established with a single network. The prototype networks were programmed to follow a hierarchy such that Prototype 1 emitted the preferred network, followed in importance by Prototype 2, and then Prototype 3. For example, if all three versions of the prototype were powered on, the user will be able to connect to the network hosted by Prototype 1, which will also allow the user to communi-

cate with the other prototypes since they would automatically connect to this same network upon boot. Furthermore, if Prototype 1 runs out of battery power during the course of operation, Prototype 2 would then emit the preferred network upon reboot. The user would be able to connect to this unique network, which Prototype 3 would also automatically connect to upon boot. The prototypes were assigned static IP addresses to allow for quick SSH access of the prototype upon connection to the emitted network. The wireless capability of the prototype allows the user easily add or modify software remotely, and permits the user to run the pole condition assessment routine and review the recorded measurements while the prototype is fully enclosed and secured to a utility pole.

3.2.2 Embedded Software for Remote Data Collection

The pole condition assessment routine allows the user to initiate and monitor the progress of data sampling by the prototype during vibration testing. First, the user connects to the wireless network of the prototype using the same process that is used to connect any computer to a WiFi network. The user can then log in to the prototype and run the pole condition assessment routine via terminal commands using an SSH connection (Figure 3.5a).

Algorithm 1 provides a pseudocode for the data collection routine executed on the prototype. The program, written in C, first configures the MEMS accelerometer so that tap detection is enabled and measurement data is communicated to the single-board computer via the I^2C bus. The sampling rate of the accelerometer is also set to 3200 Hz. Following successful initialization, the program then displays a welcome

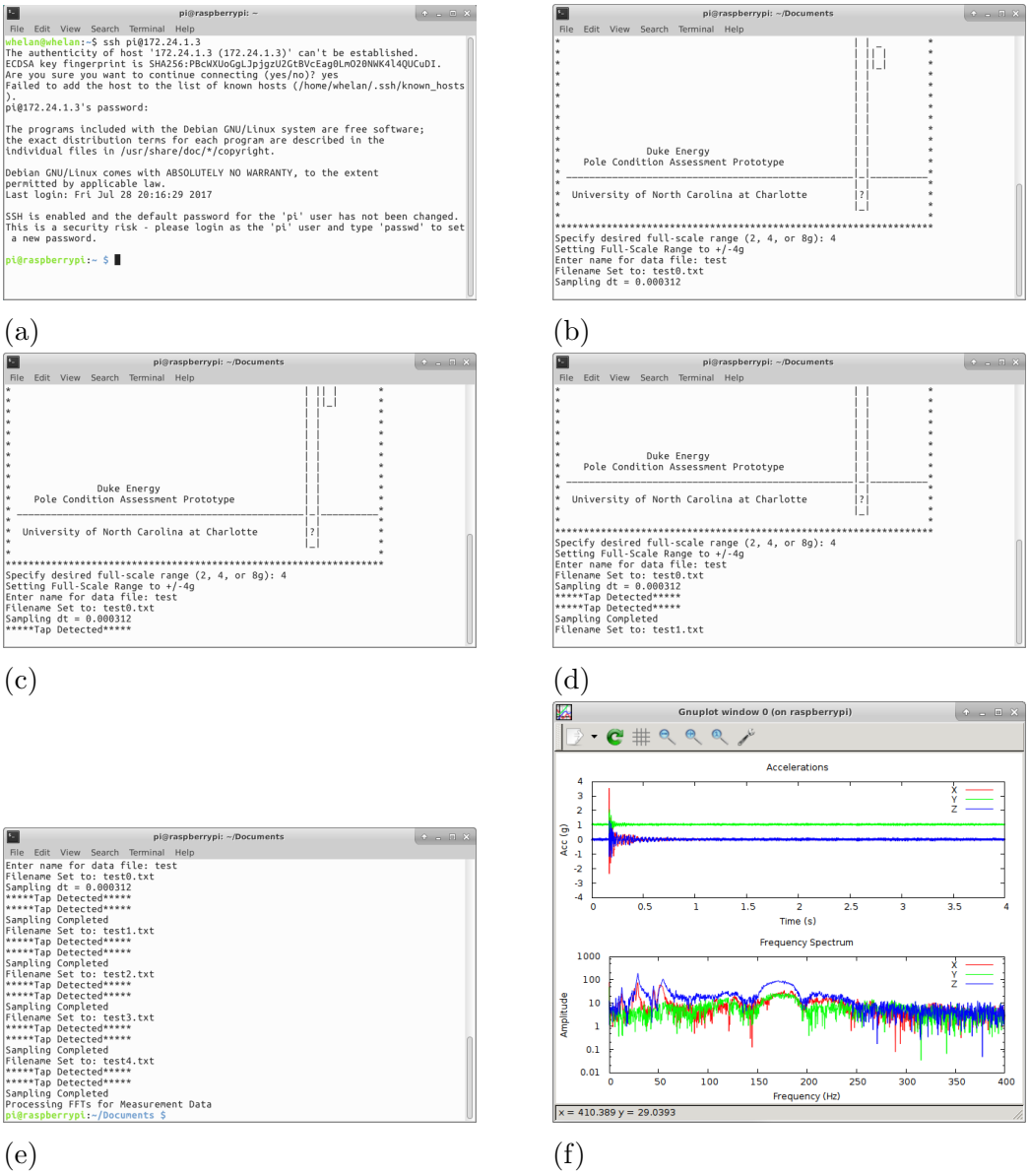

FIGURE 3.5: a) Log in to prototype through SSH; b) User enters acceleration range; c) Tap detected; d) Sampling of first strike completed; e) Sampling of all strikes completed; (f) Plots of time history and frequency response function

screen and prompts the user to specify the programmable maximum acceleration range and a filename prefix for the acceleration data files (Figure 3.5b). After this user input is set, the prototype begins sampling the three measurement axes to monitor for tap detection. Upon tap detection, a digital interrupt line signals the single-board computer to acquire the pre-triggered and post-triggered data from the FIFO buffer

on the accelerometer (Figure 3.5c). If the rate of measurement exceeds the rate of data transfer at any point, the overflow data is stored in the data buffer housed in the accelerometer. Data is transferred from the buffer to the computer on a FIFO basis while the accelerometer continues to measure data and store it in the buffer. The user receives a notification when the four second duration of sampling for the strike is completed (Figure 3.5d). Following the data retrieval, the measurements are converted from voltage to acceleration and written to a tab delimited text file. The data measurement and recording loop was programmed to run for five pole strikes to allow for averaging of spectral measurements consistent with prior laboratory testing. After sampling of the five strikes is completed, a fast Fourier transform is performed locally on the prototype using the acceleration data from each strike and the GNU Octave open-source programming language (Figure 3.5e). The acceleration data and the frequency response functions (FRF) for the strikes are also plotted in time and frequency domain, respectively, using gnuplot. These plots can be remotely accessed by the end user to review the characteristics of the field measurements following the testing (Figure 3.5f).

Algorithm 1 Prototype Data Collection Routine

Display welcome screen
User input: *Acceleration limit (±2g,±4g,±8g)*
User input: *Filename*
for Strike < 5 **do**
  Tap detected, accelerometer begins recording data
  Data communicated from accelerometer to computer via I^2C
  if Sampling Rate > Data Transfer Rate **then**
    Accelerometer buffer stores overflow data
    Data sampling continues. Data transfer continues on FIFO basis
  end if
  Sampling duration completed
  Data written to .txt file
end for
FFT performed on acceleration data
Plots generated for data in time and frequency domains

3.3 Performance Evaluation of Prototype Accelerometer

Time histories and frequency response functions (FRFs) developed from data measured by the prototype were compared to a high-end reference accelerometer interfaced with a commercial data acquisition system in order to validate the prototype measurements. A PCB Piezotronics 333B52 single-axis accelerometer was used to provide the reference acceleration measurement. This commercial accelerometer features a 1000 mV/g sensitivity and a 0.5 to 3000 Hz measurement bandwidth that is well suited for vibration testing of structural systems. The accelerometer was sampled with a National Instruments PXIe-4497 dynamic signal analyzer set to sample at 3200 Hz. The prototype accelerometer was also programmed to sample at 3200 Hz. This rate matches the expected operational sampling rate of the prototype when deployed for the proposed in-service condition assessment of timber distribution poles.

For this performance testing, the reference accelerometer was bonded to the case of the prototype to enable both devices to measure nominally identical vibration events concurrently. Since the measurement systems are inherently independent, the sampling was not time synchronized but post-processing of the data sets was performed to align and window the measurements from the prototype and reference systems to consistent measurements. Comparisons of the acceleration time histories obtained from testing performed on a timber pole in the laboratory (Figure 3.6) revealed that the amplitude waveform produced by the prototype correlated very well with the commercial system, except that small deviations on the time base were observed that increased with sampling time. Likewise, a comparison of FRFs revealed minor discrepancies in the spectral content measured by the two devices (Figure 3.7). Natural frequency estimates obtained from the prototype measurement data were observed to be consistently lower than those obtained from measurements obtained from the commercial accelerometer. This discrepancy, as well as the discrepancy visible in the time history data, suggests that the sampling clock on the prototype sensor is faster than the calibrated reference clock in the commercial data acquisition system.

The discrepancy in the measurement time base can be attributed to a wider tolerance in the sampling clock frequency for the low-cost MEMS sensor used in the prototype than in the high-end, calibrated commercial data acquisition system. While the programmed sampling rates for the prototype and the commercial accelerometer were set to the same value, the actual sampling rate for the prototype was higher than that of the commercial data acquisition system due to error in the sampling clock of

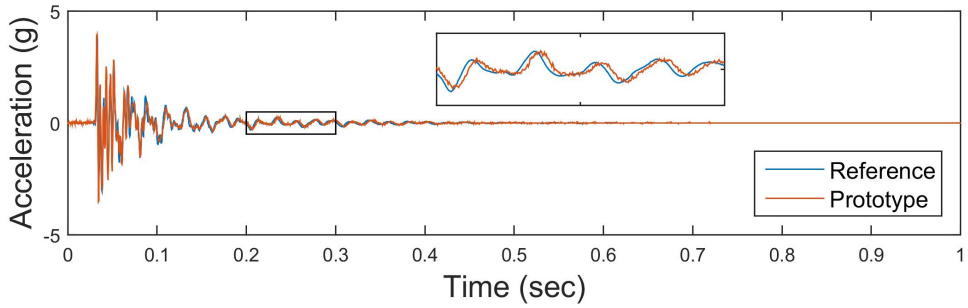

FIGURE 3.6: Comparison of impulse response time histories obtained from vibration testing of a timber distribution pole in the laboratory

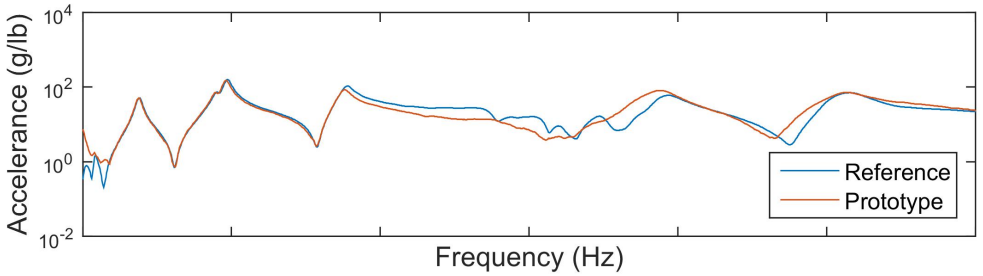

FIGURE 3.7: Comparison of frequency response functions obtained from vibration testing of a timber distribution pole in the laboratory

the MEMS accelerometer. Since frequency is proportional to the inverse of time, the ratio between the actual sampling rates of the two devices is equal to the ratio between the frequency estimates obtained from the two devices using the commercial measurement system as a reference. Consequently, by obtaining measurements comparing a range of known steady-state frequencies measured by the prototype to those measured by the accelerometer connected to the commercial data acquisition system, a linear regression could be performed to develop a correction factor suitable for calibrating the sampling clock of the prototype sensor to the reference system. This device-specific calibration is necessary in order to ensure the accuracy of the

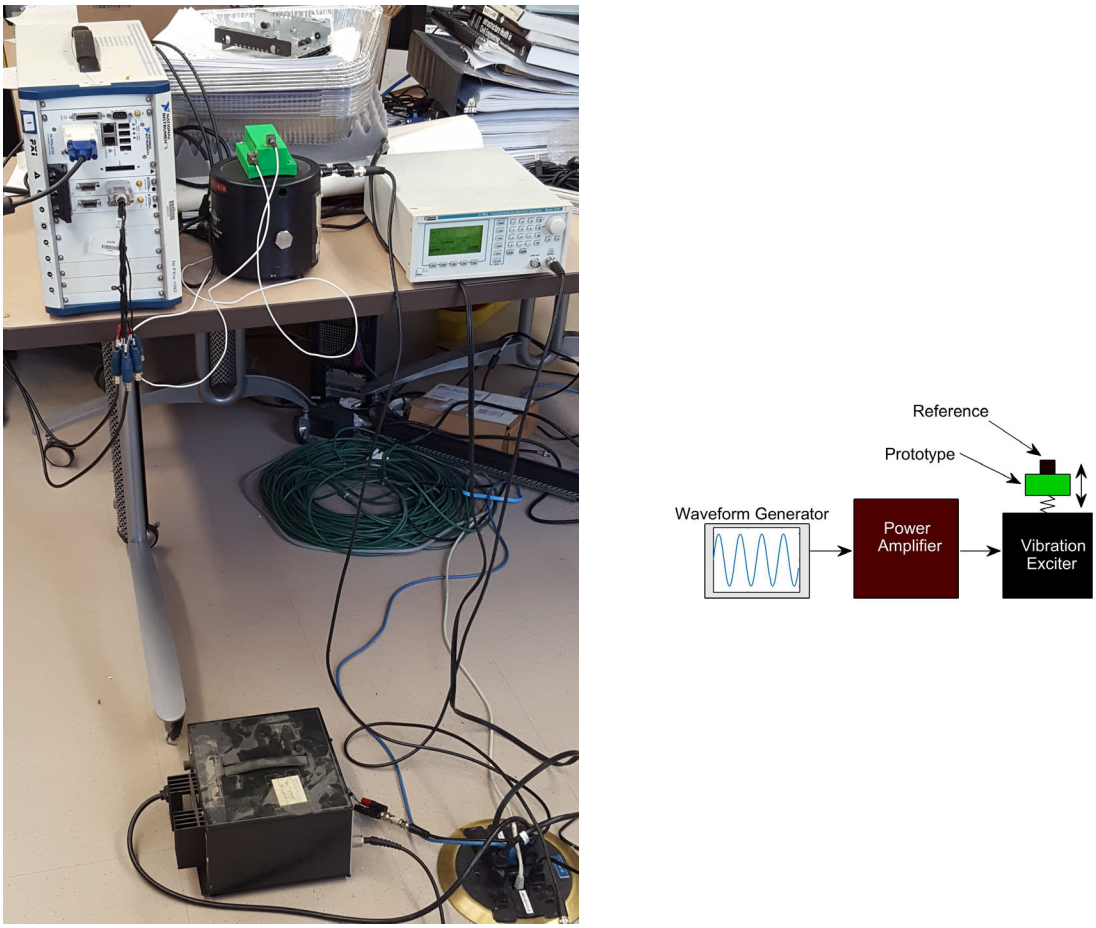

FIGURE 3.8: Laboratory setup for calibration of prototype sampling clock

natural frequency estimates.

A laboratory test setup was developed to determine correction factors for the prototype accelerometers using a vibration exciter (shaker) to subject the accelerometers to steady-state harmonic excitation (Figure 3.8). The prototype was bonded with hot glue to a Bruel and Kjaer vibration exciter Type 4809, that was driven by a Bruel and Kjaer power amplifier Type 2706. A TEGAM, Inc. Model 2720 31 MHz Function/Arbitrary Waveform Generator was used to produce sinusoidal waveforms with adjustable amplitude and frequency. The same commercial accelerometer was bonded to the case of the prototype to obtain the reference measurements and sampling of

the accelerometer was performed with the same data acquisition unit set to a fixed sampling rate of 3200 Hz.

The vibration exciter was used to subject the accelerometers to steady-state harmonic oscillation at a fixed frequency programmed through the waveform generator. Accelerations were then concurrently sampled from each accelerometer over a 60 second duration to provide a frequency resolution of less than 0.02 Hz in the frequency spectra. This sampling of steady-state harmonic oscillation was performed sequentially at excitation frequencies of 20, 50, 100, 150, 200, 250, 300, 350, and 400 Hz to calibrate the sampling clock over the bandwidth where the first eight structural modes of interest for the timber utility poles are present. The frequency spectra for each of these data sets were computed by the fast Fourier transform to identify the measured frequency of the vibration assuming a perfect sampling rate of 3200 Hz. Typical results are provided in Figure 3.9, which presents measurements obtained when the function generator was programmed to source a 200 Hz sine wave. The frequency measurement obtained with the commercial measurement system matched the prescribed frequency within 0.1 Hz, while the lower frequency measurement obtained by the prototype accelerometer indicates that the sampling clock frequency for this accelerometer is slightly higher than the programmed rate of 3200 Hz.

To obtain a correction factor for the frequency of the sampling clock of the accelerometer in each wireless prototype, the set of nine frequency estimates obtained from each system were plotted against each other. The frequency estimates were found to exhibit a strong linear relationship over the range of frequencies tested, which confirmed the assumption of differences in the sampling clocks being responsi-

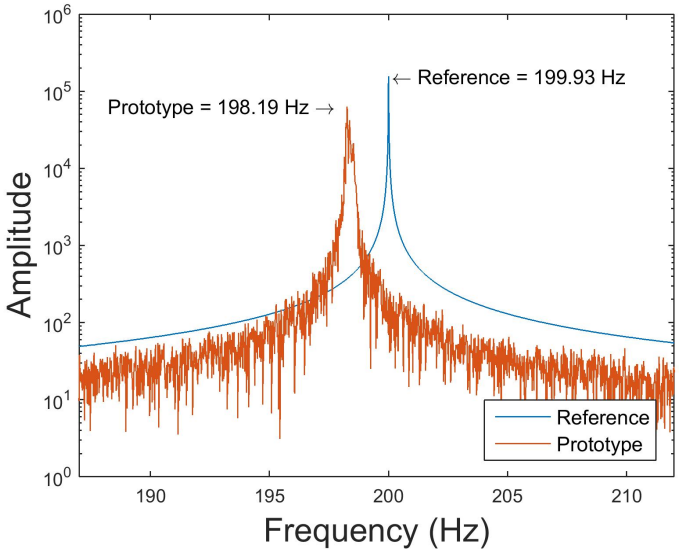

FIGURE 3.9: Windowed frequency spectra obtained from measurement of steady-state harmonic motion at 200 Hz

ble for the discrepancies in time and frequency measurements. The correction factors for each prototype were calculated using linear regression with the y-intercept constrained to zero (Figure 3.10). Constraining the linear regression to pass through the origin permits the correction of frequency estimates through a single scalar multiplier applied to the sampling clock of the prototype sensor. Correction factors for each of the three accelerometers were greater than one, which indicates that all clocks were faster than the reference clock, and the worst error in the sampling rate of the clocks was approximately 2%. The R^2 values for the linear regressions for Prototypes 1, 2, and 3 were 0.99909, 0.99975, and 0.99857, respectively, which indicates that a linear correction factor is suitable over the range of frequencies tested. Comparison of measured time histories (Figure 3.11) and frequency response functions (Figure 3.12) after the compensation for the differences in clock frequency was applied reveal strong correlations between measurements obtained with the developed prototype and the

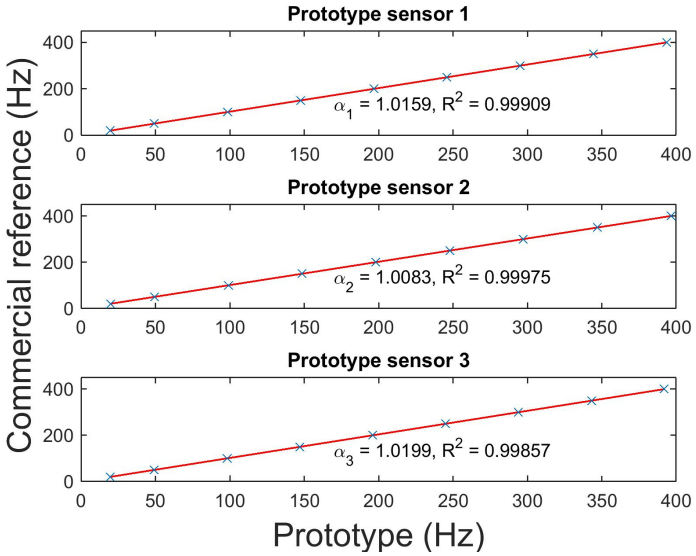

FIGURE 3.10: Linear regression of correction factors for the three prototype accelerometers developed in this study.

commercial reference system and the absence of deviations in the time base of the measurements. Despite the success of this calibration, it should be noted that the sampling clock frequency may be temperature dependent, although no attempt was made to characterize the influence of temperature on the time base of the wireless prototype sensor.

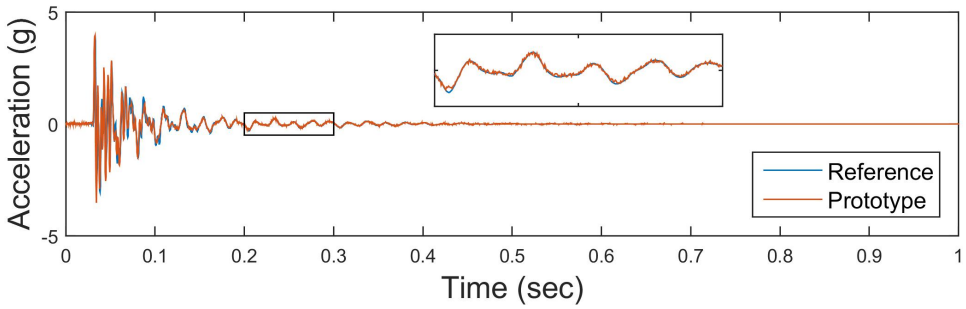

FIGURE 3.11: Comparison of impulse response time histories after application of the sampling clock correction factor

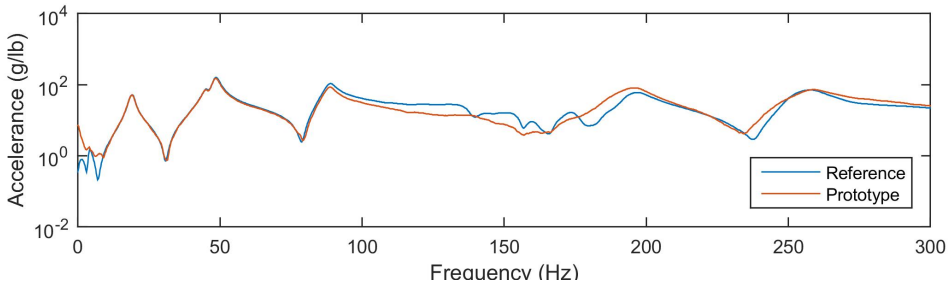

FIGURE 3.12: Comparison of frequency response functions after application of the sampling clock correction factor

In the course of developing the sampling clock correction factors, a discrepancy was observed between the vibration amplitudes measured by the prototype and those measured by the reference system (Figure 3.13). The ratio of the amplitude measured by the prototypes and the commercial reference at each steady-state excitation frequency were computed and plotted against the excitation frequency (Figure 3.13). This amplitude loss was found to be more pronounced at higher frequencies, and the amplitude measured at 400 Hz by the prototype is as low as 21.6% of that measured by the reference system (Figure 3.14). The characteristics of the amplitude ratio with frequency are similar to that of a low-pass filter, which suggests that this discrepancy may arise from the electrical circuit in the MEMS accelerometer. It is also possible that the amplitude differences may be a result of the different locations of the accelerometers, as the MEMS accelerometer is bonded to the base of the case and the reference accelerometer is bonded to the top of the case. The dynamics of the top of the case may lead to significant differences in the vibration amplitude transferred to the reference accelerometer if the cavity of the case is approaching the resonance frequency. This is a likely possibility, especially since the amplitudes measured during impulse response testing (Figure 3.11) exhibited strong correlation without evidence

of this amplitude discrepancy. Since the ultimate goal of the measurement system is only to estimate natural frequencies, differences in the acceleration amplitudes are not a concern and the amplitude loss does not appear to affect the accuracy of the frequency estimates. However, if the discrepancy is a result of electrical filtering in the accelerometer or other performance limits of the sensor, then a higher quality accelerometer may be needed for the prototype to reliably detect the higher natural frequencies of in-service utility poles.

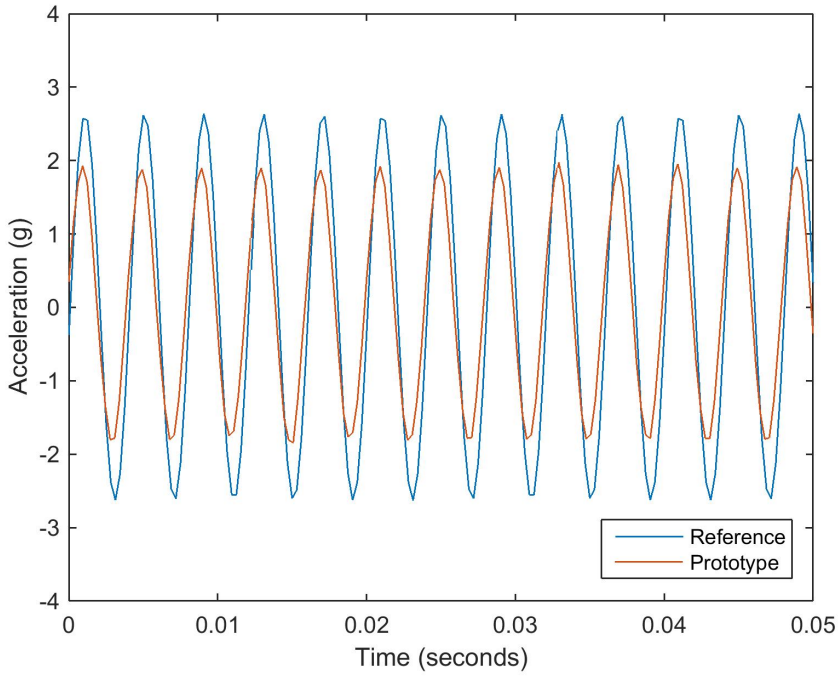

FIGURE 3.13: Comparison of steady-state harmonic oscillation amplitudes measured by the prototype and reference measurement systems

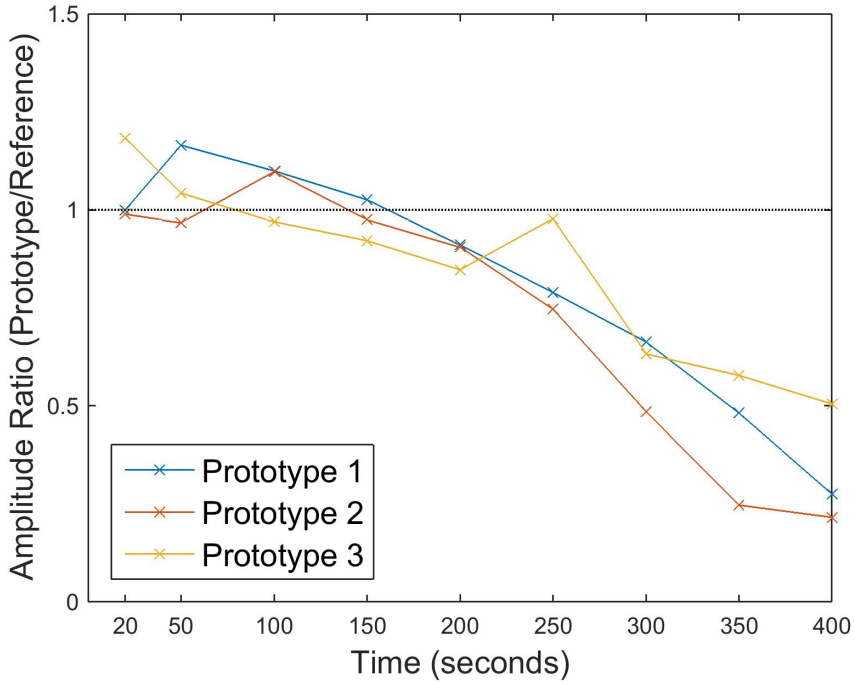

FIGURE 3.14: Discrepancy in acceleration amplitude measured by prototype system and commercial reference system during laboratory performance characterization

3.4 Laboratory Validation of Prototype Measurements

To assess the performance of the developed wireless prototype sensor for estimating natural frequencies of timber utility poles, vibration responses of actual timber poles were measured simultaneously by the first generation pole condition assessment prototype and a high end commercial reference accelerometer. Following the testing approach outlined in Barber (2016), impulse excitations were used for excitation and accelerations were measured for a set of ten poles embedded in a laboratory test pit (further information on the laboratory test pit and poles is provided in a subsequent chapter). Natural frequencies were estimated through system identification of the acceleration measurements using the Eigenvalue Realization Algorithm. Estimates

from the prototype were compared to those from the high end reference system to evaluate the performance of the prototype.

Reference accelerometers were attached to the prototype case with hot glue to allow for acquisition of simultaneous measurements from both the prototype sensor and the commercial measurement system (Figure 3.15). The reference accelerometers were attached to measure vibrations along orthogonal axes, which may differ if the pole cross section is asymmetric or there is decay in the pole. The orientation of the prototype and reference sensors in relation to these axes and the pole cross section are depicted in Figure 3.16. Validation measurements were obtained using two separate configurations. In the first configuration, the prototype was secured to the surface of the pole along axis 1. In the second configuration, the prototype was secured along axis 2. In both configurations, the elevation of the prototype was six feet above grade following the recommendation developed in Barber (2016). The pole testing procedure was the same for both sensor orientations and consisted of a total of 15 impulse excitations, or strikes, performed on each of the ten poles. Acceleration data was measured for four seconds following each strike. Strikes 1-5 oriented the hammer to excite vibration modes primarily along axis 1, strikes 6-10 excited vibration modes along axis 2, and strikes 11-15 excited vibration modes along axis 3, which is 45 degrees between axes 1 and 2.

FIGURE 3.15: Photograph of prototype installation on timber pole with cable-based accelerometers installed on the case of prototype for reference measurement

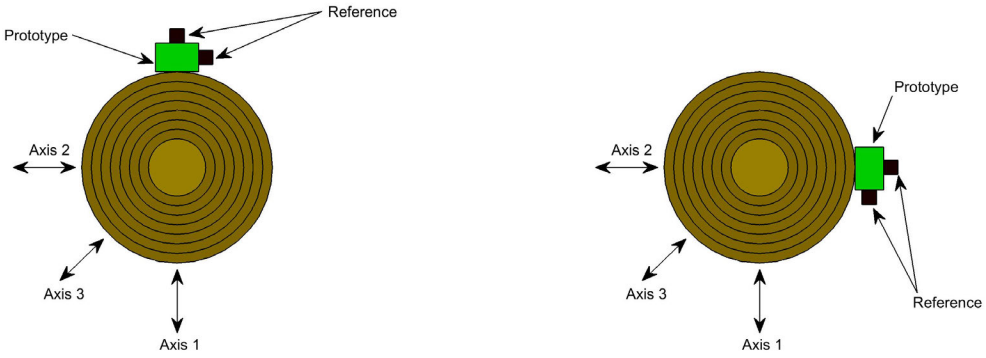

(a) (b)

FIGURE 3.16: Prototype orientation relative to pole cross section a) Orientation 1; b) Orientation 2

Results of the lab validation of the prototype are shown in Figure 3.17, which plots the natural frequencies of each of the ten poles obtained from measurement data acquired from the prototype against the natural frequencies obtained from the reference measurement data. As expected, an approximately linear and proportional relationship exists between the natural frequencies predicted by the prototype and those

obtained using the commercial accelerometer. In general, larger absolute differences between the natural frequencies were observed for higher natural frequencies with the errors being generally balanced about the 1:1 reference line. Using the estimates obtained from the commercial accelerometer as a reference, the percentage errors in the natural frequency estimates obtained from use of the prototype were calculated using Equation (1).

$$PercentageError = \frac{f_{n,prototype} - f_{n,reference}}{f_{n,reference}} \tag{1}$$

These percentage errors were plotted against the corresponding natural frequencies from the reference measurement to see if the error was biased by the natural frequency (Figure 3.18). Error in the fundamental frequency predictions was found to be as high as 28% due to the sensitivity of this low frequency to small differences in measurement prediction and the difficulty associated with accurately estimating this natural frequency due to the low amplitude of acceleration developed in this mode during impulse testing. These errors are not a particular concern as the fundamental natural frequency was excluded from the development of the original condition assessment algorithm due to the challenges associated with obtaining an accurate natural frequency estimate for this mode. The prediction errors for all other modes within the measured bandwidth were within 5% with few exceptions. The mean and the standard deviation of the percentage errors for all estimates, with the exception of those for the fundamental mode are 0.8% and 1.5%, respectively. The prototype is

deemed to able to reliably estimate frequencies within 3.7% of the value predicted by the reference accelerometer with 95% confidence.

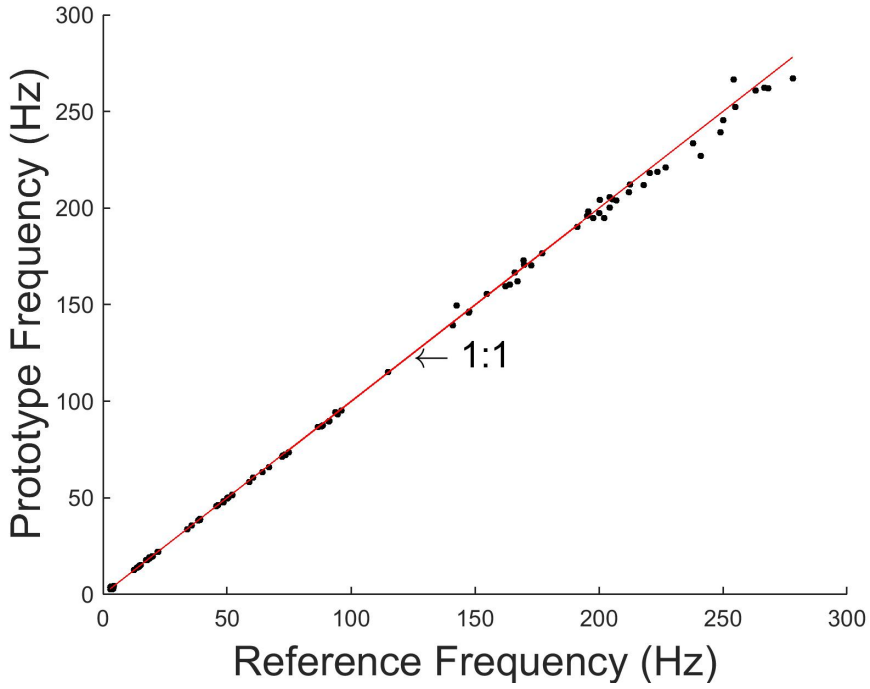

FIGURE 3.17: Comparison of frequency predictions obtained from prototype and reference systems based on concurrent measurements

In Barber (2016), the average error between the natural frequencies predicted by the Rayleigh-Ritz model for a healthy pole following model updating and those measured experimentally using the wired commercial system was approximately 2%. Since the objective function that drives the optimization scheme in this method relies on the absolute error between measured natural frequencies and those predicted by the model, the 95% confidence interval on the error between the prototype and reference measurements is too large to justify extended analysis of the use of the current prototype for pole condition assessment at this time. The discrepancies in oscillation amplitudes identified during the calibration of the sampling clock of the prototype sensor cast

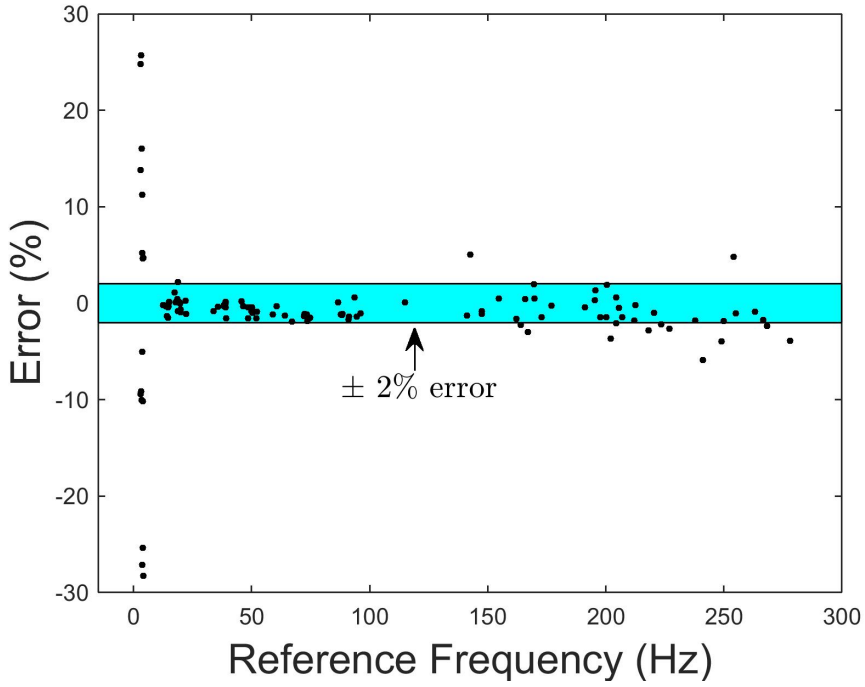

FIGURE 3.18: Percentage error between natural frequencies estimated by prototype and natural frequencies estimated by reference system

additional doubt on the suitability of the prototype to perform the laboratory and field validation detailed in the subsequent chapters of this work. Consequently, the laboratory and field validation of the method developed in Barber (2016) discussed in subsequent chapters will be performed using experimental measurements acquired with the cable-based commercial test and measurement system.

CHAPTER 4: LABORATORY VALIDATION OF VIBRATION-BASED CONDITION ASSESSMENT AND EXTENSION OF LABORATORY TESTING TO ASPHALT ENCASEMENT

This chapter reports the procedure and results of the laboratory validation of the vibration-based condition assessment introduced in Barber (2016). Ten utility poles that were previously in service are embedded in a poorly-graded sand within a concrete-lined geotechnical test pit in the EPIC Structural High Bay Laboratory at University of North Carolina at Charlotte. The natural frequencies of each pole are estimated from structural vibration measurements and were used along with geometric dimensions of the poles to calibrate a physics-based model for each pole based on the Rayleigh-Ritz Method. The estimated extent of the decay in the region of the pole 6 to 18 inches below the ground line predicted by the calibrated model is compared to destructively obtained profiles of the actual section loss. In addition to this validation, this chapter also explores the application of the condition assessment technique to the common field condition of encasement introduced by paving materials, such as asphalt or concrete. Extended testing of the same ten poles is performed after placing a layer of hot mix asphalt in the test pit and the effect of the encasement on the natural frequencies and performance of the nondestructive condition assessment algorithm is assessed.

4.1 Validation of Condition Assessment Technique Using Second Set of Ten Poles Embedded in Laboratory Test Pit

4.1.1 Description of Laboratory Test Pit and Pole Specimens

Following on the initial research performed by Barber (2016), a set of ten additional timber utility poles were embedded in the same poorly-graded sand in the cylindrical, concrete-lined geotechnical test pit used in the original research. Holes for pole installation were augured using a four foot long, 16 inch diameter auger bit and bit extension (Figure 4.1a). Laboratory embedment depths were set to match the field embedment depths of the pole by using the presence of residual soil, coloring of the pole, and presence of any plugs from prior inspection to identify the location of the ground line. An overhead crane was used to lift the poles and install them in the augered holes (Figure 4.1b). A photograph of the complete experimental test setup with all 10 poles installed in the test pit is provided in Figure 4.1c. The height, base circumference, top circumference, and embedment depth were measured before the poles were installed (Table 2). The poles were numbered from 11 to 20 since they supplement the original set of 10 poles tested in Barber (2016). The extent of decay in the region below the groundline varied across the set of 10 poles tested. The external appearance of the embedded portion of the poles is shown in Figure 4.2, and qualitative descriptions of the health of the embedded portions of the poles in the second set are given in Table 3. In general, the severity of the decay in the poles with the most significant section loss did not appear to be as severe as the three poles with the most severe section loss in the original study, although several of the poles did have advanced section loss.

(a)

(b)

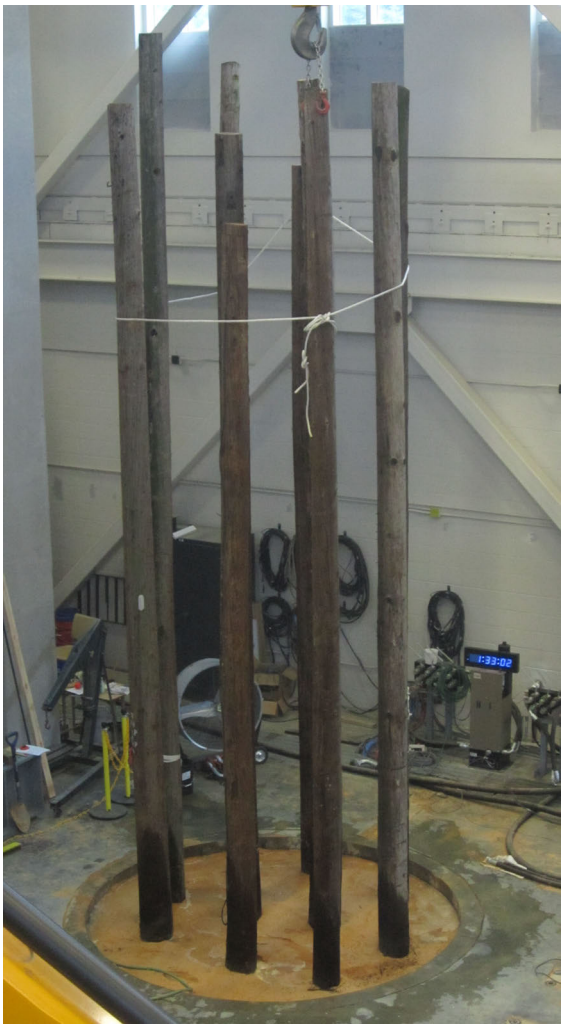

(c)

FIGURE 4.1: Preparation of experimental test pit for pole installation: a) augering of hole to embedment depth, b) placing pole to mimic field condition, c) set of ten poles installed in test pit

TABLE 2: Geometric characteristics of timber utility poles used for laboratory testing

Pole Number	Pole Length	Pole Base Circumference	Pole Top Circumference	Pole Embedment Depth
11	28’ 1”	34.75”	26.5”	6’ 3”
12	29’ 10”	35.25”	22.75”	6’ 3”
13	30’ 0”	25.5”	20.75”	5’ 10.25”
14	30’ 0”	35.5”	24.0”	5’ 0.5”
15	27’ 6”	39.0”	27.5”	5’ 1”
16	29’ 7”	36.0”	29.0”	5’ 10”
17	30’ 0”	34.0”	25.0”	6’ 2.5”
18	29’ 6.5”	40.0”	25.5”	6’ 3.5”
19	26’ 6”	36.75”	25.25”	6’ 3”
20	29’ 10”	31.25”	22.25”	6’ 3”

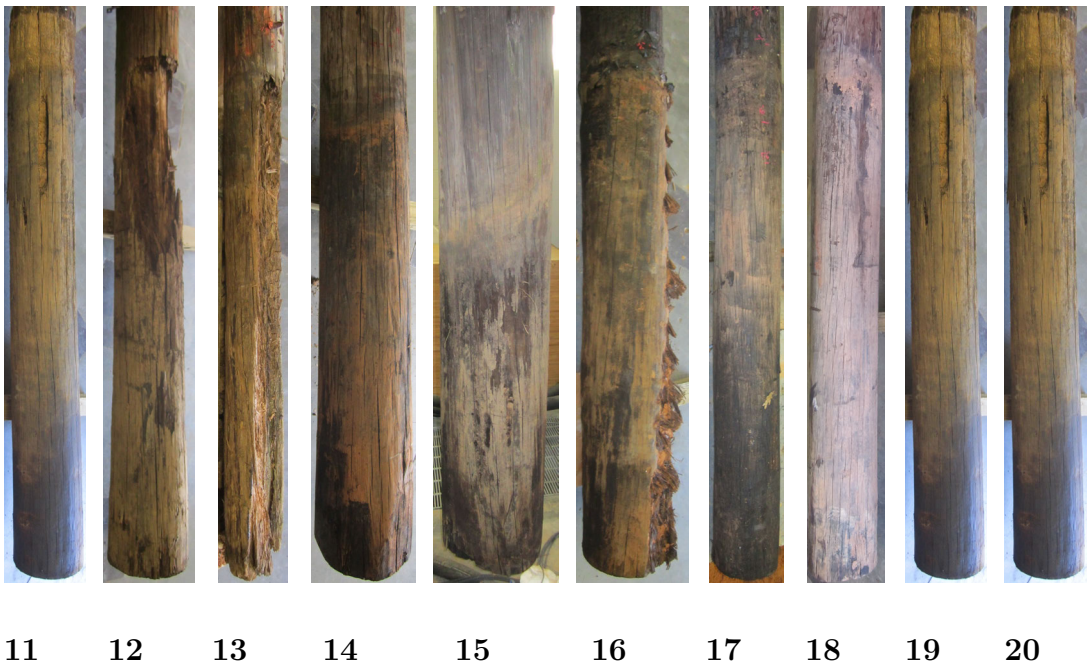

FIGURE 4.2: Pole profiles in region below the ground line

4.1.2 Destructive Testing and Damage Classification

After vibration testing was completed, a characterization of the actual decay present in the poles was needed to evaluate the performance of the method. Destructive test-

TABLE 3: Description and condition summary of poles in validation set

Pole	Description of pole and condition
11	Shell rot in region just below ground line
12	Severe shake around heartwood caused slices to fall apart during destructive testing
13	Decay primarily in a region 20 to 30 inches below ground
14	Healthy
15	Moderate checking but otherwise healthy
16	Healthy
17	Healthy with some checking
18	Ring shake around heart over nearly three feet of depth
19	Moderate section loss over a large region that extends above ground
20	Moderate decay just below the groundline

ing of the poles was used to assess the location and extent of actual decay in the poles below ground. The embedded portion of each pole was cut across the cross section with a band saw into slices approximately three inches in thickness. Slices were cut from the bottom tip of the pole up to six inches above ground or to the top of the decayed region, whichever was highest. Each slice was photographed on a white background with an 18 megapixel Canon EOS Rebel T6 digital single-lens reflex (DSLR) camera positioned on a stationary tripod to look down upon the cross section. A black square was used to provide a high contrast dimensional reference for calculations of the section properties of the pole slice. Photographs of the slices of each pole are shown in Appendix C and are labeled according to their position relative to the ground line. The photographs were analyzed using a digital image processing routine in MATLAB (Figure 4.3). The high contrast in color between the timber and the white background was exploited to trace a boundary around the cross section of the slice, which was subsequently masked to calculate a total pixel area of the pole cross section. A boundary was also traced around the high contrast square

of known area. The ratio between the pixel area of the slice and the pixel area of the reference square was multiplied by the known physical area of the square in order to find the cross sectional area of the slice. The second moment of area about axis 1 and axis 2 (I_y and I_x, respectively) were also calculated from the analysis of the pixels contained within the traced boundary. These section properties were plotted with their position relative to the ground line in order to illustrate and quantify the changes in the cross section with depth. These plots are provided in Appendix D along with profile images of the below ground region of the poles.

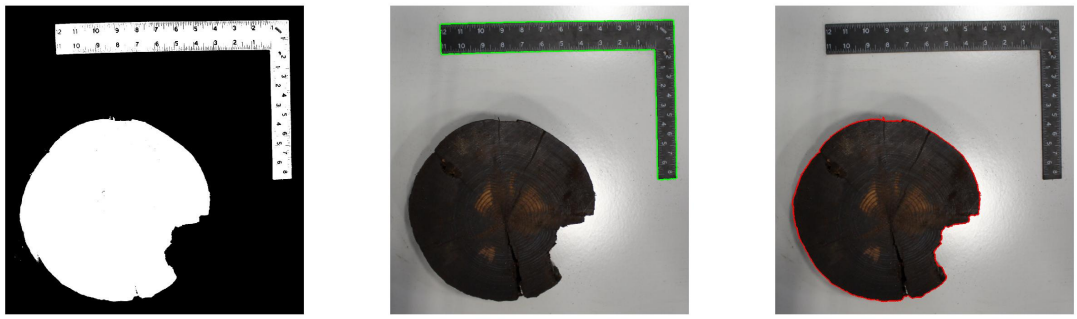

FIGURE 4.3: Digital image processing routine in MATLAB used to trace profile perimeters of pole slice and reference scale

The method developed in Barber (2016) was stated to show potential not only for identifying poles with critical levels of decay, but also in quantifying the relative severity of decay in a set of poles. However, this assessment was performed qualitatively without directly comparing the identified decay parameter with the measured loss of cross sectional area obtained through destructive testing. To perform quantitative analysis of the accuracy of the decay parameter relative to the measured section loss, a quantitative measure of actual decay below the ground line is needed. The process used to quantify the actual decay severity based on the destructive charac-

terization results is illustrated in Figure 4.4. An expected cross sectional area was first calculated using a linear gradient between two elevations on the pole deemed to be healthy because of their relative positions on a plot of cross sectional area with depth. It should be noted that for a linear tapered pole, it is the radius, r, that changes linearly with depth, and the change in expected cross sectional area is a quadratic function of r^2. However, since the taper of a utility pole is mild and the expected radius of the pole does not change significantly throughout the embedded portion of the poles, the change in expected area over the embedded portion of the pole can be approximated as linear. The relative extent of decay in the cross section was calculated using the difference between the projected expected area and the actual cross sectional area identified through destructive testing. The maximum relative reduction in cross section was calculated along with the average relative reduction in cross section over the critical region of the pole from 6 to 18 inches below the ground line.

The estimated profile of expected healthy area and estimated extent of decay for each of the ten poles tested in the first phase of this project by Barber (2016) are shown in Figure 4.5. Note that for some of the poles deemed to be healthy, cross section slices were only obtained for a limited portion of the depth to simply confirm the absence of decay. The estimated profile of expected healthy cross sectional area and estimated extent of decay for each of the ten additional poles tested in this current study are shown in Figure 4.6. The decay analysis region for each pole is located 6 to 18 inches below the groundline and is outlined in blue on the cross sectional area plots. The loss in cross sectional area for the complete set of laboratory poles is given

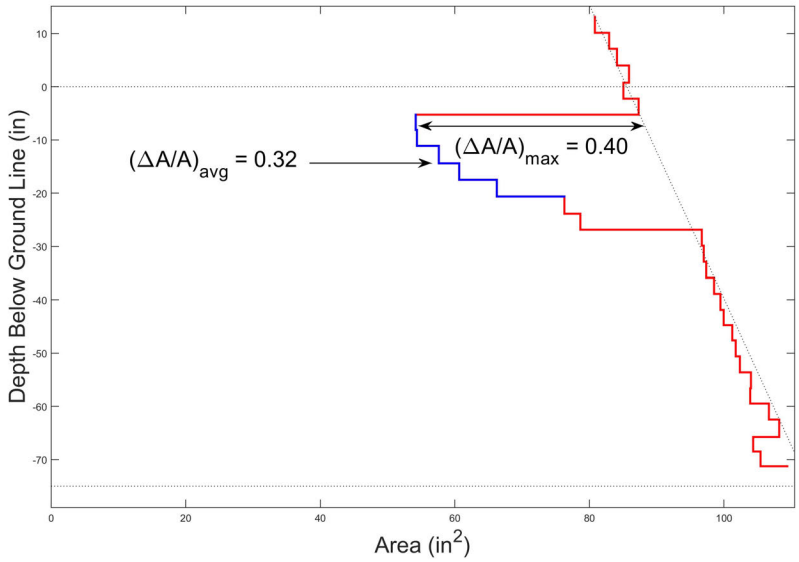

FIGURE 4.4: Calculation of maximum and average loss in the cross section from 6 to 18 inches below ground

in Figure 4.7. For the destructive characterization used to evaluate the performance of the condition assessment method, the poles were ranked according to maximum cross section loss, $(\frac{\Delta A}{A})_{max}$, since this value represents the critical section of the pole where a failure may occur (Figure 4.7a). The poles are color-coded blue, green, or red to signify a healthy, moderately decayed, or severely decayed pole, respectively. Based on the destructive characterization, two poles from this set, Poles 11 and 12, were classified as having severe section loss, while an additional four poles (Poles 13, 18, 19, and 20) were classified as having moderate section loss and decay. It should be noted that, while Pole 18 did not have significant loss of cross sectional area, this pole had significant ring shake extending to the heart of the pole that will reduce its strength and stiffness (Wood et al., 1960). Consequently, this pole was classified as moderately decayed. Additional discussion on the decay in pole 18 will be provided later in this chapter. The remaining four poles (Poles 14, 15, 16, and 17) were deemed

to be healthy and suitable for continued service.

Destructive characterization according to average cross section loss, $(\frac{\Delta A}{A})_{avg}$, is shown in Figure 4.7b. While the overall characterization of the poles is similar to that based on the maximum cross section loss, there are some differences in the rankings of the poles that shows possible error present in the destructive characterization method. While the destructive characterization method is suitable for giving an approximate quantification of actual decay in the poles, the exact rankings of the poles according to severity of decay should be viewed with some skepticism.

4.1.3 Laboratory Validation Procedure

Validation testing performed on each of the poles utilized two PCB Piezotronics 333B52 single-axis accelerometers to measure transverse vibrations due to impulse excitation with a PCB Model 086D20 Impulse Hammer with a soft (brown) tip. The accelerometers and force sensor from the impulse hammer were sampled with a National Instruments PXIe-4497 dynamic signal analyzer sampling at 1000 Hz. The sensor orientation used for this validation testing is shown in Figure 4.8a alongside a photograph of the temporarily installed sensors Figure 4.8b). The two sensors were placed on the pole along orthogonal axes at an elevation of six feet above ground, following the recommendations developed in Barber (2016). The orientation of the sensors allows for the measurement of vibrations along orthogonal axes, which may differ if the pole cross section is asymmetric or there is decay in the pole. The pole testing procedure consisted of a total of 15 impulse excitations, or strikes, performed on each of the ten poles. Acceleration data was measured for four seconds following

FIGURE 4.5: Estimated extent of cross sectional area loss obtained through destructive characterization of the original set of ten poles

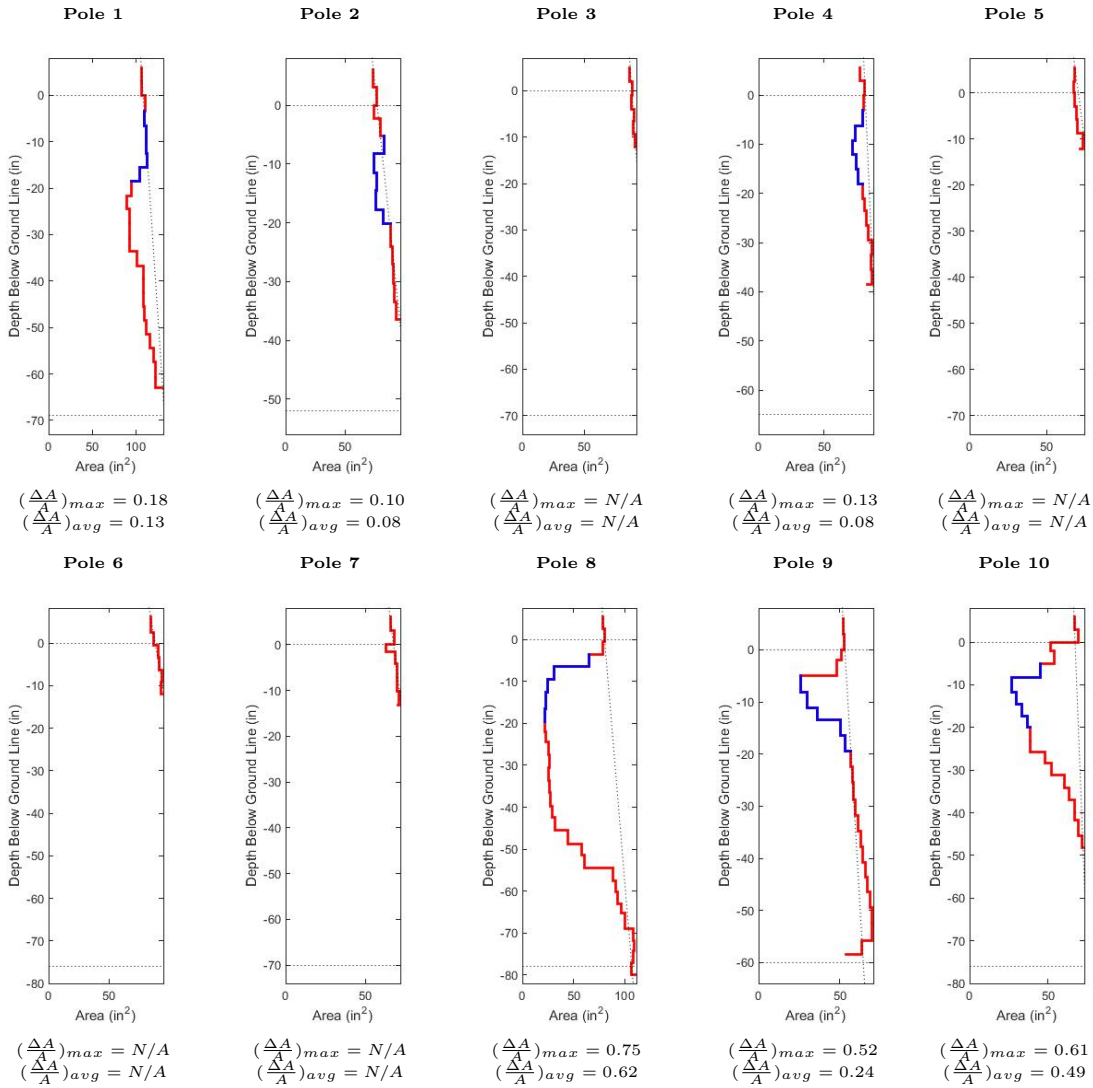

FIGURE 4.6: Estimated extent of cross sectional area loss obtained through destructive characterization of the second set of ten poles

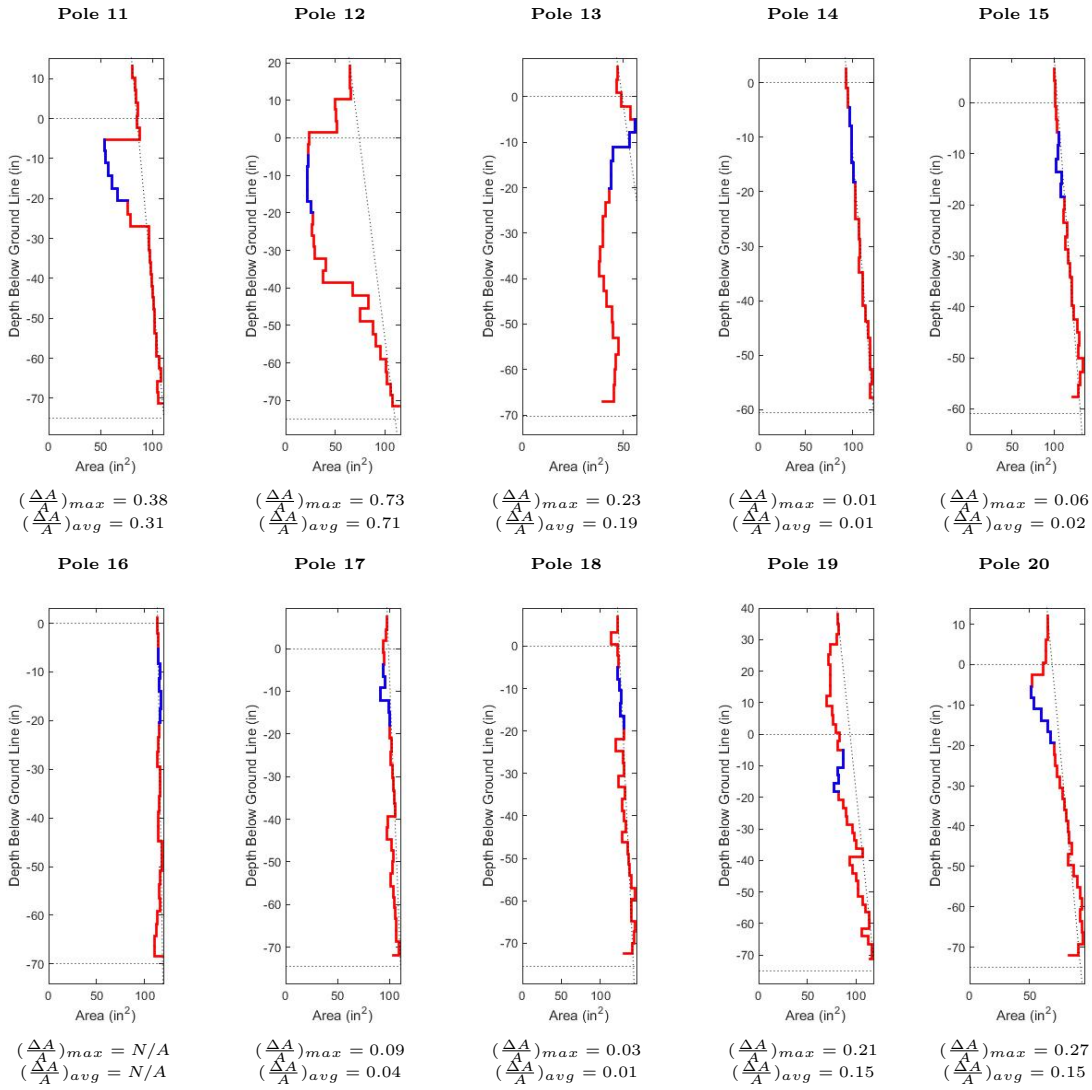

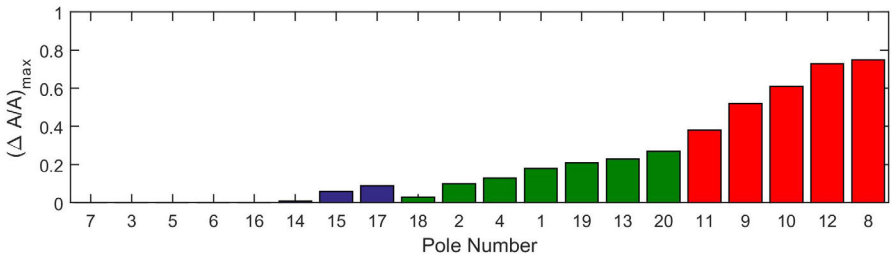

(a)

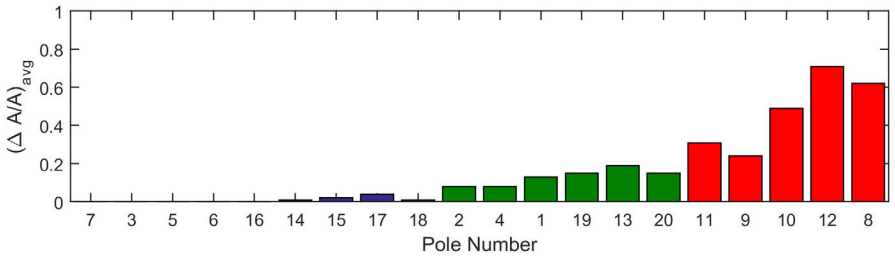

(b)

FIGURE 4.7: Loss in cross section of poles calculated as: a) $(\frac{\Delta A}{A})_{max}$ b) $(\frac{\Delta A}{A})_{avg}$

each strike. Strikes 1-5 oriented the hammer to excite vibration modes along axis 1, strikes 6-10 excited vibration modes along axis 2, and strikes 11-15 excited vibration modes along axis 3, which is 45 degrees between axes 1 and 2. The acquisition of data from multiple strikes along each axis allows for the prediction of natural frequencies using an average of frequency response functions from several nominally identical strikes.

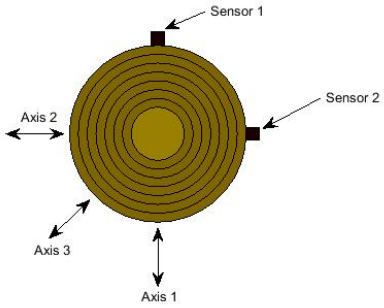

(a)

(b)

FIGURE 4.8: Sensor and axis orientation relative to pole cross section

4.1.4 Experimental Estimation of Natural Frequencies

The natural frequencies of the poles were estimated from the measured vibration data through the same system identification routine used in Barber (2016). A fast Fourier transform (FFT) was used to convert the acceleration and force time histories into frequency spectra. These input and response frequency spectra were then used to compute the frequency response function (FRF) using the H_1 estimator (Brandt, 2011). The FRFs for the poles from Set 2 are grouped in Figures 4.9 and 4.10 according to the decay severity of the pole as determined by the destructive testing consistent with observations made in Barber (2016). Healthy poles were found to produce a 'clean' FRF with sharp resonance and anti-resonance peaks with smooth transitions between resonance and anti-resonance. In contrast, severely decayed poles produce less distinct resonance and anti-resonance peaks and less smooth curves in the FRF. Additionally, severely decayed poles tend to have lower resonance frequencies, which is indicative of lower flexural stiffness. However, pole geometry, timber stiffness,

and mass also affect the natural frequencies so simply evaluating the magnitudes of the natural frequencies is insufficient for pole condition assessment.

The natural frequencies of the pole are related to the resonance peaks in the FRF and aid in the selection of natural frequencies during system identification, but simply selecting the peak frequencies in the FRF is insufficient for determination of natural frequencies. An inverse FFT was performed on each FRF to produce impulse response time histories that were then analyzed using the Eigenvalue Realization Algorithm (ERA) to produce the system identification (Juang and Pappa, 1985). This application of the ERA was performed using the semi-automated routine described in Barber (2016). To aid in the selection of natural frequency estimates, the measured geometric properties of each pole were used to develop a baseline Rayleigh-Ritz prediction model to produce estimates of the relative expected magnitudes of the first eight natural frequencies.

One important deviation in the system identification routine from that used in Barber (2016) is that measurement data from each individual axis was analyzed independently instead of averaging the measurements across the two axes to create a single set of natural frequency estimates. This change in the routine was made to be more consistent with the physical response of the pole dynamics, which may differ over the two axes especially if there is asymmetric decay in the pole. By analyzing the natural frequencies for each axis independently, the parameter identification results are expected to be more accurate and may possibly identify the spatial location of the decay in the cross section in addition to the severity. While this latter capability is not necessary to address the motivation for this study, the ability to determine

where the decay is within the cross section could assist in informing pole reinforcement strategies. Since the system identification routine used in Barber (2016) was modified, the data from this past study was reanalyzed using the new approach and the natural frequency estimates for each axis for the first set of ten poles is provided in Appendix E. Parameter identification for condition assessment of these 10 poles will also be performed again in this chapter.

Estimates of the natural frequencies and the corresponding damping ratios selected from validation testing of the ten poles from Set 2 along axis 1 and axis 2 are provided in Table 4 and Table 5, respectively. As with the testing performed in Barber (2016), the identification of the fundamental natural frequency was deemed unreliable due to the generally large damping ratio estimates.

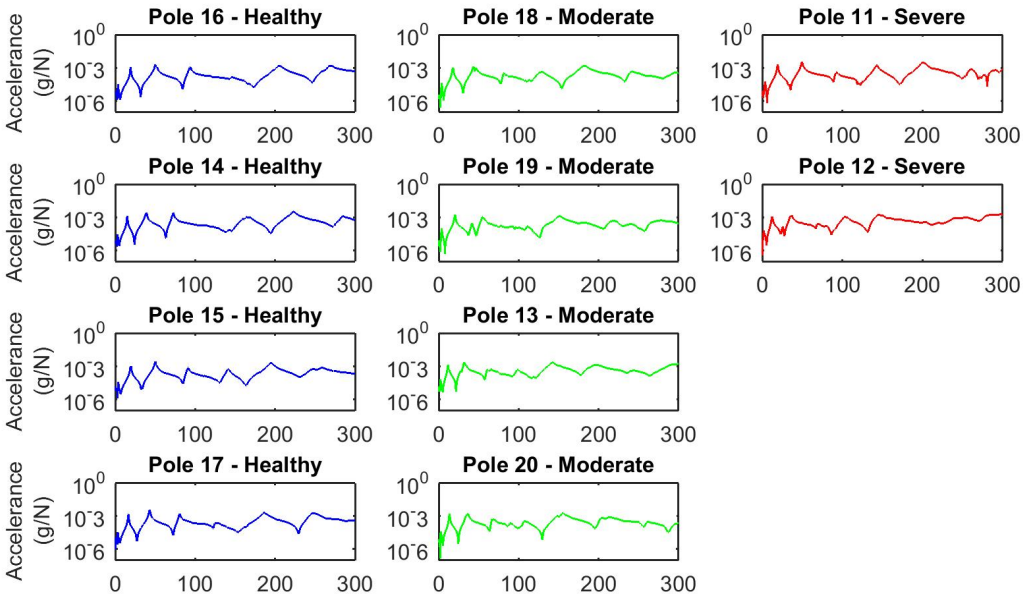

FIGURE 4.9: FRFs for vibrations about axis 1 from all poles in Set 2 grouped by decay severity

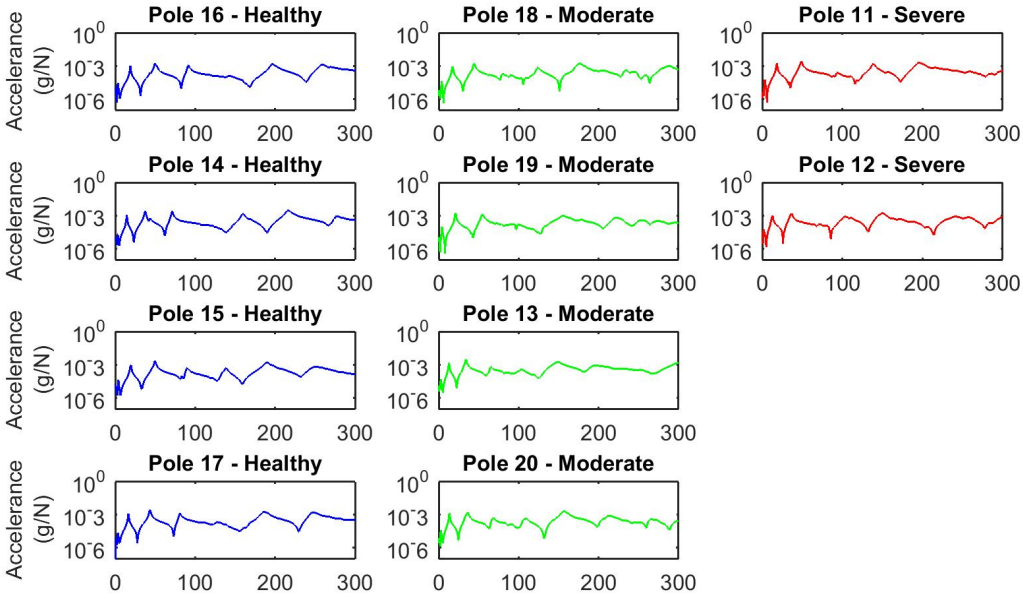

FIGURE 4.10: FRFs for vibrations about axis 2 from all poles in Set 2 grouped by decay severity

TABLE 3: Experimental estimates of natural frequencies (f_n) and damping ratios (ζ) from Axis 1 excitations

Pole 11			Pole 12			Pole 13		
Mode	f_n **(Hz)**	ζ (%)	**Mode**	f_n **(Hz)**	ζ (%)	**Mode**	f_n **(Hz)**	ζ (%)
1	3.78	9.2	1	2.03	28.1	1	2.27	13.4
2	19.32	2.2	2	12.39	4.3	2	11.71	3.7
3	49.75	2.1	3	35.32	3.2	3	32.07	3.1
4	91.94	1.6	4	68.34	2.7	4	66.28	4.2
5	143.55	1.4	5	103.92	2.5	5	98.04	3.0
6	205.40	1.3	6	149.31	2.0	6	143.69	2.7
7	262.39	1.6	7	208.49	1.9	7	207.10	5.5
8	-	-	8	246.74	2.9	8	301.08	3.4
9	-	-	9	288.24	1.9	9	-	-

Pole 14			Pole 15			Pole 16		
Mode	f_n **(Hz)**	ζ (%)	**Mode**	f_n **(Hz)**	ζ (%)	**Mode**	f_n **(Hz)**	ζ (%)
1	3.00	8.7	1	3.89	5.4	1	3.61	5.9
2	15.06	2.3	2	19.54	1.7	2	19.23	1.5
3	38.70	2.8	3	50.50	1.2	3	49.77	1.6
4	72.21	1.4	4	90.75	1.5	4	93.30	1.6
5	107.24	6.2	5	140.97	1.2	5	145.85	1.6
6	164.05	1.5	6	194.72	1.3	6	201.19	1.5
7	221.63	1.6	7	251.02	3.0	7	266.44	1.6
8	287.37	1.4	8	-	-	8	-	-

Pole 17			Pole 18			Pole 19		
Mode	f_n **(Hz)**	ζ (%)	**Mode**	f_n **(Hz)**	ζ (%)	**Mode**	f_n **(Hz)**	ζ (%)
1	3.49	29.7	1	4.15	20.3	1	3.68	8.1
2	16.35	2.5	2	17.69	2.3	2	20.36	2.4
3	43.15	1.6	3	44.86	2.1	3	54.91	2.4
4	81.46	1.7	4	81.07	1.9	4	112.53	3.8
5	125.40	2.7	5	127.86	3.6	5	150.80	2.7
6	186.21	2.2	6	182.44	3.3	6	219.70	3.3
7	252.07	2.3	7	242.68	2.2	7	270.29	4.5

Pole 20		
Mode	f_n **(Hz)**	ζ (%)
1	2.73	12.1
2	13.49	2.2
3	36.07	2.8
4	66.97	2.0
5	107.32	2.5
6	153.82	1.7
7	207.94	2.2
8	266.68	1.6
9	334.66	1.4

TABLE 4: Experimental estimates of natural frequencies (f_n) and damping ratios (ζ) from Axis 2 excitations

	Pole 11			Pole 12			Pole 13	
Mode	f_n **(Hz)**	ζ (%)	**Mode**	f_n **(Hz)**	ζ (%)	**Mode**	f_n **(Hz)**	ζ (%)
1	3.38	10.2	1	1.97	21.2	1	2.63	15.1
2	18.36	3.0	2	12.97	3.4	2	12.87	3.2
3	48.71	1.7	3	35.39	3.4	3	34.12	3.4
4	93.05	2.7	4	69.65	2.7	4	64.67	2.3
5	137.59	2.1	5	106.08	3.4	5	102.76	4.7
6	201.72	1.8	6	147.98	3.9	6	145.63	4.2
7	257.46	1.9	7	236.46	4.1	7	216.65	2.8
8	-	-	8	307.59	2.9	8	305.96	3.9

	Pole 14			Pole 15			Pole 16	
Mode	f_n **(Hz)**	ζ (%)	**Mode**	f_n **(Hz)**	ζ (%)	**Mode**	f_n **(Hz)**	ζ (%)
1	3.11	10.7	1	3.95	5.7	1	3.57	7.4
2	14.48	2.4	2	19.51	1.7	2	18.93	1.5
3	37.55	2.2	3	49.99	1.4	3	50.39	1.8
4	71.78	1.3	4	89.59	1.5	4	92.07	1.2
5	108.23	3.1	5	138.32	1.4	5	142.97	2.4
6	161.87	1.4	6	192.66	1.7	6	198.37	1.6
7	218.04	1.4	7	248.12	3.4	7	262.73	1.4
8	285.73	1.1	8	-	-	8	-	-

	Pole 17			Pole 18			Pole 19	
Mode	f_n **(Hz)**	ζ (%)	**Mode**	f_n **(Hz)**	ζ (%)	**Mode**	f_n **(Hz)**	ζ (%)
1	3.37	15.0	1	3.87	9.5	1	4.07	11.2
2	16.55	2.3	2	17.21	2.4	2	20.98	2.1
3	43.28	1.9	3	44.51	1.9	3	54.37	2.6
4	81.22	1.8	4	89.35	1.8	4	90.61	18.0
5	127.63	3.8	5	123.21	3.4	5	153.40	4.8
6	187.43	1.6	6	175.74	1.8	6	221.42	2.4
7	248.79	1.9	7	239.49	1.4	7	254.23	3.3

	Pole 20	
Mode	f_n **(Hz)**	ζ (%)
1	2.83	13.5
2	13.39	2.3
3	36.23	2.6
4	67.55	2.1
5	107.97	2.4
6	158.87	2.2
7	209.10	2.4
8	263.68	2.8
9	315.68	1.9

4.2 Performance Assessment of Condition Assessment Algorithm

The approach of parameter identification through model updating of a Rayleigh-Ritz model introduced in Barber (2016) was used to perform nondestructive condition assessment across the complete set of 20 poles tested in the laboratory. A summary of the Rayleigh-Ritz model and the model updating approach used to solve an inverse problem to identify unknown parameters in the model was summarized in Section 2.3 of this thesis, and so it will only be briefly reviewed here. This approach identifies values for three unknown parameters in a physics-based model of the pole-soil system. The first two parameters, E and E_s, represent the elastic modulus of the pole and the stiffness provided by the soil, respectively. The soil stiffness parameter describes the scope of a linear function that increases the soil spring constant with depth. A third parameter, DP, models the decay in the pole as uniform shell rot spanning the region 6 to 18 inches below ground and the magnitude of this parameter corresponds to the loss in area due to decay (ΔA) over the total original cross sectional area (A). The values for the unknown parameters are bounded to constrain the optimization search to realistic values. The elastic modulus of the pole is bounded from 1000 ksi to 3000 ksi, the soil modulus is bounded from 5 ksi to 50 ksi, and the decay parameter, DP is bounded from 0 to 1, where 0 represents no cross section loss and 1 represents total cross section loss. To quantify how well candidate solutions compare with the experimental measurements to inform the optimization, natural frequencies for the candidate models are calculated and compared to the experimentally measured natural frequencies of the pole. Following the recommendations from a parameter

identifiability study in Barber (2016), the objective function is taken as the sum of the absolute percentage prediction errors over the number of measured natural frequencies. A genetic algorithm with a population of 100 individuals, an elite count of 5 individuals, a crossover rate of 60%, and a fixed stopping point at 24 generations is used for the genetic algorithm. The solution from the genetic algorithm is then subject to a fmincon constrained local optimization routine to identify the set of parameters E, E_s, and DP that result in the strongest correlation between the natural frequencies of the model and the experimentally measured natural frequencies according to the objective function.

A summary of the results from the parameter identification, with the exception of the decay parameter results, for all 20 poles using each of the axis 1 and axis 2 natural frequency measurement data sets is shown in Figure 4.11a and Figure 4.11b, respectively. With the exception of Pole 18, the poles are ordered along the horizontal axis from left to right by increasing levels of decay, $(\frac{\Delta A}{A})_{max}$, determined by the destructive characterization previously described. They are also color-coded with blue, green, or red to signify the classification of healthy, moderate decay, or severe decay, respectively. Pole 18 was classified as a pole with moderate decay due to the significant amount of shake in the cross section that was unaccounted for by the digital image processing routine used to calculate the relative loss in cross sectional area of the pole. The justification for this decision is discussed in further detail later in this chapter. Since no reliable measure of $(\frac{\Delta A}{A})_{max}$ was available, it was ordered arbitrarily as the first of the poles with moderate decay.

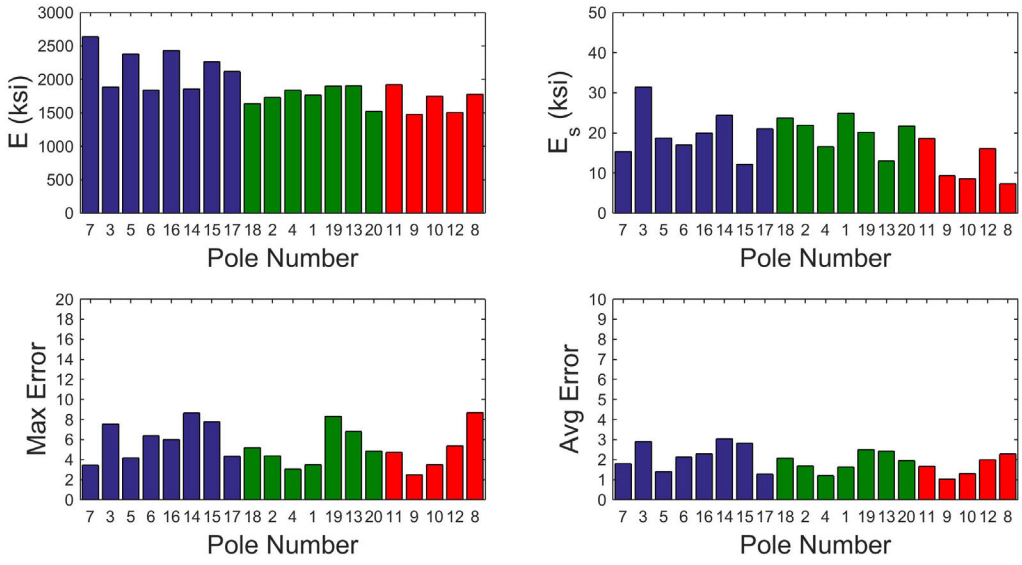

(a)

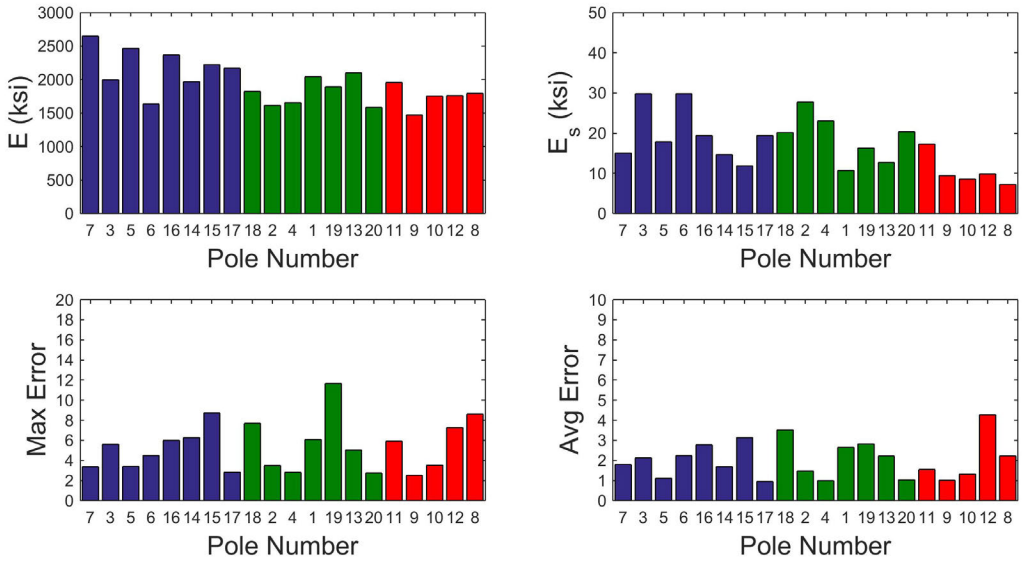

(b)

FIGURE 4.11: Summary of parameter identification results for complete set of laboratory poles based on transverse vibrations about: a) axis 1; b) axis 2

The average percentage error between the natural frequencies predicted by the updated analytical model and those measured experimentally was around 2%, which is consistent with the results found by Barber (2016). Maximum prediction errors

were also of similar magnitude. In general, there is little difference in the identified values of E between axis 1 and axis 2 of the poles, but there are some larger differences in the E_s values between the results for the two axes for some of the poles. There is also a slight correlation between the extent of decay and the values identified for E_s, which suggests that the model updating routine may slightly reduce the stiffness contributions from the soil to account for some of the loss in stiffness caused by decay.

The condition assessment was performed separately using data collected from vibration measurements about axis 1 and axis 2 in order to assess the performance of the condition assessment relative to the original formulation of the methodology and to assess the ability of the condition assessment method to detect asymmetric decay patterns in the poles. The identified decay parameter values for axis 1 and axis 2 are shown in Figure 4.12a and Figure 4.12b, respectively. Differences in the identified decay between the two axes can be explained in several poles by the presence of an asymmetric decay pattern that would result in different bending stiffnesses about the two axes. These instances of asymmetric decay and the ability of the model to identify asymmetric decay patterns will be discussed further in a later section of this chapter.

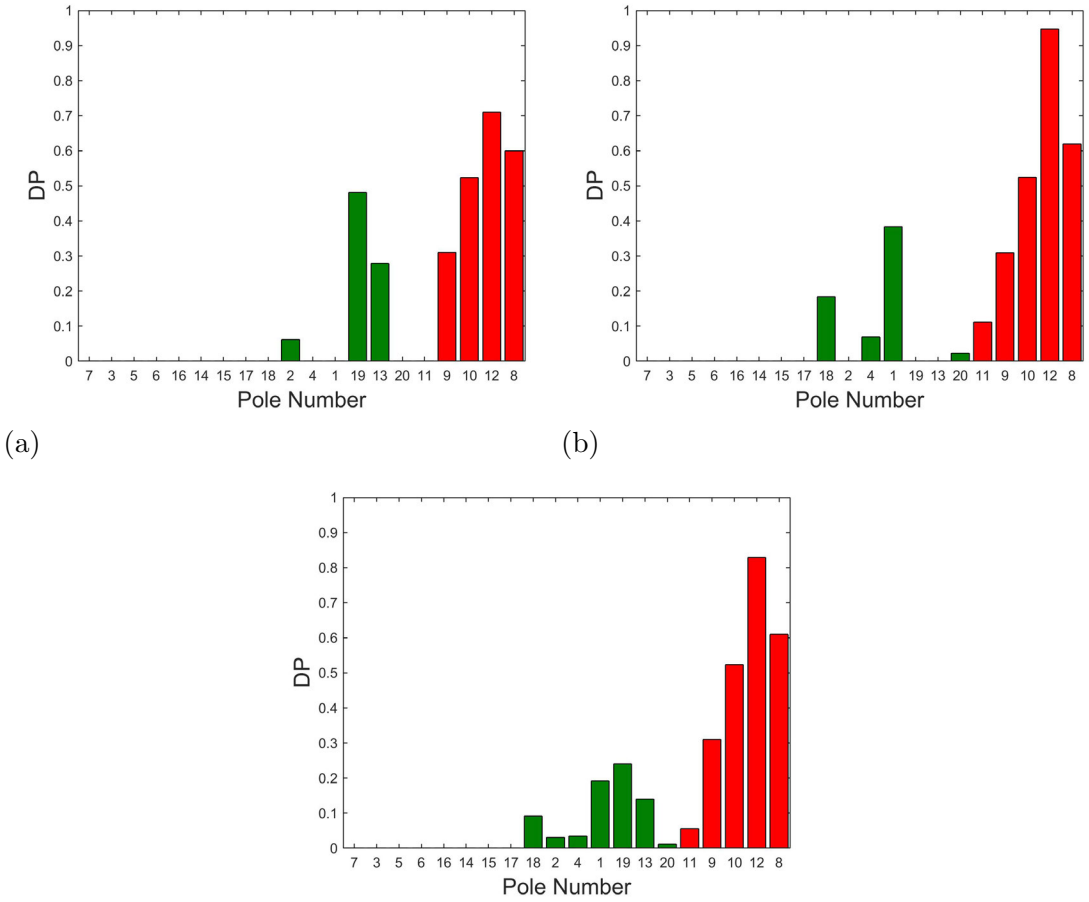

FIGURE 4.12: Identified decay (DP) in complete set of laboratory poles about a) axis 1 b) axis 2 c) average

A quantification of the overall decay in the poles was calculated as an average of the DP values for axis 1 and 2 (Figure 4.12c).The decay parameter values have a positive correlation with the actual decay $(\frac{\Delta A}{A})_{max}$, and the condition assessment procedure was generally successful in accurately classifying the poles according to the actual decay determined through destructive testing. A decay parameter of essentially zero was assigned to all of the poles classified as healthy so the method produced no false positives. Likewise, a classification of severe decay (>= 0.33) was identified for all of the poles that actually had severe decay with the exception of Pole 11 that was

still identified as having decay but only a low level of decay. This pole was the least decayed of the poles classified as severely decayed. Poles with moderate decay were typically classified appropriately ($0.10 <= DP <= 0.33$). However, while Poles 2, 4, and 20 were identified as having a decay parameter, the magnitude of the identified decay would incorrectly classify them as healthy despite having moderate decay. The misclassification of Pole 20 as healthy is not a particularly troubling concern, since the decay in Pole 20 extended above the ground line and could be readily be detected by a visual inspection. An interesting result obtained in this analysis was the identified decay for Pole 1, which was correctly identified as having moderate decay but was incorrectly identified as a healthy pole in Barber (2016). The improved classification is attributed to the analysis of the measurement axes independently rather than averaged, as the decay parameter for this pole was found to be significant only for the axis 2 response. The classification of Pole 11, which had severe decay, as a pole with less than 10% decay is of greater concern. Despite these issues, the testing described provided validation that the condition assessment method developed in Barber (2016) should continue to be developed for use in a device that can assist utility workers in accurately identifying and quantifying decay present in timber poles below the ground line.

4.2.1 Evaluation of Weighted Objective Function

During selection of the natural frequencies, it was observed that the second, third, and fourth resonance frequencies of a pole are typically represented by clean, sharp peaks in the frequency response function, allowing for a higher level of confidence in

the estimates of the natural frequencies corresponding to these modes. In contrast, the resonance frequencies for the higher modes in the measured bandwidth have duller peaks that are often not well-defined. As a result, the selection of the higher natural frequencies in the semi-automated system identification routine is more challenging and, consequently, the level of confidence associated with the natural frequency estimates of these modes is lower. The objective score for candidates in the original structural identification procedure is calculated as the sum of the absolute errors between the analytical natural frequencies and the corresponding experimental natural frequencies. With this equal weighting, large errors between any one natural frequency estimate predicted by the analytical model and the corresponding experimental natural frequency will result in a high objective score, eliminating the candidate from consideration in the search for a solution. High error already potentially present in the experimental natural frequency estimates could be construed by the optimization routine as a failure of a candidate to accurately model the soil-pole system. The uncertainty in the estimation of the frequencies associated with the higher modes in the excited bandwidth increases the likelihood that the parameter identification will be driven by error resulting from inaccuracies in the selected natural frequencies rather than true shifts caused by decay in the pole. To address this issue, a weighted objective function was developed and is shown below in (Equation 2).

$$J = \sum_{i=1}^{n} \alpha_i \frac{|f_i^{analytical} - f_i^{exp}|}{f_i^{exp}}, \qquad \alpha_i = n - i + 1 \tag{2}$$

In this alternative objective function, the absolute percentage error for each natural

frequency estimate is multiplied by a weighting factor, α, that is inversely proportional to the order of the bending mode, i. This weighted objective function places more importance on the absolute percentage errors for the lower bending modes, since the experimentally measured natural frequencies associated with these modes can be estimated with greater certainty than those associated with higher modes.

Results of the pole condition assessment method using this weighted objective function in place of the original objective function are summarized in Figures 4.13. In general, the results obtained are similar with some important differences. The identified values for E and E_s and the percentage errors of the model correlation are similar to those produced by the original objective function. To further evaluate the structural parameters identified for each axis, the ratio of the pole stiffness assignments produced for each axis was calculated to see if the axes developed consistent estimates. Likewise, the ratio of soil modulus values identified for each axis was calculated. The results indicate that there is little difference in the identified values of E between axis 1 and axis 2 poles (Figure 4.14a), which is to be expected, since the modulus of elasticity is a material property of the pole with only slight variations due to the inhomogeneous nature of timber. Greater variation exists between the E_s values identified for axis 1 and axis 2 (Figure 4.14b), and the E_s values identified for the two axes differs substantially in some poles. This asymmetry in the identified soil stiffness may be a result of the proximity of these poles to the stiffer concrete edge of the pit. For example, the ratio between the E_s values calculated for axes 1 and 2 is nearly 2.0 for Poles 12 and 13 and is over 2.5 for Pole 1. This asymmetry in the identified soil stiffness may be a result of the proximity of these poles to the stiffer

concrete edge of the pit. These poles were embedded in close proximity to the edge of the pit, and axis 1 was approximately parallel to the circumference of the pit at these locations. The concrete wall of the pit may be providing extra stiffness to the soil support condition in these instances.

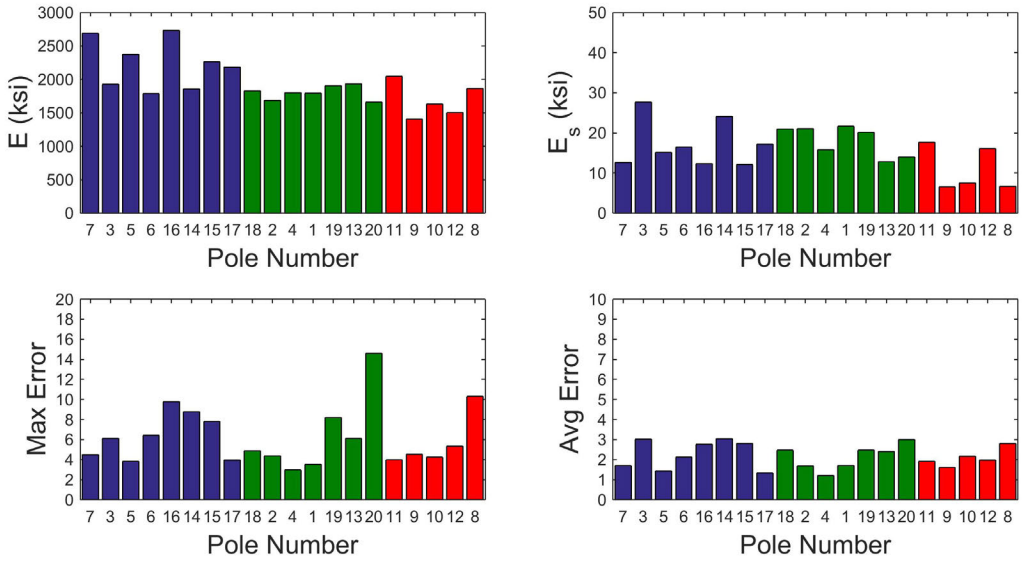

(a)

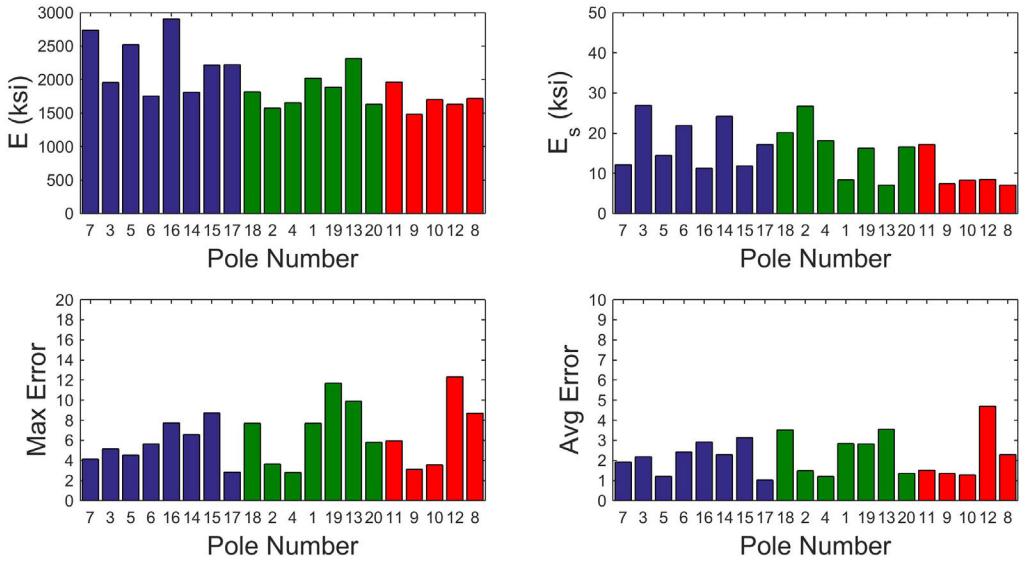

(b)

FIGURE 4.13: Summary of parameter identification results for complete set of laboratory poles using weighted objective function based on transverse vibrations about: a) axis 1; b) axis 2

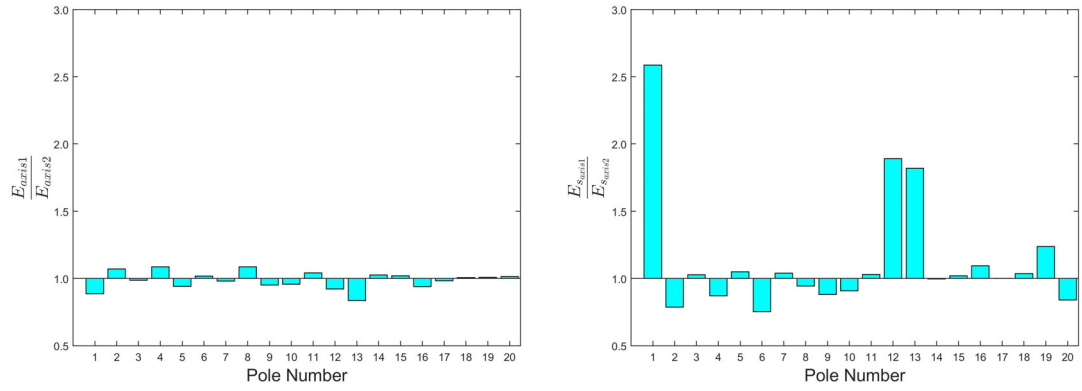

(a) (b)

FIGURE 4.14: Ratio between axis 1 and axis 2 structural identification results for a) the modulus of elasticity of pole (E); b) the elastic spring constant of soil (E_s)

The decay parameters identified by the pole condition assessment method using the weighted objective function differ in small but important ways from the decay parameters identified by the original formulation of the parameter identification (Figure 4.15). All of the poles classified by the parameter identification as healthy were correctly identified with decay parameters of essentially zero so no false positives were generated. Additionally, the four poles accurately classified as severely decayed by the unweighted condition assessment were assigned DP values more closely correlated with the actual decay $(\frac{\Delta A}{A})_{max}$. The classifications of decay for Poles 11 and 20 remained incorrect, but the levels of decay predicted in these poles increased toward a more accurate classification of the severity of decay. The identified decay in the poles is positively correlated with the actual decay as determined through the destructive characterization (Figure 4.16). These results suggest that the use of a weighted objective function may enhance the ability of the pole condition assessment method developed in Barber (2016) to accurately identify and quantify decay below

the ground line in timber utility poles.

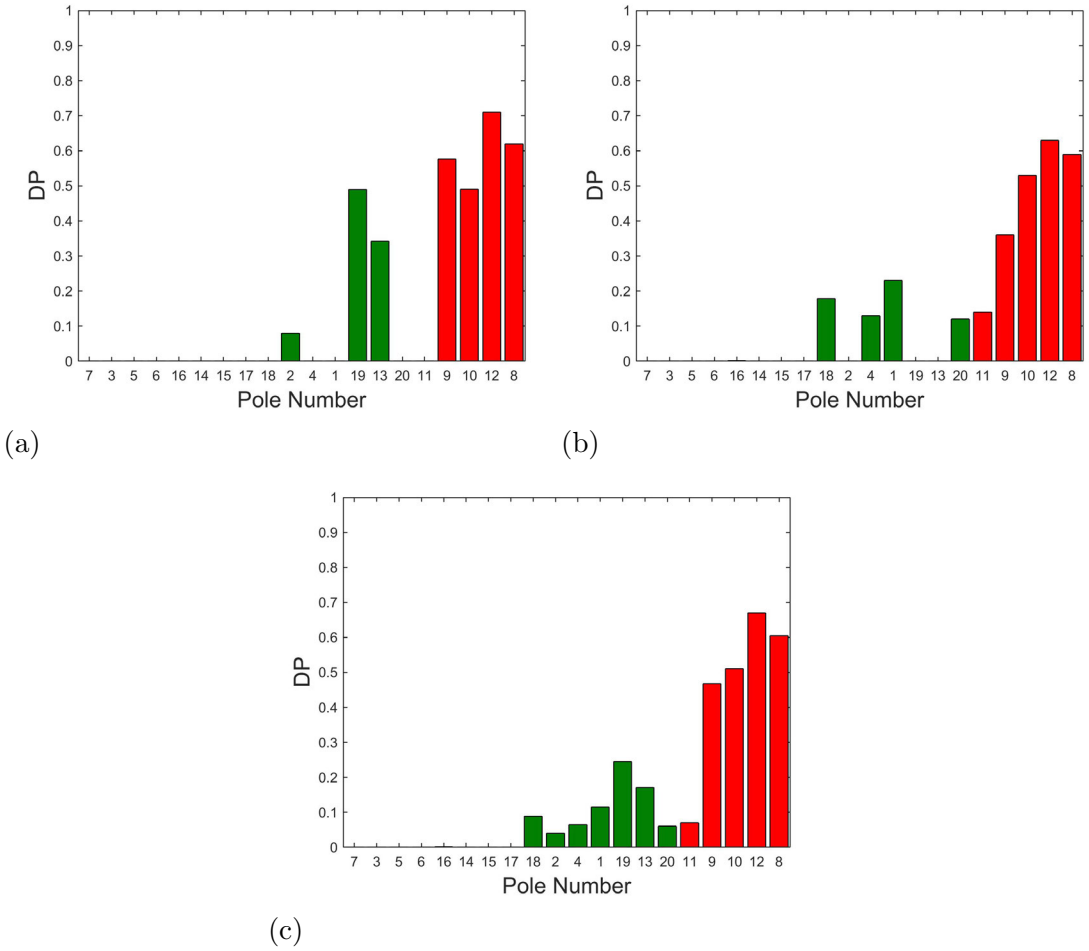

FIGURE 4.15: Identified decay (DP) in complete set of laboratory poles using weighted objective function about a) axis 1 b) axis 2 c) average

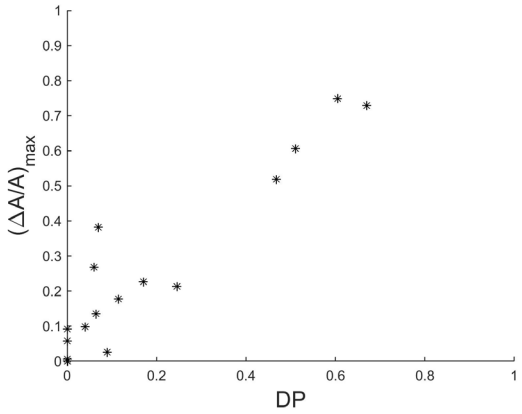

FIGURE 4.16: Comparison of actual decay and average decay parameter for complete set of laboratory poles

4.2.2 Accounting for Shake in the Damage Classification of Poles

The destructive testing method used to characterize the actual decay in the poles did not accurately account for the expected loss of stiffness associated with decay in pole 18 since this pole experienced ring shake that was not progressed to the extent that large areas of the cross section were lost. Ring shake, despite the lack of area loss, can produce a significant reduction in the bending stiffness and strength of timber poles (Wood et al., 1960). Since the digital image processing routine exploits the contrast between the dark pole cross section and the white background, the entire cross section was included in the area estimate for the slice, as shown in Figure 4.17a. However, a large portion of the pole in the lower left region of the cross sectional slice shown in the photograph is almost completely detached from the pole cross section as a result of the ring shake. Shear forces created in bending will not be transferred across separations in the pole caused by shake. Consequently, the fibers in the cross section do not act compositely, which leads to a reduction in the bending stiffness

and strength of the pole. The original estimate of actual damage calculated for this slice was small ($\Delta A/A = 0.03$), but this calculation did not account for the region of the cross section not acting compositely with the majority of the cross section due to shake. To produce an improved destructive classification of the extent of decay severity in this pole, the areas of the slice photographs affected by shake were colored white using a digital image editing software (Figure 4.17b). The cross sectional area of the slice was recalculated using the digital image processing routine described earlier in this chapter, resulting in a revised decay assessment of 0.17 for this particular slice. This extent of decay classifies Pole 18 as having moderate decay based on this more rigorous calculation of the actual area of the cross section that contributes to the overall bending stiffness of the pole. The average decay parameter computed for this pole with ring shake was 0.09 using the original objective function and 0.09 using the weighted objective function.

The inability of the digital image processing routine to directly account for shake shows that judgment is needed to give reasonable decay classifications to the poles during the destructive characterization used in the study to provide a basis for ground truth comparisons. This vulnerability also highlights the general imprecision of the destructive testing and ranking procedures used to quantify actual decay in the poles. Although the general extent of relative damage can be captured by this method of destructive testing, the exact ranking of the poles according to damage severity should be viewed with some degree of skepticism.

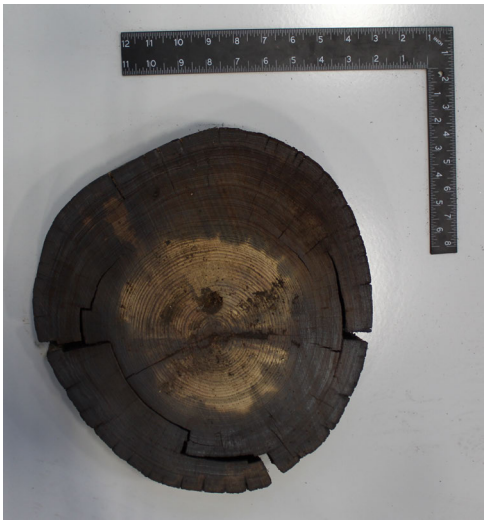

$(\frac{\Delta A}{A})_{max} = 0.03$

(a)

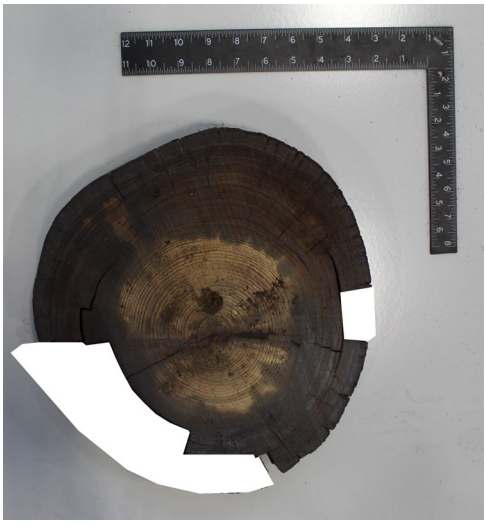

$(\frac{\Delta A}{A})_{max} = 0.17$

(b)

FIGURE 4.17: a) Cross section slice of Pole 18 containing significant shake; b) Region lost to shake eliminated from consideration in calculation of cross sectional area

4.2.3 Assessment of Performance of the Parameter Identification in Identifying Asymmetric Decay Patterns

Decay in a pole may be oriented so that it does not significantly reduce the bending stiffness about the axis chosen for vibration measurements. If the decay is located in close proximity to the bending axis where the contribution to flexural stiffness from the cross section is negligible, then it may not affect the modal properties of the pole in a way that can be detected using vibration measurements of the transverse bending modes about this axis. Using natural frequency measurements from vibrations excited along two orthogonal axes of a utility pole may allow the pole condition assessment method to detect asymmetric decay in the pole, if it exists. This capability would allow the method to identify decay that might be missed using either single-axis vibration measurements or averaged responses such as those used in the

prior study. Identifying the location of decay in the pole cross section could also inform the remediation of poles with moderate decay. Identifying the weak axis of bending would assist utility workers in selecting the optimum location for arresting decay and increasing bending stiffness through chemical treatments and the addition of pole reinforcements, respectively.

In several poles, the decay parameter assigned to axis 1 differed from the decay parameter assigned to axis 2 (Figure 4.18). In Poles 11, 13, and 18, the decay parameter assigned to one axis was negligible, and the decay parameter assigned to the other axis accounted for all of the decay identified by the method. Representative photographs of the cross sections of poles with asymmetric decay are shown in Figure 4.19. Asymmetric decay was correctly identified in all of the poles based based on the decay parameter values assigned to axes 1 and 2. For most of these cases, the bending axes evaluated in the test coincided well with the general orientation of the weak and strong axes of the decayed cross section. However, in Pole 20, neither axis 1 nor axis 2 correspond closely with either the strong or weak axis of bending. Based on visual observation of a representative photograph of the cross section, the weak axis of Pole 20 is located approximately 45 degrees between axis 1 and axis 2. The decay in Pole 20 is asymmetric, but this asymmetry is not oriented in a way that it reduces stiffness about one axis more than the other. As a result, the difference in the identified decay parameters for each axis of this pole is very small. It should be further noted that the identified decay in Pole 20 produced by the parameter identification was smaller than expected, which suggests that the orientation of the measurement axes relative to the actual weak and strong axes of the cross section may influence the absolute

accuracy of the decay severity estimation.

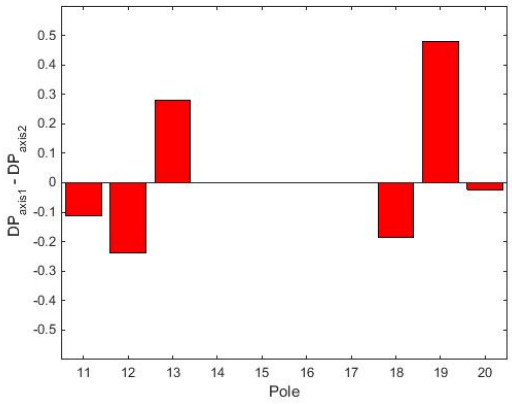

FIGURE 1.18: Asymmetry in decay between axis 1 and axis 2 ($DP_{axis1} - DP_{axis2}$) as predicted by parameter identification

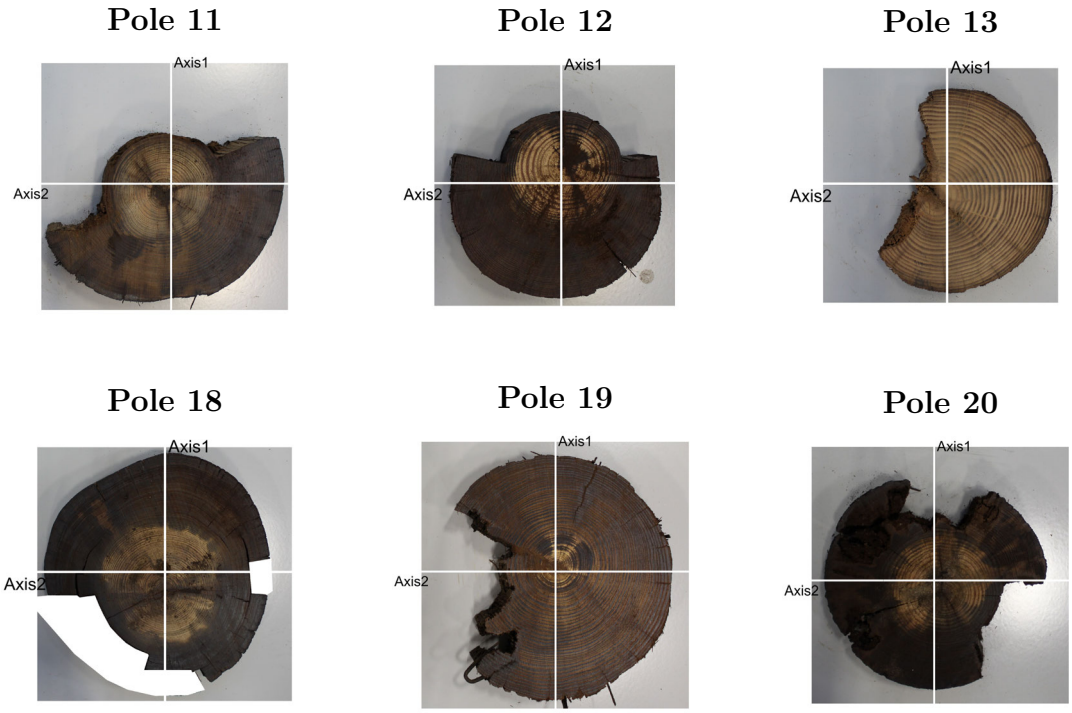

FIGURE 1.19: Representative photographs of slices from poles where the identified decay parameter was significantly asymmetric

4.3 Simulation of Asphalt Encasement Boundary Condition

Utility poles are often encased in a stiff paving material such as concrete or asphalt when installed in parking lots, sidewalks, or other paved locations. This additional stiffness at the ground line will alter the dynamic response of the utility pole. This common field condition was simulated in a laboratory setting to determine if the previously documented pole condition assessment procedure could accurately identify decay in poles encased in a paving material. A three to five inch layer of hot mix asphalt, donated by Blythe Construction, Inc., was shoveled into the pit and compacted using a hand tamp. The pole condition assessment procedure described in Section 2.3 was repeated on the poles encased by asphalt using the weighted objective function.

FIGURE 4.20: Asphalt encasement of the second set of ten poles in the experimental test pit

A summary of the results from the parameter identification of the poles in Set 2 when encased in asphalt is shown in Figure 4.21. Average and maximum absolute percentage error in the natural frequencies of the calibrated models were found to be similar to past results obtained without the asphalt encasement. The ratios of the identified E_s values between the case with asphalt and the case without asphalt are shown in Figure 4.22b. As expected, there was a general increase in the soil

stiffness assigned to the model, reflecting the additional stiffness added to the support condition by the asphalt encasement. There was also an increase in the values for the elastic modulus of the poles, though this increase is small compared to the increase of the values for E_s (Figure 4.22a).

The assigned decay parameter values for the Set 2 poles encased in asphalt are shown in Figure 4.23. While the methodology successfully identified decay in the most severely decayed pole and correctly identified all healthy poles with no false positives, the model was unsuccessful in identifying decay in several of the poles where it existed. No decay was identified in Poles 13 or 18 and only insignificant levels of decay were identified in poles 11 and 20, while all of these poles have moderate to severe decay. These results suggest that either condition assessment of poles with asphalt or concrete encasement is unreliable with the developed methodology or that changes in the physics-based model are necessary to account for the local stiffness contribution at the ground line provided by the asphalt. The addition of a spring representing the stiffness contributed by the asphalt encasement at the ground line may improve the model of the pole-soil system for cases of asphalt encasement.

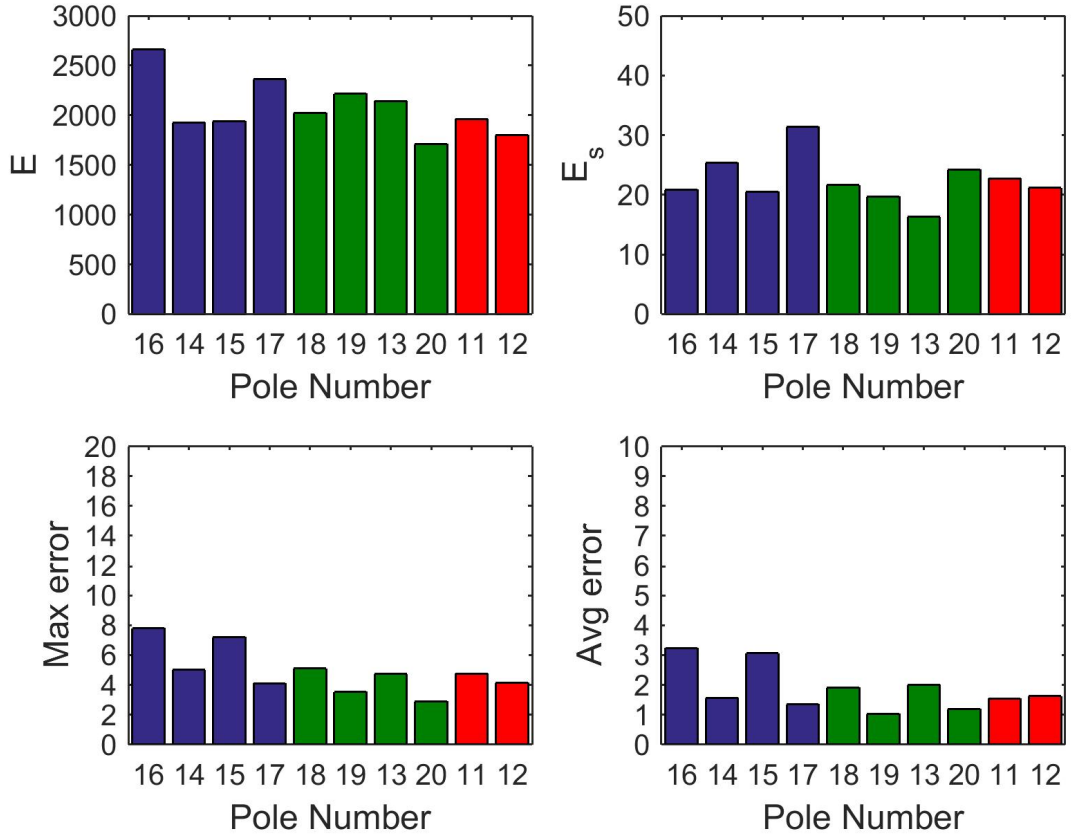

FIGURE 4.21: Summary of parameter identification results for Set 2 poles encased in asphalt

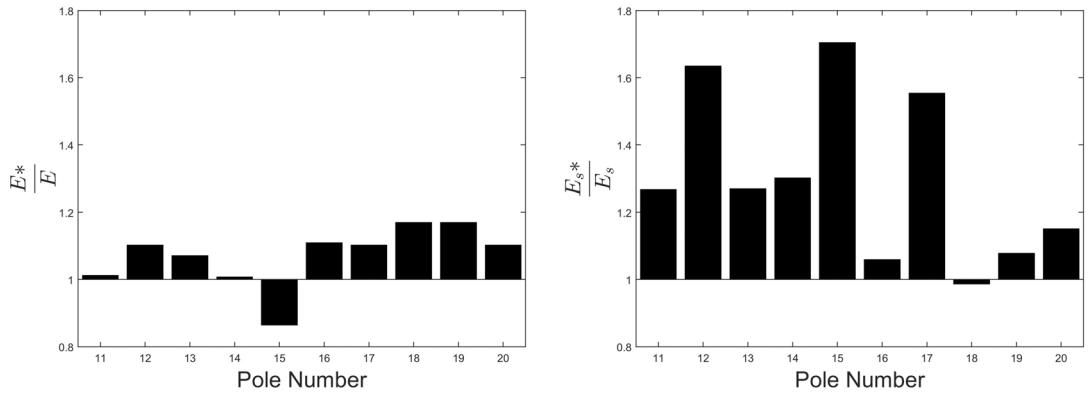

(a) (b)

FIGURE 4.22: Ratio of identified a) modulus of elasticity of pole (E); b) elastic stiffness of soil (E_s) between Set 2 poles with* and without asphalt encasement

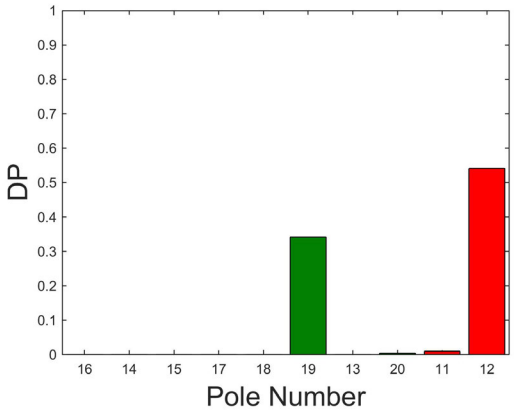

FIGURE 4.23: Average decay (DP) for Set 2 poles encased in asphalt

CHAPTER 5: INITIAL FIELD EVALUATION OF CONDITION ASSESSMENT TECHNIQUE

This chapter summarizes the field validation procedure and documents the results of the initial field assessment of the previously described pole condition assessment procedure in field conditions in contrast to the laboratory conditions. In-service poles may have additional mass from supported electrical infrastructure, such as conductors, insulators, transformers, and luminaires. In addition, conductors, guy wires, and pole reinforcements may introduce localized contributions in stiffness that have not yet been introduced into the physics-based model. The intention of this initial field evaluation is to assess the ability of the procedure to accurately identify and quantify decay in poles under common, realistic conditions. Utility poles identified by Duke Energy to be in need of immediate replacement are tested using the structural vibration procedure developed in the laboratory. Poles tested in the field are subsequently removed from service, and the portion of the poles previously embedded in the ground are characterized destructively to provide a basis for assessing the performance of the condition assessment technique.

5.1 Summary of Field Validation Test Program

The purpose of field validation is to evaluate the performance of the procedure developed in Barber (2016) on in-service poles with various configurations of rein-

forcement and supported infrastructure. Limitations identified during field testing can be addressed through further refinement in the laboratory environment and in subsequent field testing. Additionally, the development of this database of field testing measurements will allow for evaluating different approaches for compensating for the presence of supported infrastructure and reinforcements through mass and stiffness contributions in the Rayleigh-Ritz model.

The in-service poles tested during the initial field assessment were identified by Duke Energy to be poles in need of replacement. Most of these poles were deemed unfit for service through a conventional assessment. One pole was marked for reloca-tion due to a road expansion. Tests performed on this likely healthy pole may serve as a baseline for evaluation of the test method in field conditions. The in-service poles tested during the initial field assessment were nearing the end of the removal and replacement process, and at the time of testing, most of the supported infras-tructure had already been transferred to replacement poles. These poles were ready for immediate removal, which allowed for a quick and direct evaluation of the testing procedure in field conditions through destructive testing. The relatively simple field conditions of these poles also helped provide a bridge from the controlled laboratory environment to complex full in-service conditions.

The height, circumference, and pole taper of each pole were obtained either directly or indirectly using in situ measurements. The height measurement was estimated using a full length photograph of the pole next to a six foot height reference (Figure 1.1). Digital image processing was used to calculate the actual height of the pole based on the relative vertical pixel lengths calculated for the pole and the reference.

Circumference measurements were taken at the ground line and at an elevation of six feet to allow for a calculation of the diameter and taper of the pole (Figure 1.2). When risers, pole reinforcement, or other infrastructure prohibited a circumference measurement at either the ground line or the six foot elevation, the measurements were taken at two separate locations where the entire circumference of the pole was available, and the elevations of these locations were recorded. Prior to vibration testing, photographs were taken to document the supported infrastructure, support conditions, and general environment of the pole. Additionally, photographs were taken of unique features on the pole such as identifying tags, evidence of remedial treatment, or visible signs of damage due to decay, splitting, or woodpecker holes (Figure 1.3).

FIGURE 1.1: Example photograph of a pole with height reference used to estimate above ground height

(a)

(b)

FIGURE 1.2: Circumference measurements taken at a) ground line b) 6 feet above ground

FIGURE 1.3: Photograph of visible symptoms of decay in a pole near the ground line

Chalk was used to mark the pole at four feet, five feet, and six feet above the ground line in order to streamline the testing procedure. An aluminum utility pole tag was nailed into the pole at the five foot elevation along axis 1 to allow for identification of the pole, the location and orientation of the axes, and the elevation of the ground line after the field specimens were removed from service and shipped to the laboratory for destructive characterization (Figure 1.4). Vibration measurements were taken with both the wired commercial system and the wireless prototype described in the previous chapter, but only the measurements obtained from use of the wired system were used in the initial field assessment due to the measurement errors characterized

in the laboratory performance assessment of the prototype. The wired accelerometers were bonded to the prototype case, and the prototype case was secured to the utility pole with an adjustable hook and loop strap. This setup allowed for concurrent measurement by the two systems and provided a simple solution to the requirement of having a strong bond between the accelerometers and the pole. The procedure for recording vibration measurements is shown in Algorithm 1. Measurements were recorded for placement of the accelerometers at both the six foot elevation and at the four foot elevation. Testing at two different elevations was performed to provide additional data in the event that the field conditions lead to the six foot elevation, determined as ideal in the laboratory testing, no longer being suitable due to shifts in nodal points of the modes. At each of these locations, impulse excitations were applied at the six foot elevation and the four foot elevation in the direction of both axis 1 and axis 2 (Figures 1.5, 1.6). Impulse excitations in the direction of axis 3 (at 45 degrees from both axis 1 and axis 2) were not applied in the initial field assessment procedure.

FIGURE 1.4: Prototype and wired accelerometers secured to pole Pole 16 on Axis 1 at an elevation of 6 feet above ground

Algorithm 1 Protocol for vibration testing of in-service poles

Sensor placed at 6 ft elevation on Axis 1
Five hammer strikes at 6 ft elevation in direction of Axis 1
Five hammer strikes at 6 ft elevation in direction of Axis 2
Five hammer strikes at 4 ft elevation in direction of Axis 1
Five hammer strikes at 4 ft elevation in direction of Axis 2
Sensor placed at 4 ft elevation on Axis 1
Five hammer strikes at 6 ft elevation in direction of Axis 1
Five hammer strikes at 6 ft elevation in direction of Axis 2
Five hammer strikes at 4 ft elevation in direction of Axis 1
Five hammer strikes at 4 ft elevation in direction of Axis 2

(a) (b)

FIGURE 5.5: Impulse excitation of modes in direction of a) axis 1 b) axis 2

FIGURE 5.6: Impulse excitation of modes in direction of axis 2 at a) 6 feet b) 4 feet above ground

5.2 Initial Assessment of Field Measurements from a Limited Set of Poles

The initial field assessment discussed in this thesis documents the geometry and in situ condition of five in-service poles, provides initial observations on the modal characteristics of the poles obtained through vibration testing, and characterizes the actual decay in the five poles through destructive testing. A total of 29 in-service poles have been tested to date using the pole condition assessment method. However, the process of pole removal is lengthy, and only five poles were received at the time of preparing this thesis. The poles documented in this study are referred to as Pole 10 - Pole 14, corresponding to the ID tags UNCC10 - UNCC14 used in the field validation procedure described in Section 5.1.

5.2.1 Description of Field Specimens and Conditions

The geometric characteristics for the five poles tested in the initial field assessment are given in Table 6. The pole circumferences provided are estimates based on a linear extrapolation of the in situ measurements described in Section 5.1. The pole embedment depths were measured directly from the poles received after removal. Embedment depths could not be recorded for two of the poles tested, Pole 12 and Pole 13, because the embedded portion of these poles remained in the ground during removal due to detachment resulting from severe decay near the ground line. The pole lengths were calculated as the sum of the measured embedment depth and the estimated above ground height of the pole, except in the case of Pole 10 where the full length of the pole was received and could be directly measured. An embedment depth of 70", the mean embedment depth of the 20 poles tested in the laboratory, was

assumed for poles Pole 12 and Pole 13, producing uncertainty in the length estimates of these poles. Since the digital image processing routine described in Section 5.1 calculates the above ground height of the pole using the number of vertical pixels between user-selected locations of the top and the 1' elevation of the pole, additional will be introduced into the above ground height estimate if the pole is not straight or if if the orientation of the pole and/or reference height in the photograph is not exactly vertical. Additional error may be introduced by uneven ground line around the circumference of the pole or obstruction of the ground line location from tall grass and brush that makes the selection of the ground line elevation less certain. In all of these cases, the errors, if present, would tend toward a shorter estimate of the pole length than the actual pole length. As a verification check on the digital image processing approach for pole height estimation described in Section 5.1, the length for Pole 10 was measured directly after the pole was removed from the ground. The estimated length for Pole 10 based on the digital image processing in Section 5.1 was 24' 2", a difference of approximately 5" (1.7% absolute error). This comparison verifies that the pole height estimation procedure is capable of providing reasonable estimates of the above ground height of the utility poles during field validation. Note that the average pole length for the poles tested in the initial field assessment is several feet shorter than the average pole length of the laboratory poles. Poles scheduled for removal are often cut when the electrical and telecommunications infrastructure is transferred to a replacement pole in order to keep the upper region of the rejected pole outside of the area around the conductors supported by the adjacent replacement pole and to simplify the removal of the rejected pole. Since the poles tested in the

initial field assessment were near the end of the removal process, the poles had been cut down to a shorter length by the time when testing was performed.

TABLE 6: Measurements of geometric characteristics of timber utility poles tested in field conditions

Pole Number	**Pole Length**	**Pole Base Circumference***	**Pole Top Circumference***	**Pole Embedment Depth**
Pole 10	24' 7 "	34.7	26	6' 11 "
Pole 11	23' 5 "	32.7	28.5	6' 3 "
Pole 12	23' 7 "	30.1	28.1	-**
Pole 13	25' 1 "	38.0	23.3	-**
Pole 14	25' 11 "	33.2	30.1	6' 9 "

**Pole circumferences are estimates based on in situ measurements*
***Embedded portion of pole detached during removal process due to severe decay*

Destructive characterization of the poles was not performed in time to evaluate the method according the procedure documented in Chapter 4. Consequently, the method was assessed based on visual observations of the condition of the poles below the ground line. For reference, photographs of the pole slices for Poles 10, 11, and 14 are provided in Appendix F. Slicing could not be performed on Poles 12 and 13, since the embedded portions of these poles were lost during the process of pole removal. Photographs of the condition of each of the received poles below the ground line are presented in Figure 5.7. A summary of the general condition and characteristics of the five poles tested in the initial field assessment is given in Table 7. Based on the visible condition of the poles after being received in the laboratory, three of the poles in this set had severe decay below the ground line (Pole 11, Pole 12, and Pole 13). Pole 10 and Pole 14 appeared to be mostly healthy with some evidence of mild onset of decay. Photographs documenting the in situ condition of each pole at the ground

line are shown in Figure 5.8. Algae growth on Pole 10 can be seen near the ground line, suggesting the presence of consistent moisture and the possibility of conditions promoting decay. The original ground line of Pole 11 was covered with fresh soil excavated for the embedment of a replacement pole prior to the time of field testing. The photograph of Pole 12 shows the steel reinforcement used to reinforce this pole while in service. Algae growth and section loss from decay can also be seen at the ground line in the photograph of Pole 13.

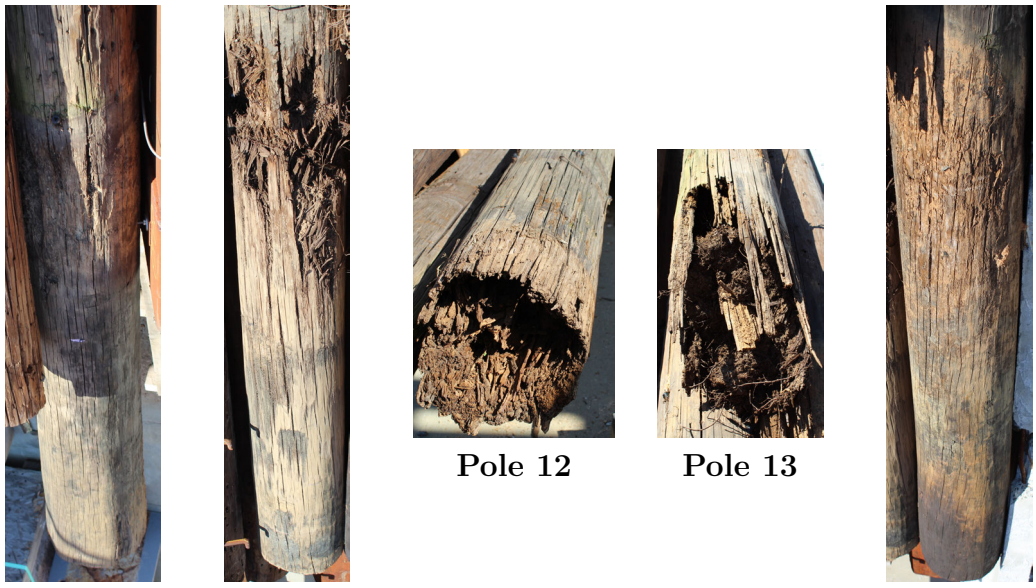

FIGURE 5.7: Pole profiles in region below the ground line. The embedded portion of Poles 12 and 13 were lost during pole removal.

TABLE 7: Description and condition summary of poles in initial field evaluation

Pole	Description of pole and condition
Pole 10	Mostly healthy with mild to moderate decay. Algae growth observed at ground line in situ. No supported infrastructure.
Pole 11	Severe decay just below ground line detected after pole removal. Supporting telecommunications lines in multiple directions
Pole 12	Reinforced with steel reinforcement while in-service. Algae growth observed at ground line in situ. Severe decay below the ground line resulting in loss of the embedded portion of the pole during removal.
Pole 13	Algae growth and section loss due to decay observed at ground line in situ. Severe decay below the ground line resulting in loss of the embedded portion of the pole during removal.
Pole 14	Mostly healthy with mild decay. Appears to be the healthiest pole tested in the initial field assessment.

Pole 10

Pole 11

Pole 12

Pole 13

Pole 14

FIGURE 5.8: Photographs of ground line conditions of poles tested in initial field assessment

Photographs of the infrastructure at the top of each pole are shown in Figure 5.9. The poles Pole 10, Pole 12 and Pole 14 are not supporting any infrastructure and, therefore, can be assumed to have a free support condition at the top. Pole 13, and Pole 14 were still supporting telecommunication lines at the time of testing. These lines may provide additional localized stiffness to these poles at the point of attachment. This is particularly true for Poles 11 and 13 where the telecommunication lines were also secured to the adjacent replacement pole. The short span of the telecommunications line leads to greater local stiffness than a typical span between normally spaced utility poles.

Pole 10

Pole 11

Pole 12

Pole 13

Pole 14

FIGURE 5.9: Photographs of electrical and telecommunications infrastructure supported by in-service poles tested in initial field evaluation

5.2.2 Evaluation of Vibration Measurements and Estimated Natural Frequencies

Averaged frequency response functions (FRFs) calculated using the vibration measurements recorded during the initial field assessment are shown in Figure 5.10. FRFs calculated from data measured at elevations of six feet and four feet are plotted together for each pole. For each FRF, the impulse excitations for these measurements were applied at the same elevation as the data measurement. Plotting measurements from two elevations assists in identifying or confirming natural frequencies in the system identification, since different distances from a nodal point in some modes may lead to a small or imperceptible peak near the resonance frequency of that mode in the FRF acquired for one elevation but a higher peak for the same mode in the FRF from another elevation where the relative amplitude of the mode shape may be higher. The acquired data shows clear instances where identification of a resonance frequency is significantly easier for one elevation relative to the other, so it is recommended that future field testing continues this practice of measuring the vibration response at multiple elevations. In general, the FRFs produced from vibration measurements in the initial field assessment were 'clean' with identifiable resonance peaks for the first five or six natural frequencies of the pole that were excited in the measured bandwidth of 300 Hz.

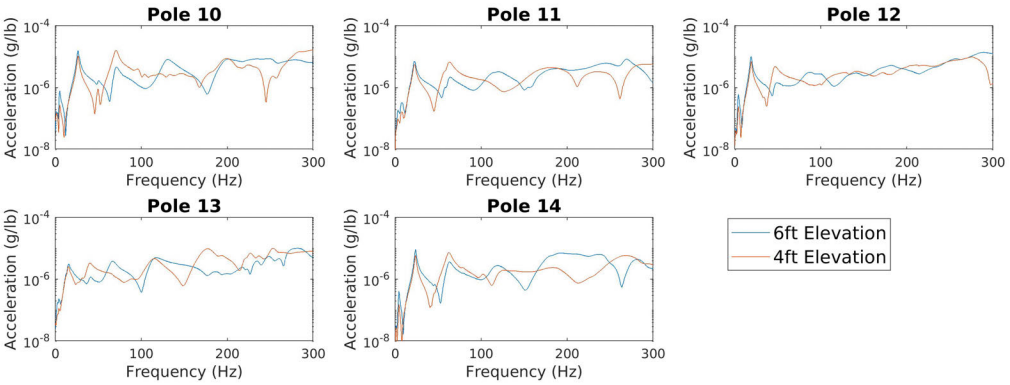

(a)

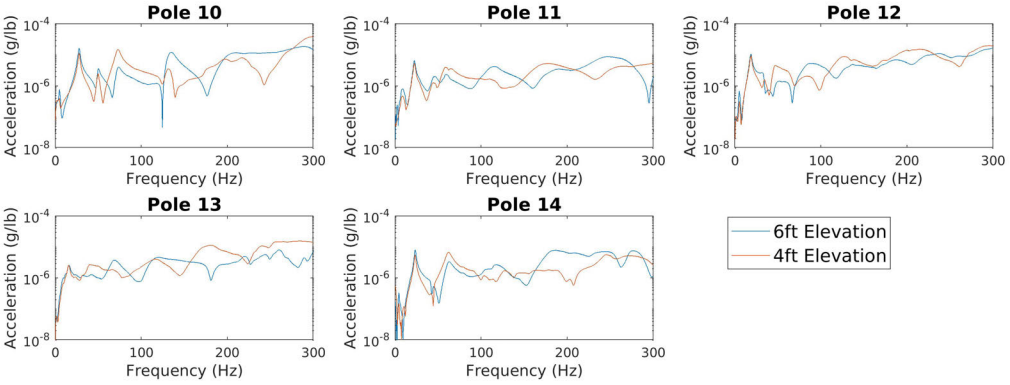

(b)

FIGURE 5.10: Frequency response spectra for in-service poles tested in field evaluation at 6ft and 4ft a) axis 1 b) axis 2

In the semi-automated routine used to perform the system identification, resonance peaks from both FRFs were used to produce the natural frequency estimates. When the resonance peak of a mode was clear in the FRFs from both elevations, the natural frequency selections from the two resonance peaks were averaged to obtain the natural frequency estimate for this mode. The experimental estimates of natural frequencies and damping ratios from axis 1 and axis 2 excitations of the poles tested in the initial field assessment are shown in Figure 8 and Figure 9, respectively. The natural frequencies of the field poles were generally higher than the corresponding natural

frequencies of the laboratory poles. This is most likely due to the shorter length of the field poles, which resulted in a stiffer pole and an upward shift in natural frequencies so that only the first five or six natural frequencies could be measured within the excited bandwidth.

There are several interesting observations in the field measurements that indicate differences in the pole responses from those tested in the laboratory. The fundamental natural frequency for Pole 11 and Pole 13 along axis 2 are significantly higher than the fundamental natural frequency estimates for other poles that have been tested in the laboratory and also higher than the fundamental natural frequencies for these same poles for bending about the other axis. The telecommunications supported by these poles ran parallel to the direction of the impulse for axis 2 measurements and were likely contributing additional localized stiffness to the pole at the attachment point which resulted in a higher fundamental frequency for these poles. Another observation is that the damping ratios for most poles are similar to those measured for the poles in the laboratory test bed. However, the damping associated with several of the modes of Pole 12 in both directions are higher. The increased damping is likely an effect caused by the steel reinforcement attached to this pole, since this is the primary distinguishing feature of this pole. While natural frequencies could still be estimated for this pole despite the higher damping ratios, the increased damping caused by the presence of ground line reinforcement may introduce additional challenges in the system identification of such poles since resonance is not as clearly evident in the FRF. There are also moderately high damping ratios associated with some of the modes of Pole 13 that may be a result of the large telecommunications line running

TABLE 1: Experimental estimates of natural frequencies (f_n) and damping ratios (ζ) from Axis 1 excitations of poles tested in the initial field assessment

	Pole 10			Pole 11			Pole 12	
Mode	f_n **(Hz)**	ζ **(%)**	**Mode**	f_n **(Hz)**	ζ **(%)**	**Mode**	f_n **(Hz)**	ζ **(%)**
1	5.02	14.1	1	6.87	27.1	1	4.13	16.0
2	26.19	3.6	2	22.19	5.7	2	18.93	6.0
3	69.99	3.9	3	61.99	5.4	3	45.84	7.2
4	129.93	5.9	4	116.10	9.1	4	86.00	19.6
5	198.12	7.3	5	176.17	12.1	5	123.98	13.0
6	287.23	4.3	6	246.02	8.2	6	177.65	8.4

	Pole 13			Pole 14	
Mode	f_n **(Hz)**	ζ **(%)**	**Mode**	f_n **(Hz)**	ζ **(%)**
1	4.13	25.7	1	4.28	14.7
2	14.95	11.7	2	23.43	4.3
3	39.42	8.6	3	62.14	5.6
4	65.31	7.6	4	117.92	7.2
5	113.88	8.1	5	185.55	7.9
6	182.64	7.3	6	266.39	7.0

TABLE 2: Experimental estimates of natural frequencies (f_n) and damping ratios (ζ) from Axis 2 excitations of poles tested in the initial field assessment

	Pole 10			Pole 11			Pole 12	
Mode	f_n **(Hz)**	ζ **(%)**	**Mode**	f_n **(Hz)**	ζ **(%)**	**Mode**	f_n **(Hz)**	ζ **(%)**
1	4.66	19.8	1	8.89	22.5	1	5.09	16.6
2	27.36	4.2	2	22.09	4.8	2	18.34	6.6
3	72.41	4.3	3	58.55	6.3	3	51.02	15.2
4	131.57	3.3	4	113.01	9.1	4	87.13	20.5
5	199.77	5.6	5	177.65	10.1	5	133.40	5.3
6	292.56	5.8	6	244.81	8.3	6	177.77	6.7

	Pole 13			Pole 14	
Mode	f_n **(Hz)**	ζ **(%)**	**Mode**	f_n **(Hz)**	ζ **(%)**
1	9.51	24.0	1	4.21	21.5
2	15.49	10.4	2	23.02	4.6
3	39.58	16.0	3	61.53	5.9
4	66.60	7.6	4	120.80	6.8
5	115.93	10.4	5	185.90	5.7
6	-	-	6	275.26	5.6

5.2.3 Application of Parameter Identification to Field Specimens

The natural frequencies obtained through the system identification were used to perform parameter identification with the Rayleigh-Ritz models for the poles tested in the initial field assessment. A summary of the parameter identification results, except for the identified decay parameter, are shown in Figure 5.11. Maximum percentage errors in the predicted natural frequencies were high for Pole 13, indicating that at least one of the natural frequencies identified in the system identification did not correlate well with the analytical natural frequency predicted by the model for the corresponding mode. However, for the other poles in the initial field assessment, the magnitudes of the maximum and average percentage errors in the predicted natural frequencies were generally similar to those obtained when evaluating the laboratory poles with this method. As in the laboratory testing, there is a correlation between the identified soil stiffness parameter, E_s, and the decay present in the pole. Furthermore, the identified values for E and E_s, while different across the set of poles tested, were generally consistent between the independent parameter identifications performed using the vibration measurements about axis 1 and axis 2.

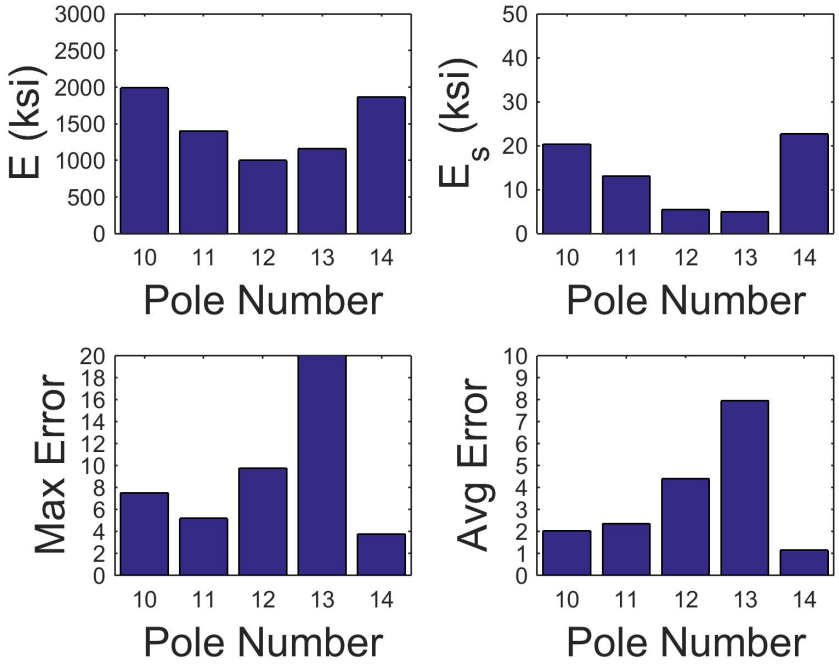

(a)

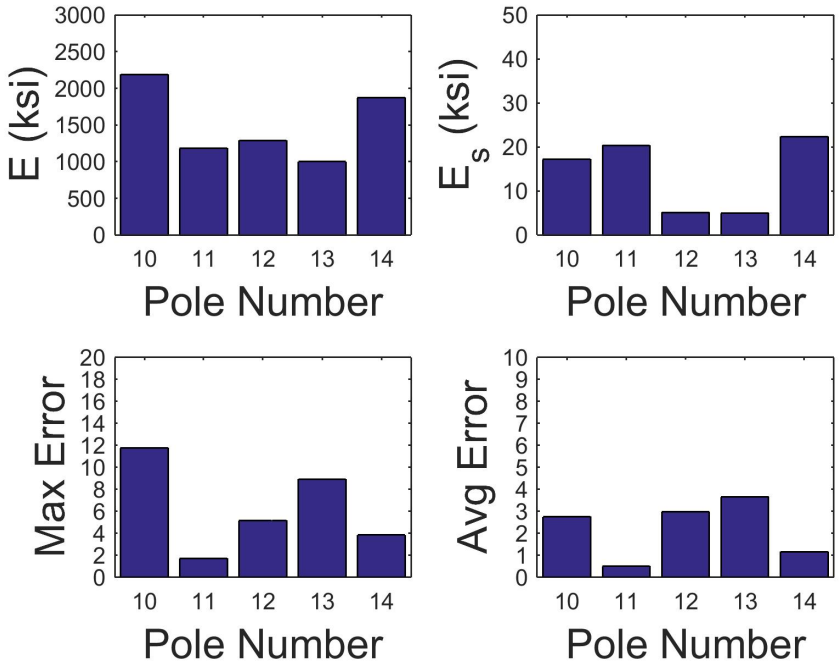

(b)

FIGURE 5.11: Summary of parameter identification results for poles tested in initial field assessment based on transverse vibrations about (a) axis 1 (b) axis 2

Results for the decay parameter obtained through the parameter identification of the poles tested in the initial field assessment are displayed in Figure 5.12 along with the average across the two axes.The results correlate well with the decay in the received poles based on visual observation of the pole condition and image analysis of cross sectional slices below the ground line. Pole 14, which was found through destructive characterization to have no decay below the ground line, was correctly identified as having a decay parameter of essentially zero for both axes, and so the method did not produce a false negative for this case. The average identified decay parameter results correctly indicate severe decay in Pole 13. High levels of moderate decay in Poles 11 and 12 were identified (DP = 28.0 and 25.1, respectively), and moderate decay was identified in Pole 10. The axis-specific decay parameters for Poles 10, 11 and 12 differ significantly and may indicate differing stiffnesses along the two axes. In fact, the method correctly identifies the orientation of asymmetric decay about axis 1 in Poles 10 and 11. The prediction of asymmetric decay in Pole 12 could not be confirmed, since the embedded portion of this pole was lost during removal. Additionally, the reinforcement on Pole 12 could be providing stiffness primarily along a single axis. The axis-specific decay parameters for Poles 10, 11, and 12 result in different classifications of decay for these poles. In Poles 10 and 11, this difference is due to asymmetric decay that resulted in only a low level of decay being identified about one axis. The different classifications about separate axes in these cases illustrate the importance of testing about multiple axes, since even severe decay may not be identified by a single axis test. It is recommended that future testing continue to utilize measurements about two orthogonal axes, not only to evaluate

the ability of the pole condition assessment method to identify asymmetric decay, but also to decrease the risk that severe decay will not be identified due to analysis of only a single-axis vibration test about the strong axis in a pole with asymmetric decay.

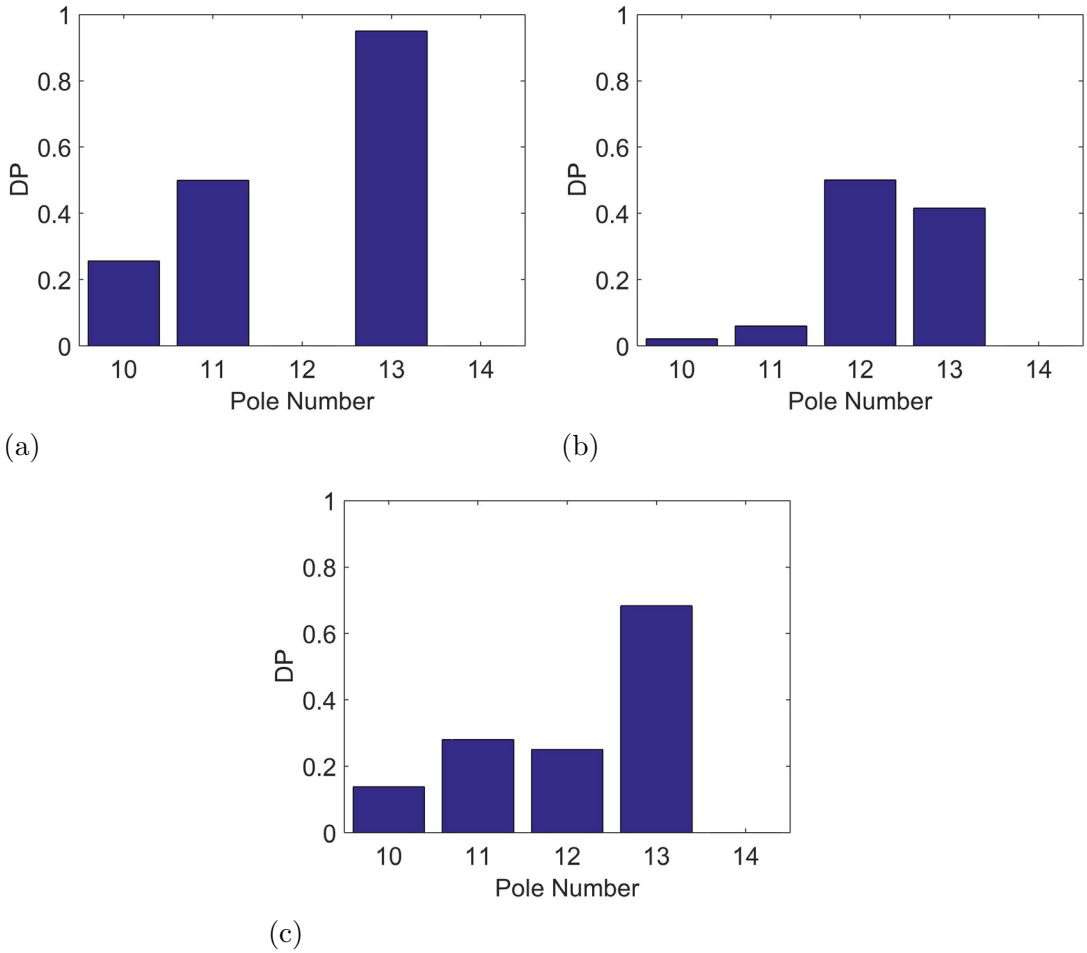

FIGURE 5.12: Identified decay parameter (DP) in poles tested in initial field assessment about a) axis 1 b) axis 2 c) average

5.3 Recommendation on Accelerometer for Field Applications

Vibration data was also collected on poles using higher range accelerometers with a full-scale acceleration limit of ±100g. The data collected with the higher range ac-

celerometers was collected on a separate set of poles than those previously discussed in this chapter. These poles are still in the replacement and removal process and have not yet been received for destructive characterization. The same PCB Piezotronics Model 086D20 impulse hammer was used to produce the impulse excitation except the hammer tip was replaced with the hard (black) tip. A harder tip increases the frequency bandwidth that is excited by the hammer impulse. The higher range accelerometer was used in an effort to measure more natural frequencies in the field poles within this larger excited bandwidth, especially given the generally higher frequencies resulting from the shorter length of these poles. The original ±5g accelerometers cannot be used to measure excitations from the black impulse hammer tip, since the resulting accelerations saturate the output of these lower range sensors. Using the ±100g accelerometers made it possible to measure these higher accelerations and compare the performance of the higher range accelerometer with the performance of the original ±5g accelerometers. The use of higher range accelerometers also allows the operator to strike the pole harder without saturating the output signal of the accelerometer. This may be important for practical implementation since pole utility workers are accustomed to striking the poles forcefully during the sounding procedure currently used to subjectively assess the pole condition. The higher range acceleration testing utilized two PCB Piezotronics 353B31 accelerometers temporarily bonded to a separate prototype case using hot glue (Figure 5.13). The accelerometers were oriented to measure vibrational modes along orthogonal axes using the same pole testing procedure explained in Algorithm 2.

Examples of the frequency response functions (FRFs) from the higher range ac-

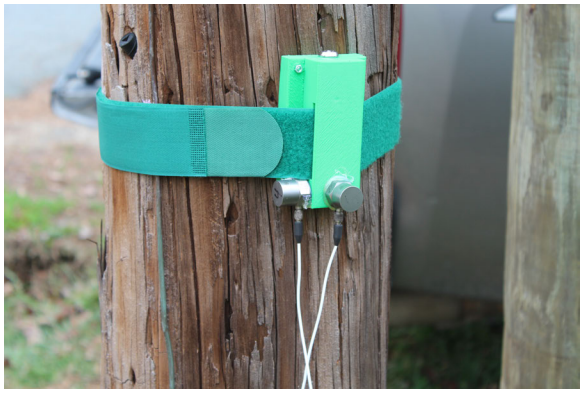

FIGURE 5.13: PCB Accelerometers with ±100g range bonded to prototype case and secured to pole

celerometer measurements with hard tip impulse hammer excitations are shown in Figure 5.14 alongside the corresponding FRFs calculated using vibrations measured on the same pole with the original lower range accelerometer measurements and excitations with a soft tip on the same impulse hammer. No significant differences are apparent in the resonance frequencies or in the quality of the resonance peaks between the measurement sets. This indicates that the use of a higher range accelerometer and impulse hammer with a harder tip are unlikely to yield a larger set of natural frequency estimates. Higher frequency content appears to be more significantly damped in the field measurements and only approximately six natural frequencies may be clearly defined in the measurement spectrum regardless of the instrumentation used. However, the anti-resonance peaks are more clearly defined in the FRFs measured by the higher range accelerometer. Although the pole condition assessment method does not utilize anti-resonance frequencies for the parameter identification, the anti-resonance frequencies of a pole are modal characteristics that are affected by the mass and stiffness of the pole-soil system, including any decay that may be

present. It is recommended that further testing be conducted using the higher range accelerometer and that the possibility of using anti-resonance frequencies to assist in parameter identification be explored. Furthermore, since the high range accelerometer did not degrade the quality of the frequency response function, it is recommended that a higher range accelerometer be used in field applications so that harder hammer strikes can be used without saturating the sensor output signal.

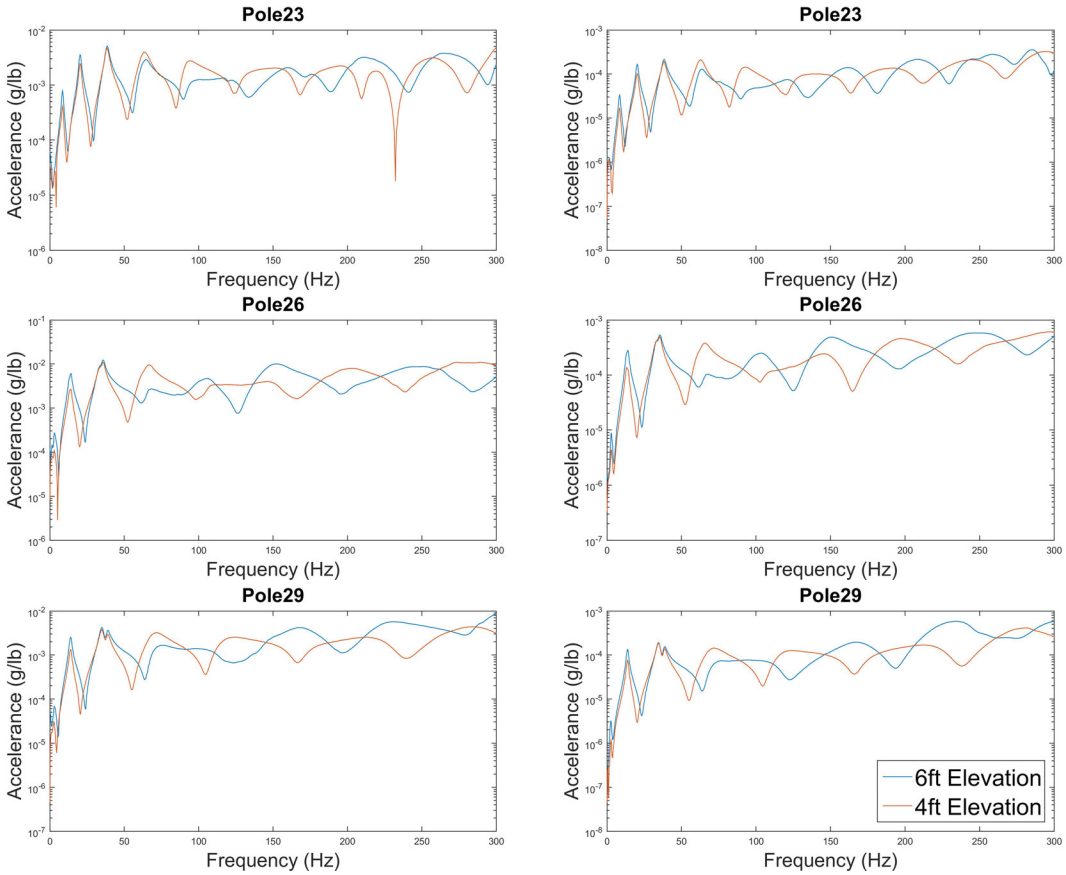

(a) (b)

FIGURE 5.14: FRFs from measurements recorded with a) original ±5g accelerometer measuring excitations from soft impulse hammer tip b) ±100g accelerometer from hard impulse hammer tip

CHAPTER 6: CONCLUSION

Over 160 million timber poles are used to support the electrical transmission and distribution systems in the United States alone (Mankowski et al., 2002). The widespread use of timber utility poles coupled with their long term susceptibility to decay that is not readily visible creates a need for methods that can rapidly inspect and evaluate the condition of a timber pole. Conventional inspection methods have a limited ability to assess the condition of a pole below the ground line, yet this is the region of the pole where decay is most likely to occur (Rural Utilities Service (2013)). A promising new vibration-based method utilizing natural frequency measurements to update a physics-based Rayleigh-Ritz model for parameter identification was developed by Barber (2016), and this method showed promise in accurately identifying and quantifying decay below the ground line in a set of ten timber utility poles embedded in a laboratory test pit.

One objective of this thesis was to validate the method developed in Barber (2016) through vibration testing of a second set of timber poles embedded in the same laboratory test pit. Vibration measurements for each pole were recorded for bending about orthogonal axes to further assess the ability to identify the orientation of asymmetric decay patterns found in some of the poles. The performance of the method was evaluated using a characterization of actual decay measured through destructive testing. The poles were removed from the ground, the embedded portion of each pole was

sliced using a band saw, and photographs were taken of each slice of the cross section. A digital image processing routine was used to calculate the section properties of the cross section from the photographs of the pole slices. Some limitations were observed in the ability of the destructive testing procedure to quantify damage in poles due to shake, and a refinement of the procedure was explored.

The original pole condition assessment method was generally successful in accurately classifying the second set of poles according to the severity of decay. All of the poles classified as healthy through destructive testing were assigned a decay parameter of essentially zero thereby producing no false positives. Poles with moderate to severe decay were also assigned non-zero decay parameters. However, two of the poles in the validation set were incorrectly classified by the nondestructive condition assessment method as having decay severities that would be considered below the threshold for moderate section loss, and one of these poles had severe decay present in the cross section. A weighted objective function was developed to mitigate the effect of the uncertainty associated with the natural frequency estimates of higher bending modes on the parameter identification results. Results obtained with this refinement of the method demonstrated improved characterization of decay in poles with severe and moderate section loss, while still correctly yielding no false positives when applied to healthy poles. Furthermore, the pole condition assessment method correctly identified the decay pattern orientation in five poles with asymmetric decay, suggesting that the method may be capable of detecting the azimuthal location of localized decay in the cross section. Vibration testing was repeated to evaluate the performance of the method in determining decay in timber poles encased in asphalt.

A three to five inch layer of hot mix asphalt was placed around the poles embedded in the test pit to simulate this common field condition in a laboratory setting. The reliability of the condition assessment technique was found to be compromised whtn applied to some of the poles with moderate to severe section loss.

A field validation procedure was developed, and in-service poles scheduled for immediate removal were tested using the vibration-based pole condition assessment method. The actual decay in the field poles was characterized through destructive testing. An initial evaluation of the ability of the method to produce accurate natural frequency estimates from vibration measurements of in-service poles was performed through analysis of the frequency spectra of the poles. The method produced 'clean' FRFs with clearly identifiable resonance peaks for the first five or six natural frequencies in the excited bandwidth of 300 Hz. FRFs from measurements at elevations of 6 feet and 4 feet were used concurrently to identify resonance peaks that were excited at only one of these elevation due to the proximity of the sensor to a nodal point along the pole. Fewer frequencies were excited in the field poles than in the laboratory poles due to the shorter average length of the field poles. The condition assessment was repeated with a measurements recorded with a higher range accelerometer with an acceleration limit of $\pm$100g and impulse excitations from an impulse hammer with hard tip in an effort to obtain more frequency measurements in the larger excited bandwidth. The higher range accelerometer testing resulted in no apparent changes in the resonance peaks of the FRFs, but the anti-resonance peaks were clearer in the higher range testing than in the original testing.

A first-generation prototype for the pole condition assessment device was devel-

oped that utilized a MEMS accelerometer and a single-board computer enclosed in a 3D printed case and configured to wirelessly to measure and record vibration measurements for the pole assessment routine. The performance of the prototype was evaluated in a laboratory setting. A wider tolerance in the sampling clock frequency of the low-cost MEMS accelerometer resulted in a discrepancy in the time base between concurrent measurements by the prototype and a high-end commercial reference system, and a device-specific calibration factor was developed to improve the accuracy of the natural frequencies measured by the prototype. Concurrent vibration measurements of pole excitations were measured by the prototype and the reference system to evaluate the ability of the prototype to produce accurate natural frequency estimates. The error between the natural frequency estimates of the prototype and those of the reference system was considered too high to justify continued use of the first-generation prototype for validation of the condition assessment method. A more refined device is ultimately needed in order to obtain the accurate measurements of natural frequencies needed to successfully complete the parameter identification for vibration-based condition assessment of timber distribution poles.

6.1 Recommendations for Future Work

The pole condition assessment method developed in Barber (2016) was validated as a suitable method for identifying and classifying decay in timber utility poles embedded in soil in a laboratory environment. The following areas of research are recommended in order to refine the pole condition assessment method for employment in a low-cost, portable, and rugged device that can rapidly assess the health of timber

utility poles below the ground line in field applications:

6.1.1 Prototype Development

A more sophisticated prototype is needed to obtain accurate natural frequency estimates of vibration in utility poles. Accurate measurements of the natural frequencies of the pole are critical to the success of the condition assessment method, and the error in the natural frequency estimates obtained from measurements by the prototype were too large to justify the continued use of the MEMS accelerometer utilized in this study. Specifically, the use of an accelerometer with a smaller tolerance in the sampling clock frequency would improve the accuracy of the time base of the measurement, which is critical to the reliable and accurate estimation of natural frequencies from the vibration response. Additionally, it is recommended that future iterations of the device utilize a fully-custom integrated board containing the accelerometer, CPU, and wireless capability, to avoid the inefficiencies resulting from features of commercially available components not necessary in this application.

6.1.2 Asymmetric Decay

In the laboratory testing performed in this thesis, the pole condition assessment method demonstrated the capability of accurately identifying and locating the orientation of decay in a pole when an asymmetric decay pattern existed. Locating the weak axis of bending in a timber pole could assist utility workers in identifying the optimal location for installation of pole reinforcement or application of remedial treatments of decay. Additional research is needed to validate and explore this apparent capability of the test method.

6.1.3 Parameter Identification

Utilizing a weighted objective function to drive the global optimization of the parameter identification led to noticeable improvements in the quantification of decay by the pole condition assessment method. This apparent refinement of the method should be validated with future testing, and additional modifications to the parameter identification that improve the utilization of available data should be explored. Specifically, natural frequency estimates from two orthogonal axes of the same pole could be used concurrently to increase the number of experimentally measured frequencies relative to the unknown parameters. Alternative forms of the objective function that use other measures of the prediction error or weighting functions should also be explored.

6.1.4 Field Validation

It is recommended that vibration measurements continue to be measured at multiple elevations, so that FRFs from both measurement locations can be utilized for system identification. It is also recommended that measurements continue to be taken along two orthogonal axes to evaluate the ability of the method to identify asymmetric decay and to reduce the risk of unidentified decay resulting from single-axis testing along the strong axis of a pole with an asymmetric pattern of decay. The use of a higher range accelerometer did not result in a greater number or a higher quality of natural frequency estimates. However, it is recommended that testing with the higher range accelerometer be used for field applications, since the higher range can measure the higher accelerations produced by harder hammer strikes with the hard tip of the

impulse hammer without saturation of the output signal of the sensor. Anti-resonance frequencies have not been utilized in the pole condition assessment method, but it is recommended that this potential refinement in the method be explored, since these modal characteristics are dependent upon the mass and stiffness properties of the pole, including any decay that may be present.

REFERENCES

ANSI, D. (2017). O5. 1 wood poles. *Specifications and Dimensions*.

ASTM (2015). Astm e1876: Standard test method for dynamic young's modulus, shear modulus, and poisson's ratio by impulse excitation of vibration. Technical report, ASTM.

Barber, E. (2016). Experimental evaluation of low-cost, portable, and rapid nondestructive evaluation methods for timber distribution poles. Master's thesis, University of North Carolina at Charlotte.

Birtz, R. E. (1979). Wood pole maintenance. *Journal of Arboricutlure*, 5(3):65–69.

Borges, C. C., Barbosa, H. J., and Lemonge, A. C. (2007). A structural damage identification method based on genetic algorithm and vibrational data. *International journal for numerical methods in engineering*, 69(13):2663–2686.

Brandt, A. (2011). *Noise and vibration analysis: signal analysis and experimental procedures*. John Wiley & Sons.

Chinchalkar, S. (2001). Determination of crack location in beams using natural frequencies. *Journal of Sound and vibration*, 247(3):417–429.

Chui, Y. H., Barclay, D. W., and Cooper, P. A. (1999). Evaluation of wood poles using a free vibration technique. *Journal of Testing and Evaluation*, 27(3):191,195.

Craighead, I., Thackery, S., Redstall, M., and Thomas, M. (2001). Monitoring wood decay in poles by the vibroacoustic response method. *Proceedings of the Institution of Mechanical Engineers, Part C: Journal of Mechanical Engineering Science*, 215(8):905–917.

Datla, S. and Pandey, M. (2006). Estimation of life expectancy of wood poles in electrical distribution networks. *Structural safety*, 28(3):304–319.

Daugherty, G. L. (1998). The realistic expectation of an in-place wood pole inspection program. *Wood Design Focus*, 9(2).

Fan, W. and Qiao, P. (2011). Vibration-based damage identification methods: a review and comparative study. *Structural health monitoring*, 10(1):83–111.

FHWA (2007). Measured variability of southern yellow pine - manual for LS-DYNA wood material model 143. FHWA-HRT- 04-097, United States Department of Transportation Federal Highway Administration.

Franklin, D. E., Murphy, M. W., and Palylyk, R. A. (1990). Apparatus and method for testing wooden poles. US Patent 4,926,691.

Friswell, M., Penny, J., and Garvey, S. (1998). A combined genetic and eigensensitivity algorithm for the location of damage in structures. *Computers & Structures*, 69(5):547–556.

Hassiotis, S. and Jeong, G. D. (1995). Identification of stiffness reductions using natural frequencies. *Journal of engineering mechanics*, 121(10):1106–1113.

Ilanko, S., Monterrubio, L., and Mochida, Y. (2015). *The Rayleigh-Ritz method for structural analysis*. John Wiley & Sons.

Juang, J.-N. and Pappa, R. S. (1985). An eigensystem realization algorithm for modal parameter identification and model reduction. *Journal of guidance, control, and dynamics*, 8(5):620–627.

Khiem, N. and Toan, L. (2014). A novel method for crack detection in beam-like structures by measurements of natural frequencies. *Journal of Sound and Vibration*, 333(18):4084–4103.

Kim, Y., Ranjithan, S., Donato, P., and Murphy, C. (2000). Nondestructive evaluation of the structural condition of timber piles. Final Report FHWA/NC/2000-004, North Carolina Department of Transportation.

Krause, M., Dackermann, U., and Li, J. (2015). Elastic wave modes for the assessment of structural timber: ultrasonic echo for building elements and guided waves for pole and pile structures. *Journal of Civil Structural Health Monitoring*, 5(2):221–249.

Krautkrämer, J. and Krautkrämer, H. (2013). *Ultrasonic testing of materials*. Springer Science & Business Media.

Lee, J. (2009). Identification of multiple cracks in a beam using natural frequencies. *Journal of sound and vibration*, 320(3):482–490.

Mankowski, M., Hansen, E., and Morrell, J. (2002). Wood pole purchasing, inspection, and maintenance: A survey of utility practices. *Forest Products Journal*, 52(11):43–50.

Mares, C. and Surace, C. (1996). An application of genetic algorithms to identify damage in elastic structures. *Journal of sound and vibration*, 195(2):195–215.

Morrell, J. J. (2008). *Estimated Service Life of Wood Poles*. North American Wood Pole Council.

Mottershead, J. and Friswell, M. (1993). Model updating in structural dynamics: a survey. *Journal of sound and vibration*, 167(2):347–375.

Peterson, S., McLean, D., Symans, M., Pollock, D., Cofer, W., Emerson, R., and Fridley, K. J. (2001). Application of dynamic system identification to timber beams. ii. *Journal of Structural Engineering*, 127(4):426–432.

Piter, J., Zerbino, R., and Blaß, H. (2004). Effectiveness of fundamental resonant frequency for determining the elastic properties of argentinean eucalyptus grandis in structural sizes. *Holz als Roh-und Werkstoff*, 62(2):88–92.

Rural Utilities Service (2011). *RUS Bulletin 1728F-700: RUS Specification for Wood Poles, Stubs and Anchor Logs*. United States Department of Agriculture.

Rural Utilities Service (2013). *RUS Bulletin 1730B-121: Wood Pole Inspection and Maintenance*. United States Department of Agriculture.

Salawu, O. (1997). Detection of structural damage through changes in frequency: a review. *Engineering structures*, 19(9):718–723.

Tedesco, J. W. (1998). *Structural Dynamics: Theory and Applications*. Addision Wesley Longman, Inc.

Wood, L. W., Erickson, E. C. O., Dohr, A., et al. (1960). Strength and related properties of wood poles. Citeseer.

Yan, N. (2015). *Numerical Modeling and Condition Assessment of Timber Utility Poles using Stress Wave Techniques*. PhD thesis, University of Technology, Sydney.

APPENDIX A: POLE GEOMETRIES AND PROPERTIES

Pole 11

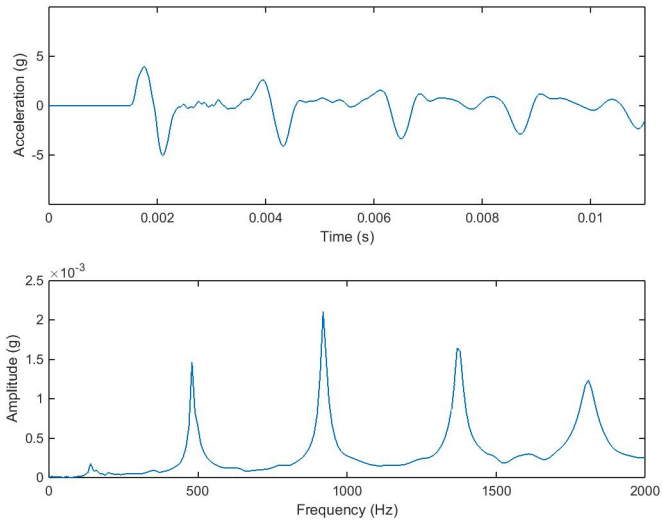

Total Pole Length	332.0 in (8.43 m)
Embedment Depth	75.0 in (1.91 m)
Base Circumference	34.75 in (88.27 cm)
Top Circumference	26.5 in (67.31 cm)
Marking	None
Inspection Tag	None

Length of Wave Speed Specimen	207.5 in (5.27 m)
Frequency of Wave Reflections	450 Hz
Longitudinal Wave Speed, C_p	186,750 in/s (4,743 m/s)
In-Situ Density, ρ	35.83 lb/ft^3 (574.0 kg/m^3)
Moisture Content	11.03 %
Longitudinal Elastic Modulus, E_L	1,873 ksi (12,915 MPa)

Pole 12

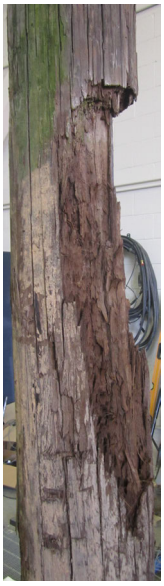

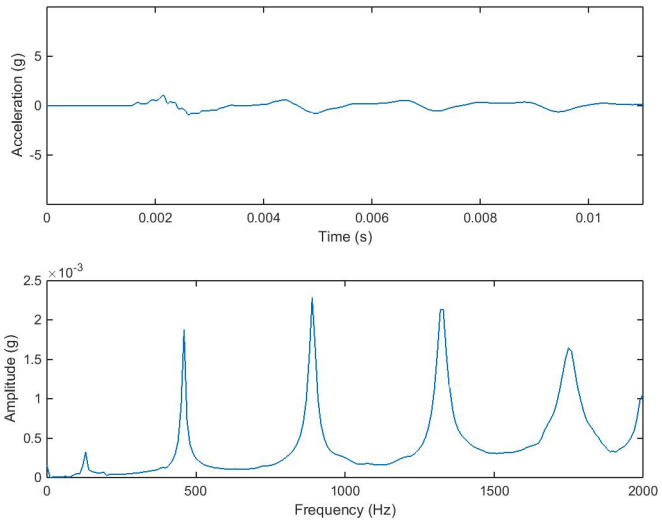

Total Pole Length	358.0 in (9.09 m)
Embedment Depth	75.0 in (1.91 m)
Base Circumference	35.25 in (89.54 cm)
Top Circumference	22.75 in (57.79 cm)
Marking	None
Inspection Tag	None

Length of Wave Speed Specimen	232.6 in (5.91 m)
Frequency of Wave Reflections	450 Hz
Longitudinal Wave Speed, C_p	209,363 in/s (5,318 m/s)
In-Situ Density, ρ	34.92 lb/ft^3 (559.4 kg/m^3)
Moisture Content	9.55 %
Longitudinal Elastic Modulus, E_L	2,294 ksi (15,820 MPa)

Pole 13

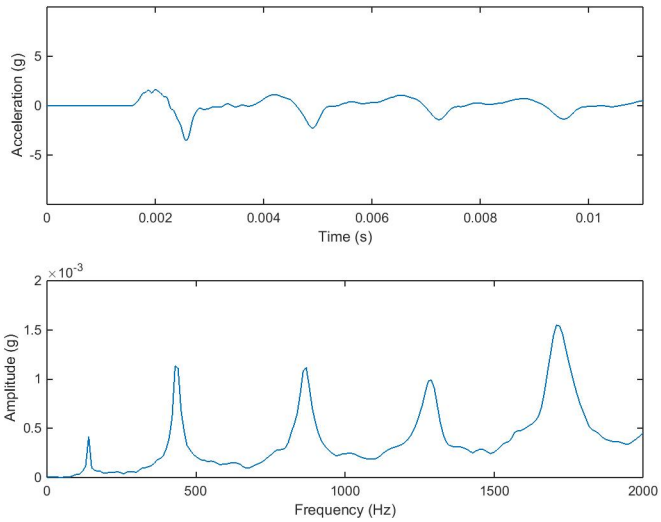

Total Pole Length	360.00 in (9.14 m)
Embedment Depth	70.25 in (1.78 m)
Base Circumference	25.5 in (64.77 cm)
Top Circumference	20.75 in (52.71 cm)
Marking	None
Inspection Tag	None

Length of Wave Speed Specimen	240.9 in (6.12 m)
Frequency of Wave Reflections	430 Hz
Longitudinal Wave Speed, C_p	207,152 in/s (5261.7 m/s)
In-Situ Density, ρ	30.47 lb/ft^3 (488.1 kg/m^3)
Moisture Content	11.5 %
Longitudinal Elastic Modulus, E_L	1,9600 ksi (13,514 MPa)

Pole 14

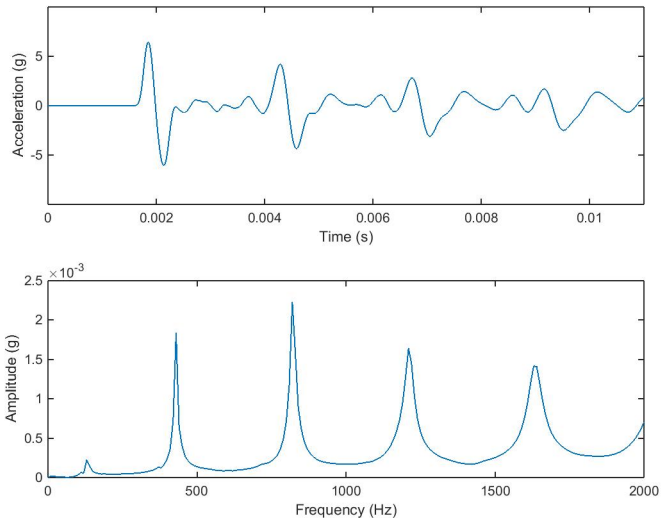

Total Pole Length	360.0 in (9.14 m)
Embedment Depth	60.5 in (1.54 m)
Base Circumference	35.5 in (90.17 cm)
Top Circumference	24.0 in (60.96 cm)
Marking	None
Inspection Tag	None

Length of Wave Speed Specimen	216.5 in (5.50 m)
Frequency of Wave Reflections	460 Hz
Longitudinal Wave Speed, C_p	199180.0 in/s (5,059.2 m/s)
In-Situ Density, ρ	39.25 lb/ft^3 (628.8 kg/m^3)
Moisture Content	10.8 %
Longitudinal Elastic Modulus, E_L	2,101 ksi (14,485.9 MPa)

Pole 15

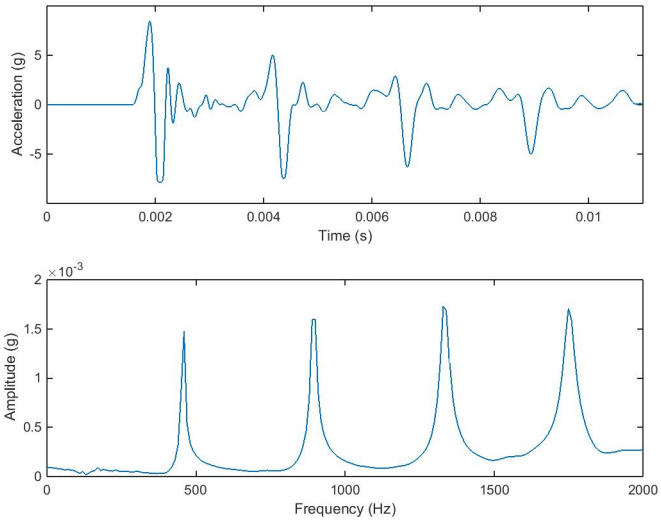

Total Pole Length	330.0 in (8.38 m)
Embedment Depth	61.0 in (1.55 m)
Base Circumference	39.0 in (99.06 cm)
Top Circumference	27.5 in (69.85 cm)
Marking	None
Inspection Tag	None

Length of Wave Speed Specimen	218.9 in (5.56 m)
Frequency of Wave Reflections	440 Hz
Longitudinal Wave Speed, C_p	192,610 in/s (4892 m/s)
In-Situ Density, ρ	45.80 lb/ft^3 (733.6 kg/m^3)
Moisture Content	11.6 %
Longitudinal Elastic Modulus, E_L	2,547 ksi (17,559 MPa)

Pole 16

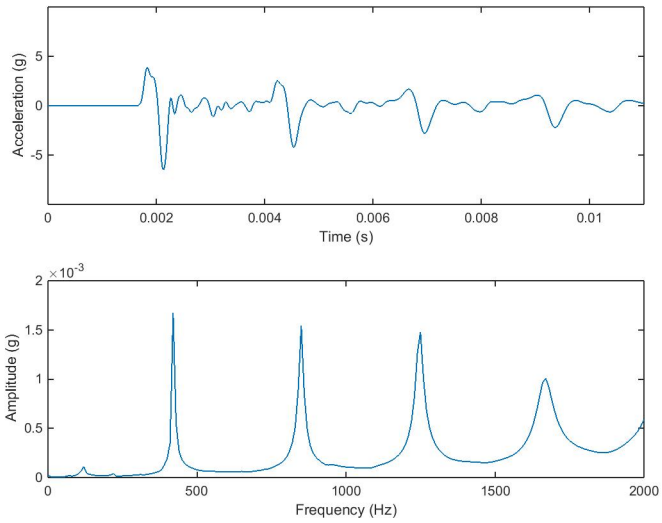

Total Pole Length	355.0 in (9.02 m)
Embedment Depth	70.0 in (1.78 m)
Base Circumference	36.0 in (91.44 cm)
Top Circumference	29.0 in (73.66 cm)
Marking	None
Inspection Tag	None

Length of Wave Speed Specimen	235.4 in (5.98 m)
Frequency of Wave Reflections	420 Hz
Longitudinal Wave Speed, C_p	197,715 in/s (5,022 m/s)
In-Situ Density, ρ	38.24 lb/ft^3 (612.5 kg/m^3)
Moisture Content	9.8 %
Longitudinal Elastic Modulus, E_L	2,240 ksi (15,448 MPa)

Pole 17

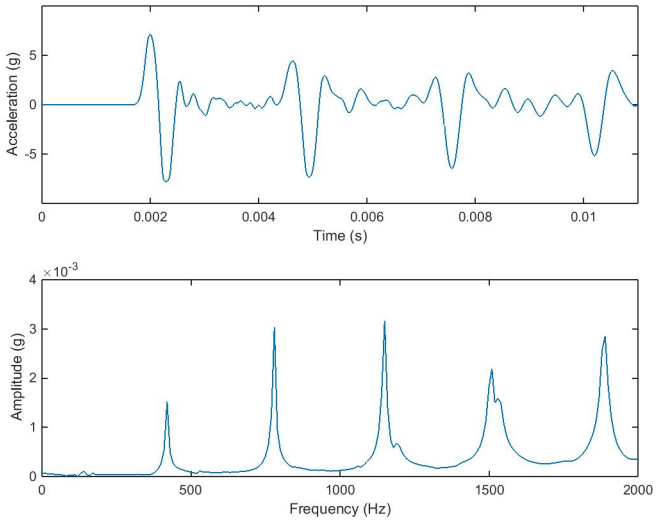

Total Pole Length	360.0 in (9.14 m)
Embedment Depth	74.5 in (1.89 m)
Base Circumference	34.0 in (86.36 cm)
Top Circumference	25.0 in (63.50 cm)
Marking	ATT-6 KOP FL-11-14 SPSK60 5-30
Inspection Tag	None

Length of Wave Speed Specimen	233.3 in (5.92 m)
Frequency of Wave Reflections	380 Hz
Longitudinal Wave Speed, C_p	177270 in/s (4503 m/s)
In-Situ Density, ρ	28.91 lb/ft^3 (463.0 kg/m^3)
Moisture Content	13.2 %
Longitudinal Elastic Modulus, E_L	1362 ksi (9387 MPa)

Pole 18

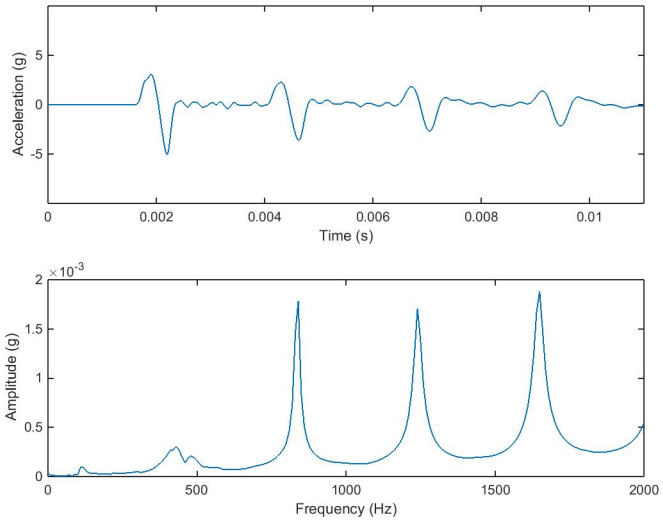

Total Pole Length	354.5 in (9.00 m)
Embedment Depth	75.5 in (1.91 m)
Base Circumference	40.0 in (101.60 cm)
Top Circumference	25.5 in (64.77 cm)
Marking	None
Inspection Tag	None

Length of Wave Speed Specimen	227.5 in (5.78 m)
Frequency of Wave Reflections	410 Hz
Longitudinal Wave Speed, C_p	186,550 in/s (4738 m/s)
In-Situ Density, ρ	32.54 lb/ft^3 (521.2 kg/m^3)
Moisture Content	10.0 %
Longitudinal Elastic Modulus, E_L	1,697 ksi (11,701 MPa)

Pole 19

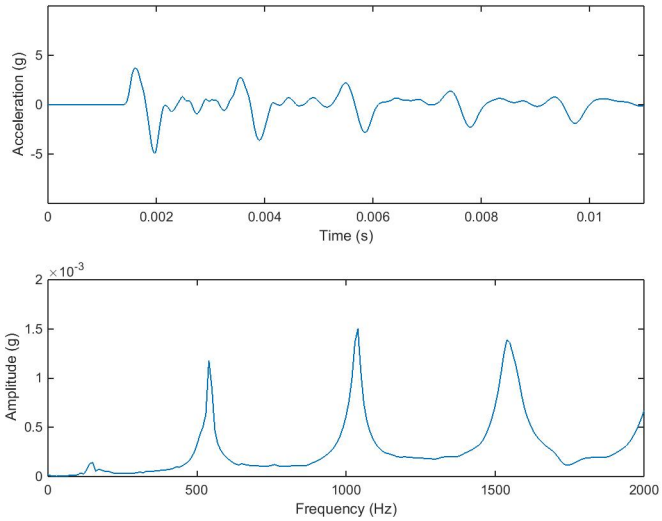

Total Pole Length	318.0 in (8.08 m)
Embedment Depth	75.0 in (1.91 m)
Base Circumference	36.75 in (93.35 cm)
Top Circumference	25.25 in (64.14 cm)
Marking	None
Inspection Tag	None

Length of Wave Speed Specimen	191.375 in (4.86 m)
Frequency of Wave Reflections	515 Hz
Longitudinal Wave Speed, C_p	197,116 in/s (5007 m/s)
In-Situ Density, ρ	37.99 lb/ft^3 (608.5 kg/m^3)
Moisture Content	11.3 %
Longitudinal Elastic Modulus, E_L	2212 ksi (15254 MPa)

Pole 20

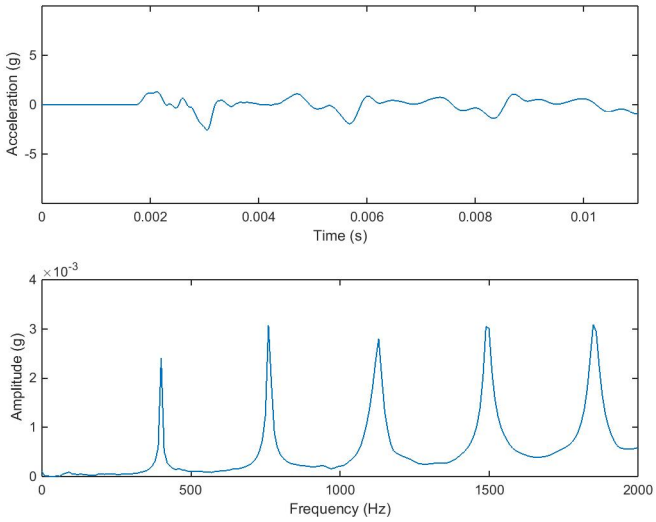

Total Pole Length	358.0 in (9.09 m)
Embedment Depth	75.0 in (1.91 m)
Base Circumference	31.25 in (79.38 cm)
Top Circumference	22.25 in (56.52 cm)
Marking	None
Inspection Tag	None

Length of Wave Speed Specimen	232.4 in (5.90 m)
Frequency of Wave Reflections	370 Hz
Longitudinal Wave Speed, C_p	171,958 in/s (4368 m/s)
In-Situ Density, ρ	35.02 lb/ft^3 (561.0 kg/m^3)
Moisture Content	10.3 %
Longitudinal Elastic Modulus, E_L	1552 ksi (10702 MPa)

APPENDIX B: DESTRUCTIVE CHARACTERIZATION OF POLES

Pole 11

13.125 in. Above Ground

10.125 in. Above Ground

7.125 Above Ground

4 in. Above Ground

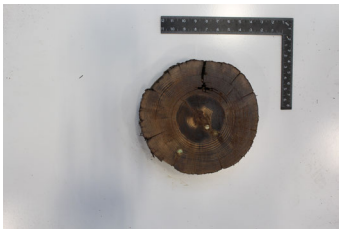

0.75 in. Above Ground

2.25 in. Below Ground

5.25 in. Below Ground

8.125 in. Below Ground

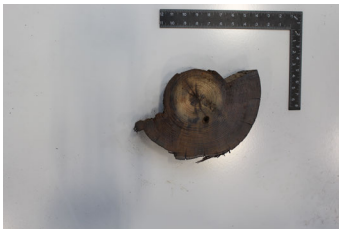

11.125 in. Below Ground

14.375 in. Below Ground

17.5 in. Below Ground

20.625 in. Below Ground

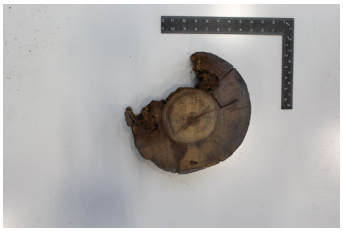

23.875 in. Below Ground

26.875 in. Below Ground

29.875 in. Below Ground

32.875 in. Below Ground

35.875 in. Below Ground

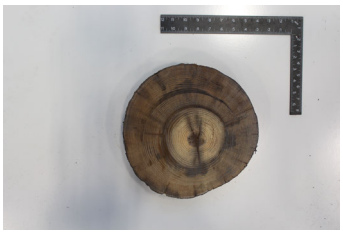

38.875 in. Below Ground

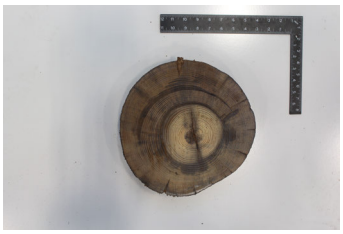

41.875 in. Below Ground

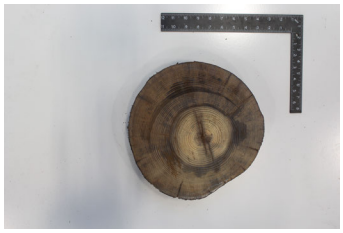

44.75 in. Below Ground

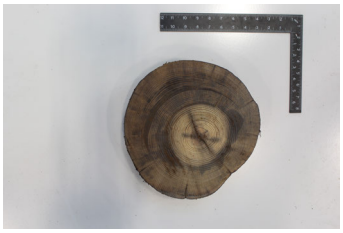

47.625 in. Below Ground

50.625 in. Below Ground

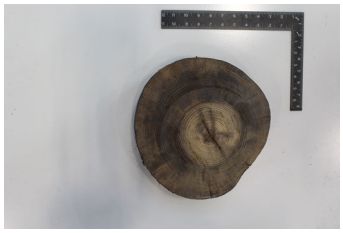

53.625 in. Below Ground

56.625 in. Below Ground

59.5 in. Below Ground 62.5 in. Below Ground 65.75 in. Below Ground

68.5 in. Below Ground 71.25 in. Below Ground

Pole 12

19.25 in. Above Ground | 16.25 in. Above Ground | 13.25 Above Ground

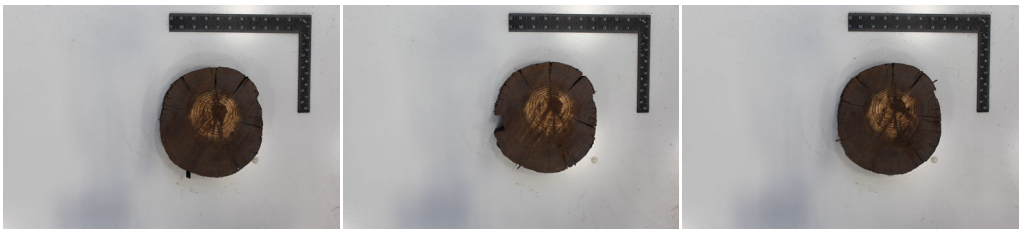

10.25 in. Above Ground | 7.5 in. Above Ground | 4.375 in. Above Ground

1.375 in. Below Ground | 1.625 in. Below Ground | 4.625 in. Below Ground

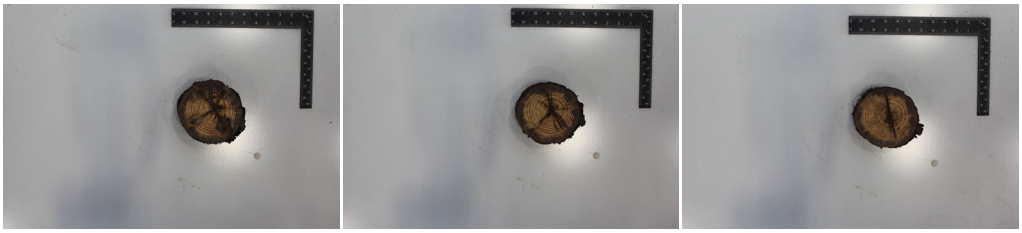

7.625 in. Below Ground | 10.625 in. Below Ground | 13.75 in. Below Ground

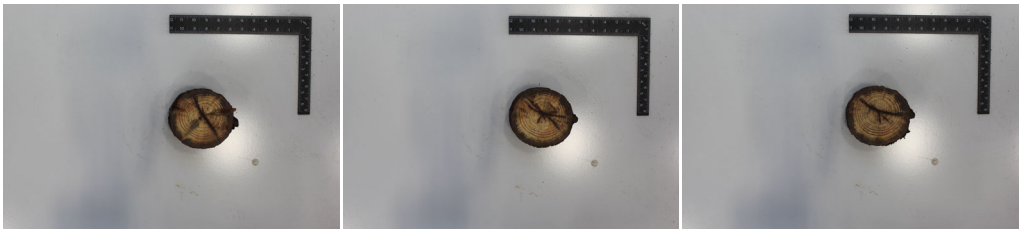

16.875 in. Below Ground

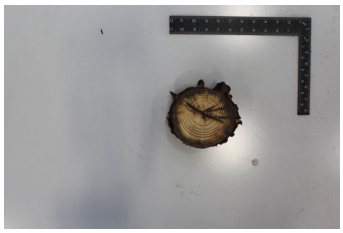

19.875 in. Below Ground

23 in. Below Ground

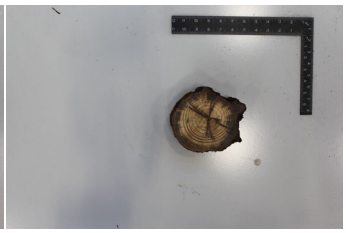

26 in. Below Ground

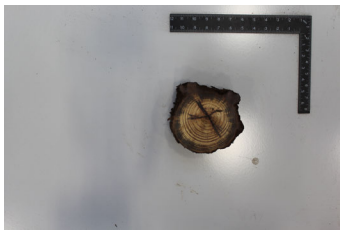

29 in. Below Ground

32.25 in. Below Ground

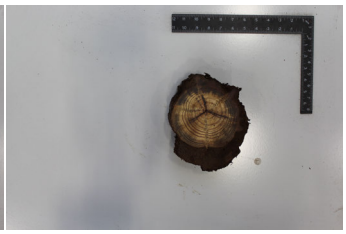

35.375 in. Below Ground

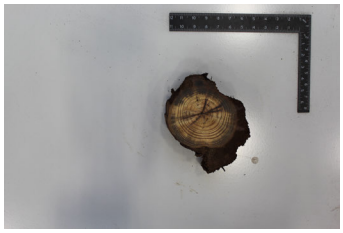

38.625 in. Below Ground

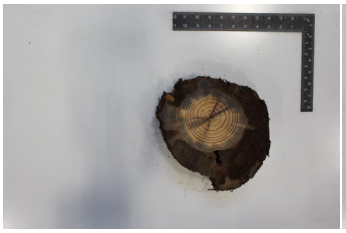

42.0 in. Below Ground

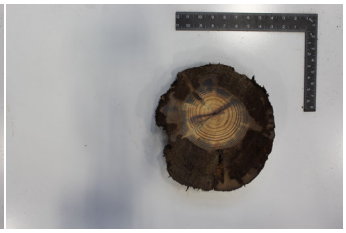

45.5 in. Below Ground

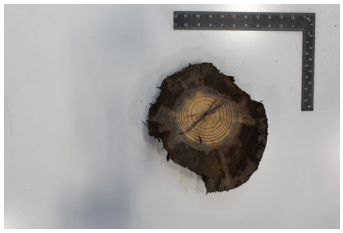

48.875 in. Below Ground

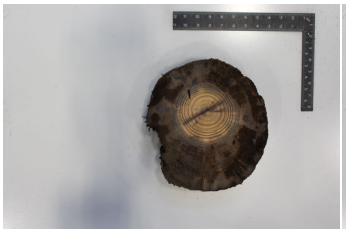

52.25 in. Below Ground

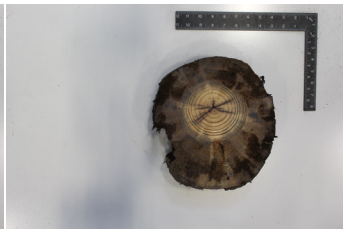

55.625 in. Below Ground

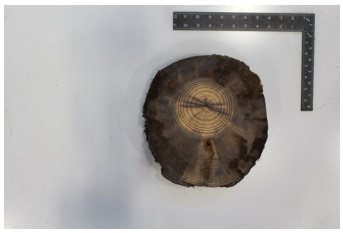

58.875 in. Below Ground

62.375 in. Below Ground

65.5 in. Below Ground

68.625 in. Below Ground

71.5 in. Below Ground

Pole 13

6.5 in. Above Ground	3.75 in. Above Ground	0.875 Above Ground
		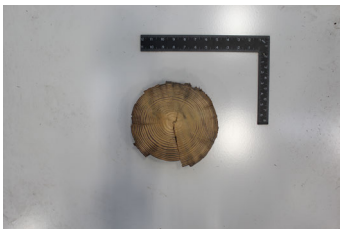

2.125 in. Below Ground	5.0 in. Below Ground	7.875 in. Below Ground
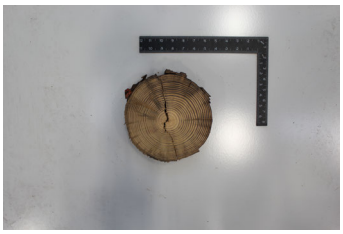	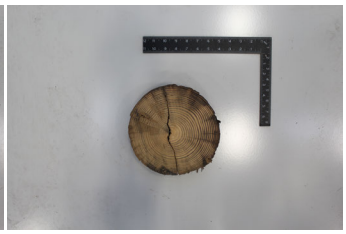	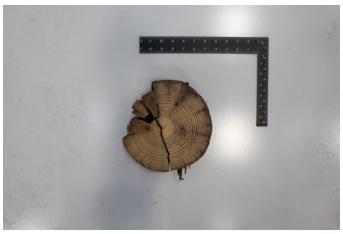

11.0 in. Below Ground	14.125 in. Below Ground	17.125 in. Below Ground
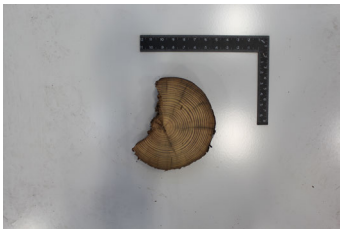		

20.25 in. Below Ground	23.25 in. Below Ground	26.375 in. Below Ground
	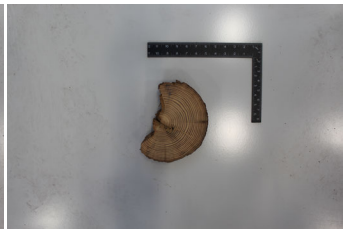	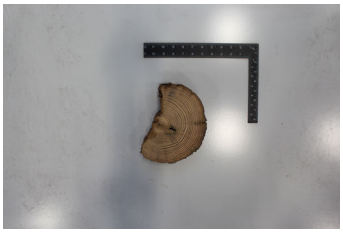

29.625 in. Below Ground

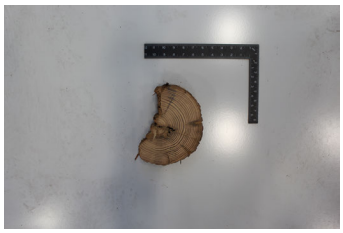

32.875 in. Below Ground

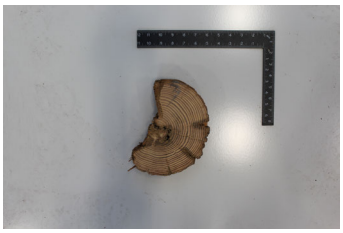

36.125 in. Below Ground

39.375 in. Below Ground

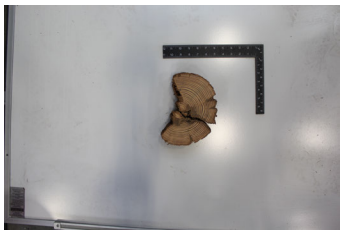

42.625 in. Below Ground

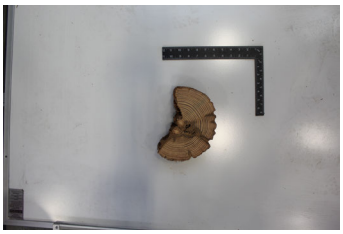

46.125 in. Below Ground

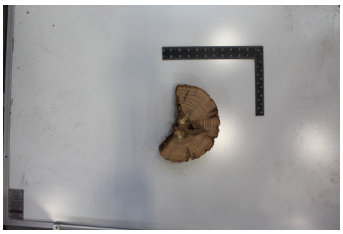

49.625 in. Below Ground

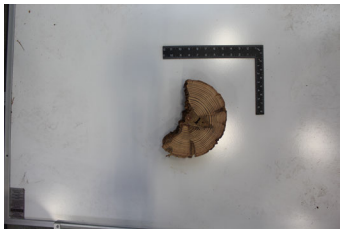

53.125 in. Below Ground

56.625 in. Below Ground

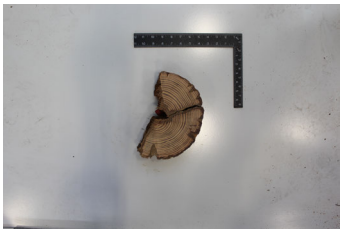

60 in. Below Ground

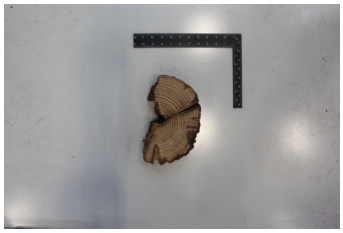

63.5 in. Below Ground

67.0 in. Below Ground

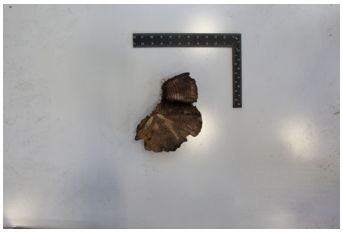

Pole 14

2.5 in. Above Ground

1.0 in. Below Ground

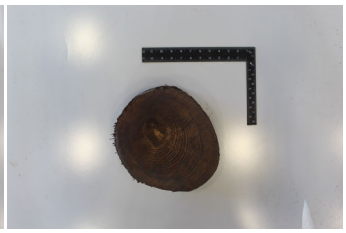

4.5 Below Ground

7.875 in. Below Ground

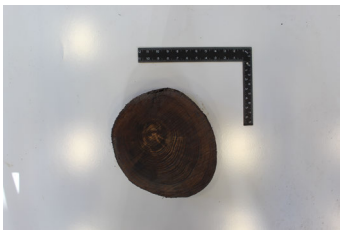

11.375 in. Below Ground

14.625 in. Below Ground

18.25 in. Below Ground

21.75 in. Below Ground

25.0 in. Below Ground

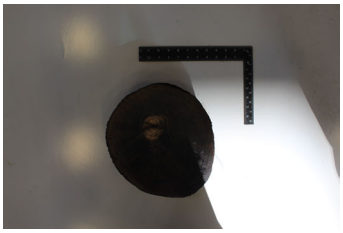

28.75 in. Below Ground

32.125 in. Below Ground

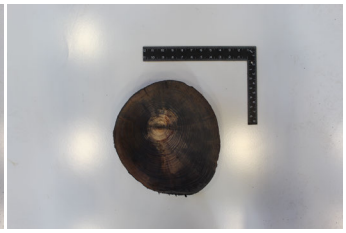

34.75 in. Below Ground

38.0 in. Below Ground

40.875 in. Below Ground

43.75 in. Below Ground

46.875 in. Below Ground

49.75 in. Below Ground

52.5 in. Below Ground

55.25 in. Below Ground

57.75 in. Below Ground

Pole 15

6.75 in. Above Ground | 4.25 in. Above Ground | 1.75 Above Ground

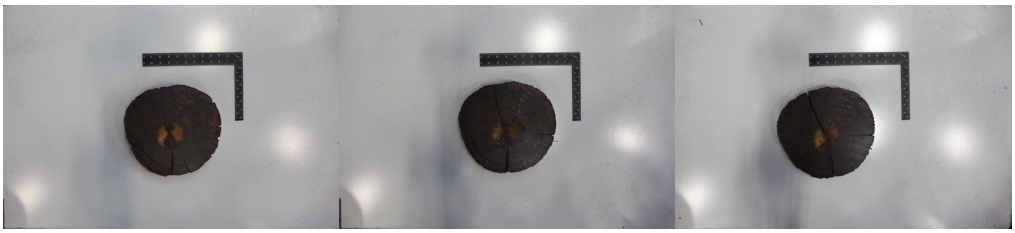

0.75 in. Below Ground | 3.25 in. Below Ground | 5.75 in. Below Ground

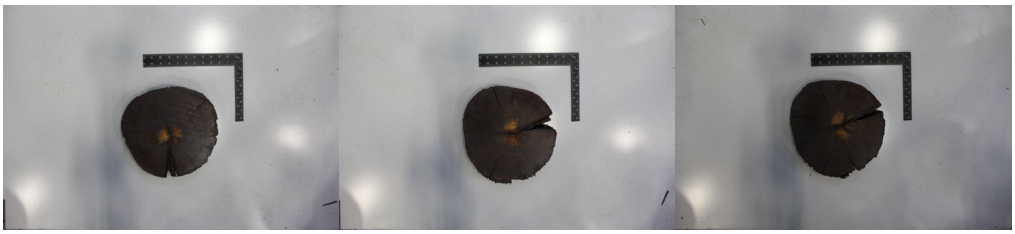

8.25 in. Below Ground | 11.0 in. Below Ground | 13.5 in. Below Ground

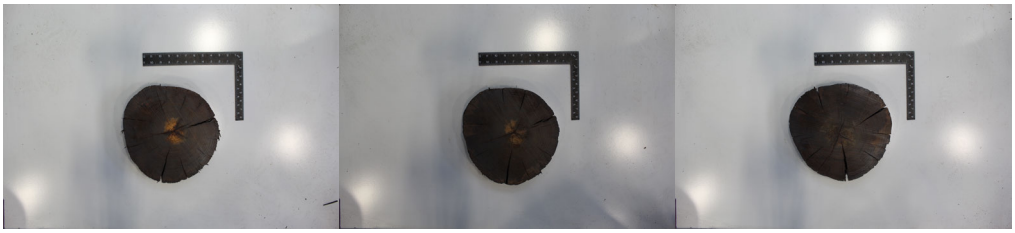

16.0 in. Below Ground | 18.5 in. Below Ground | 21.0 in. Below Ground

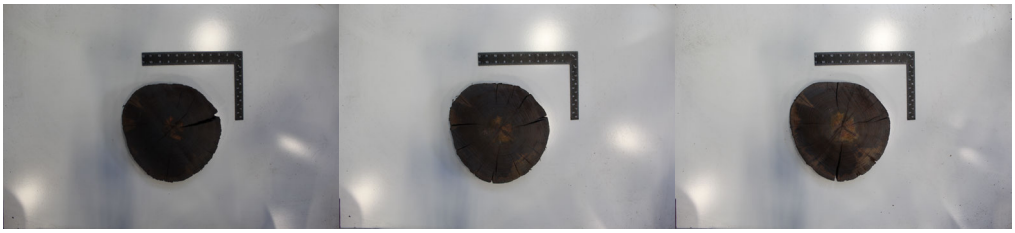

23.5 in. Below Ground 26.25 in. Below Ground 28.75 in. Below Ground

31.5 in. Below Ground 34.25 in. Below Ground 37.0 in. Below Ground

39.75 in. Below Ground 42.5 in. Below Ground 45 in. Below Ground

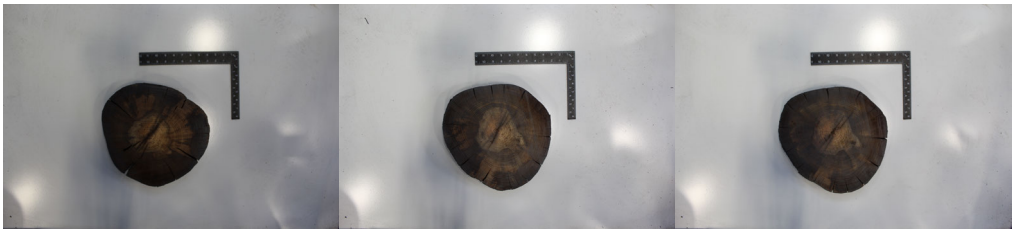

47.5 in. Below Ground 50.0 in. Below Ground 52.75 in. Below Ground

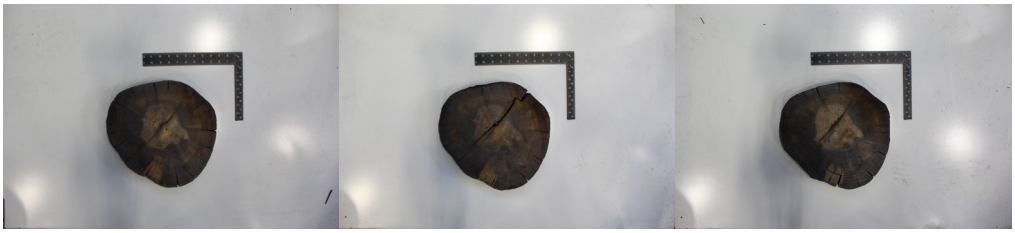

55.25 in. Below Ground 57.75 in. Below Ground

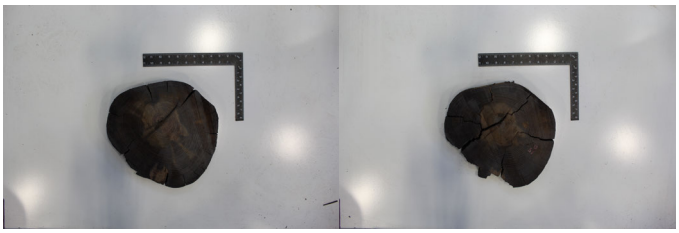

Pole 16

1.125 in. Above Ground 2.125 in. Below Ground 5.25 Below Ground

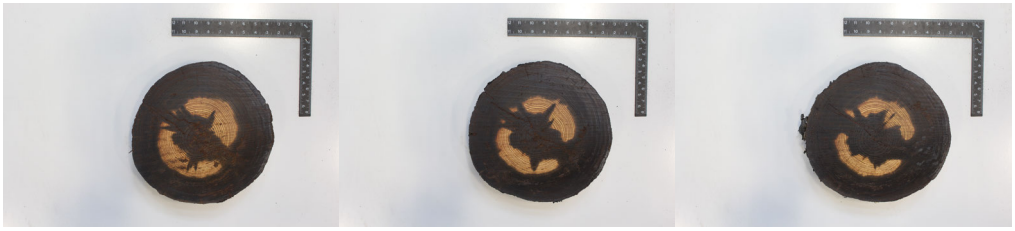

8.25 in. Below Ground 11.25 in. Below Ground 14.0 in. Below Ground

17.5 in. Below Ground 20.5 in. Below Ground 23.5 in. Below Ground

26.5 in. Below Ground 29.5 in. Below Ground 32.5 in. Below Ground

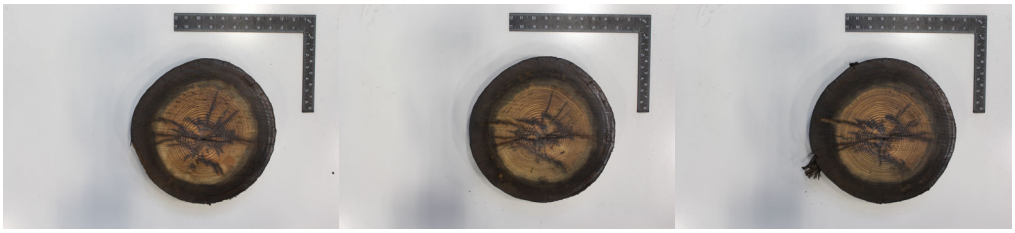

35.5 in. Below Ground 38.75 in. Below Ground 41.75 in. Below Ground

44.75 in. Below Ground 47.75 in. Below Ground 50.75 in. Below Ground

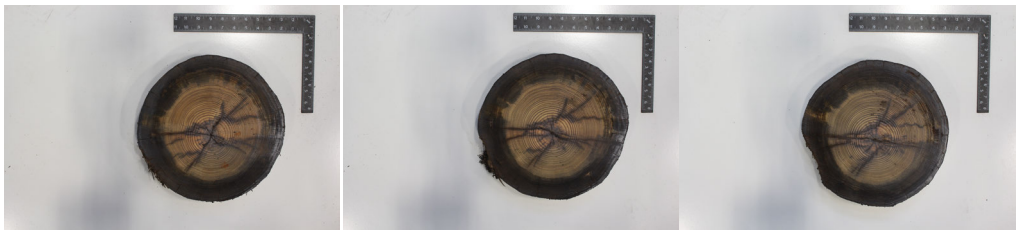

53.625 in. Below Ground 56.5 in. Below Ground 59.25 in. Below Ground

61.75 in. Below Ground 64.25 in. Below Ground 66.25 in. Below Ground

68.5 in. Below Ground

Pole 17

7.5 in. Above Ground	4.5 in. Above Ground	1.75 Above Ground
		

1 in. Below Ground	3.75 in. Below Ground	6.5 in. Below Ground
		

9.25 in. Below Ground	12.25 in. Below Ground	15.0 in. Below Ground
		

18.0 in. Below Ground	21.0 in. Below Ground	24.25 in. Below Ground
		

27.25 in. Below Ground 30.25 in. Below Ground 33.25 in. Below Ground

36.25 in. Below Ground 39.25 in. Below Ground 42.0 in. Below Ground

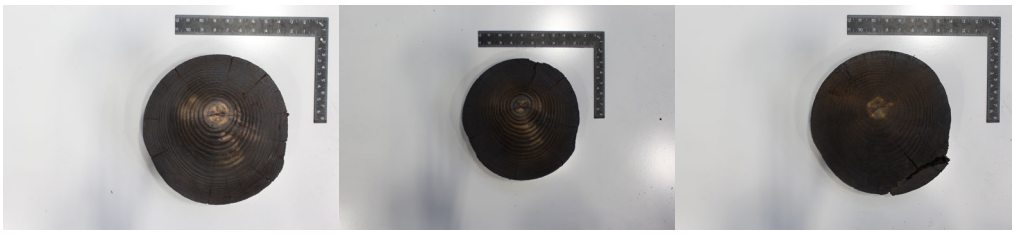

44.75 in. Below Ground 47.25 in. Below Ground 50.0 in. Below Ground

52.75 in. Below Ground 55.75 in. Below Ground 58.25 in. Below Ground

60.75 in. Below Ground 63.25 in. Below Ground 66.0 in. Below Ground

68.75 in. Below Ground 72.0 in. Below Ground

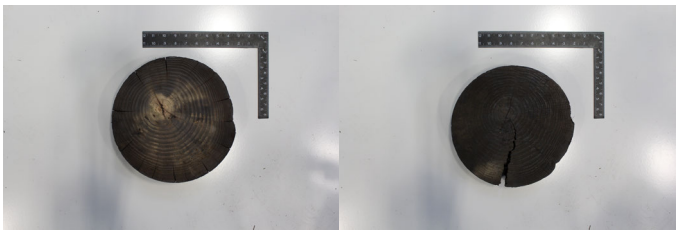

Pole 18

7.0 in. Above Ground	3.25 in. Above Ground	0.5 Above Ground
	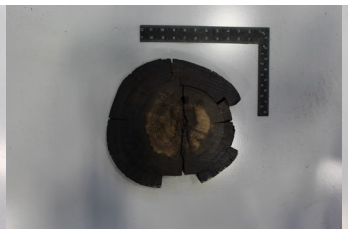	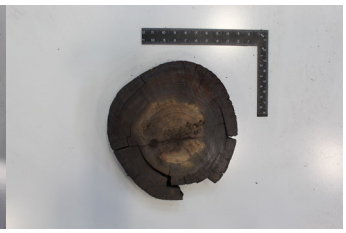

2.25 in. Below Ground	5.0 in. Below Ground	7.75 in. Below Ground
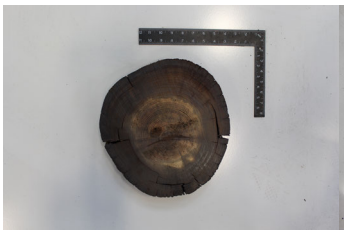	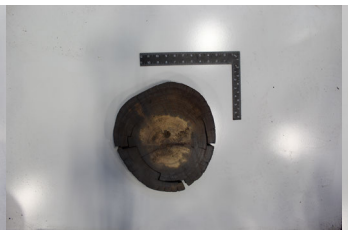	

10.5 in. Below Ground	13.5 in. Below Ground	16.5 in. Below Ground
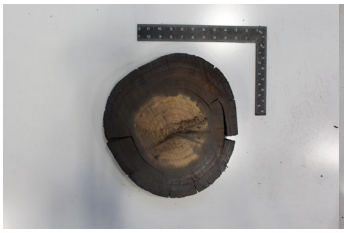	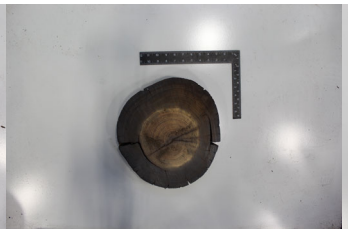	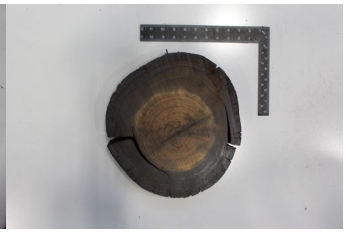

19.25 in. Below Ground	22.0 in. Below Ground	24.75 in. Below Ground
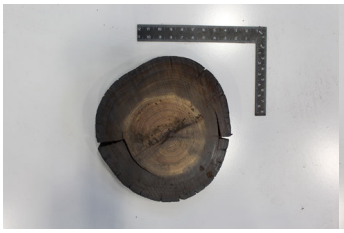		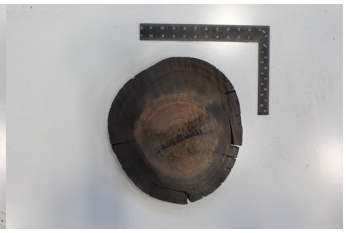

27.5 in. Below Ground 30.5 in. Below Ground 33.25 in. Below Ground

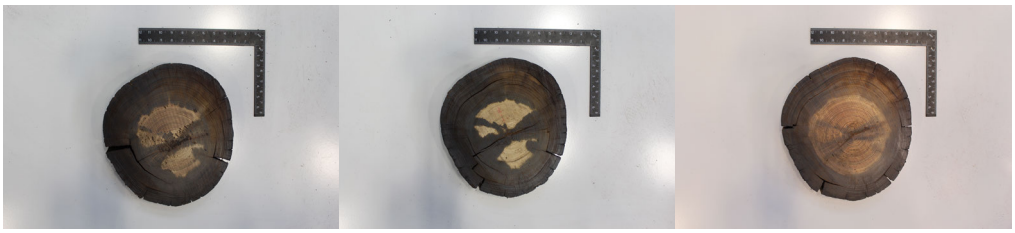

36.0 in. Below Ground 38.75 in. Below Ground 41.25 in. Below Ground

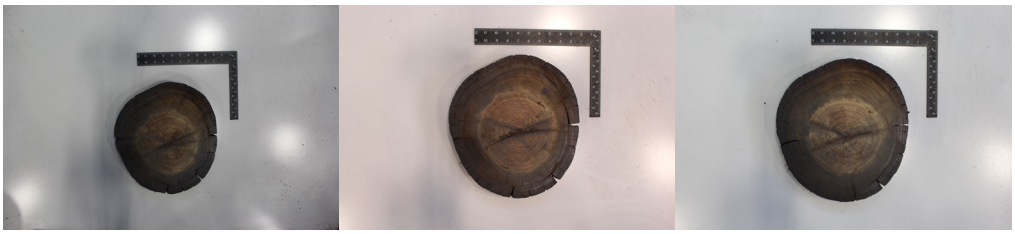

43.75 in. Below Ground 46.25 in. Below Ground 49.0 in. Below Ground

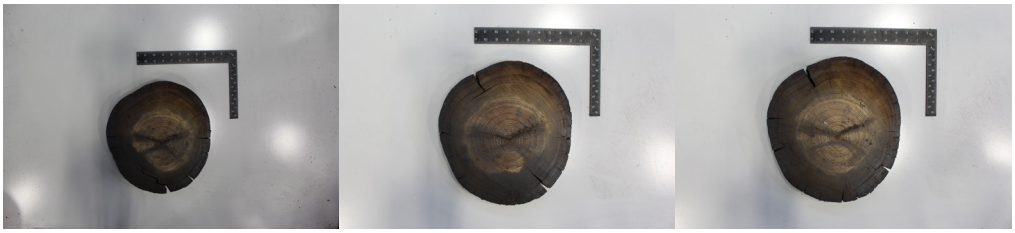

51.5 in. Below Ground 54.0 in. Below Ground 57.0 in. Below Ground

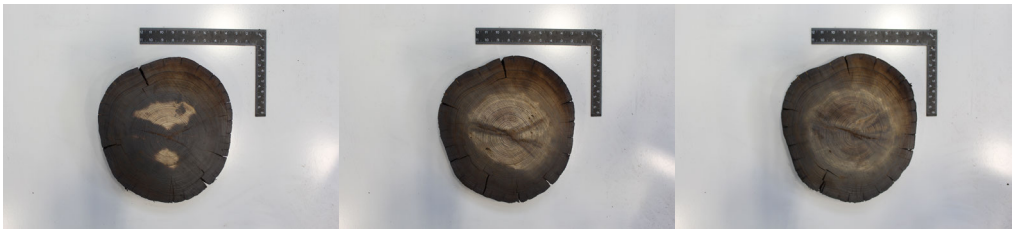

59.75 in. Below Ground 62.25 in. Below Ground 64.75 in. Below Ground

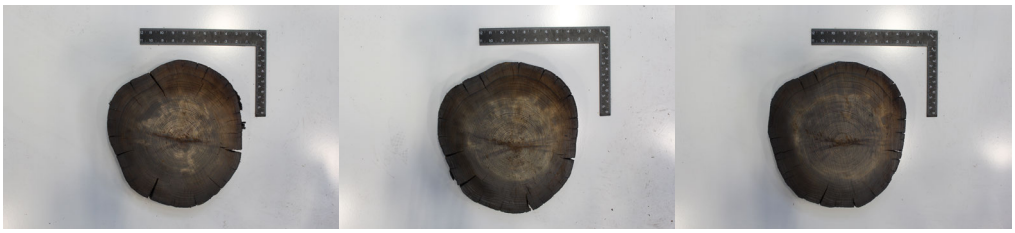

67.25 in. Below Ground 70.0 in. Below Ground 72.5 in. Below Ground

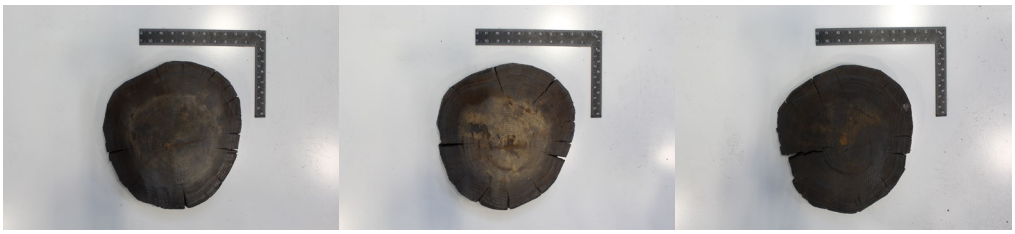

Pole 19

38.0 in. Above Ground 35.0 in. Above Ground 31.75 Above Ground

28.5 in. Above Ground 25.25 in. Above Ground 22.0 in. Above Ground

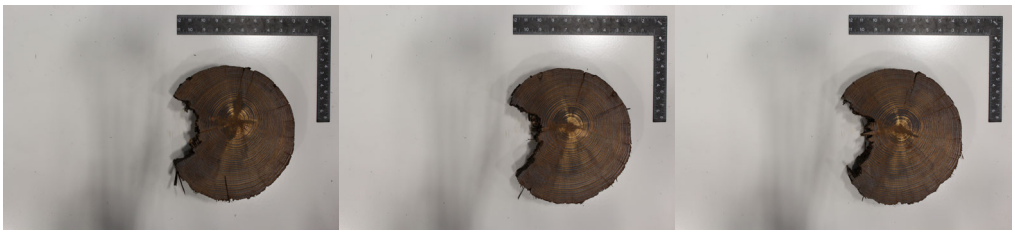

18.75 in. Above Ground 15.5 in. Above Ground 12.25 in. Above

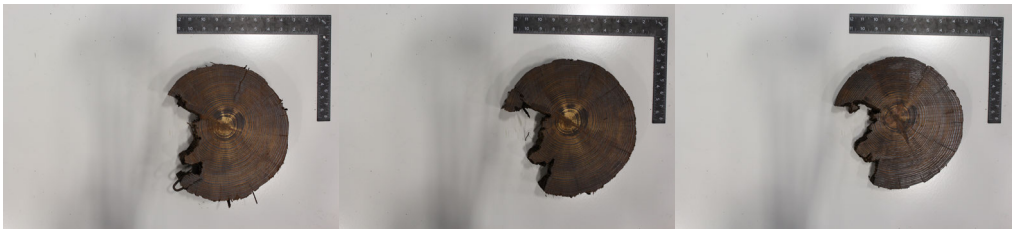

9.0 in. Above Ground 6.0 in. Above Ground 3.25 in. Above Ground

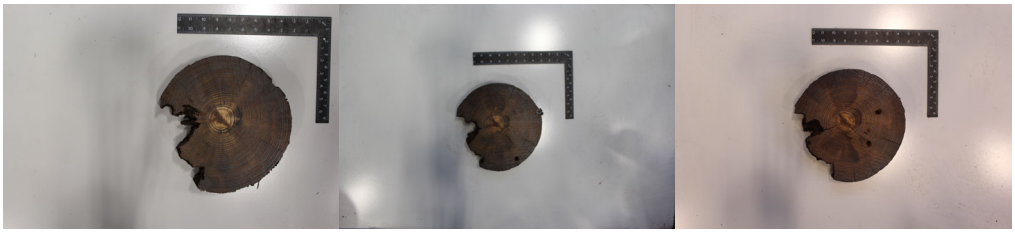

0.5 in. Above Ground | 2.25 in. Below Ground | 5.0 in. Below Ground

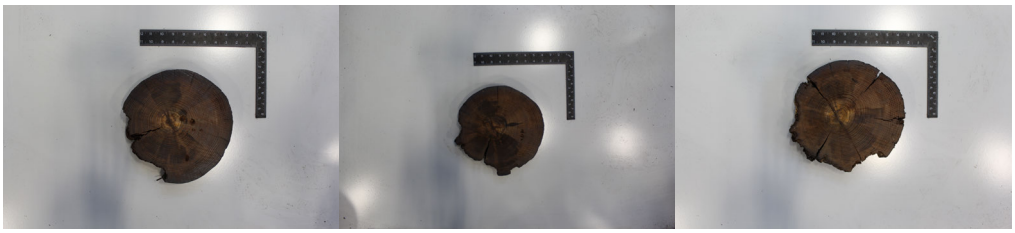

7.75 in. Below Ground | 10.5 in. Below Ground | 13.0 in. Below Ground

15.5 in. Below Ground | 18.25 in. Below Ground | 20.75 in. Below Ground

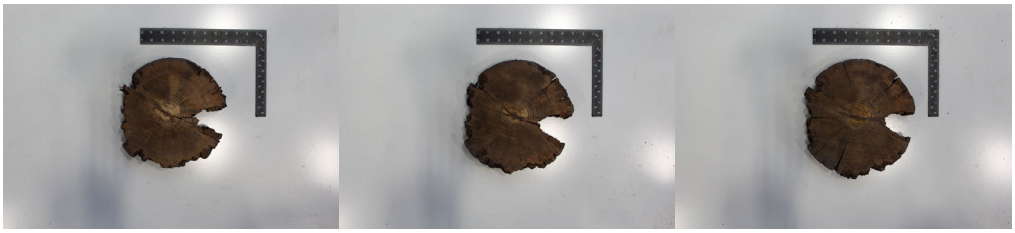

23.5 in. Below Ground | 26.0 in. Below Ground | 28.75 in. Below Ground

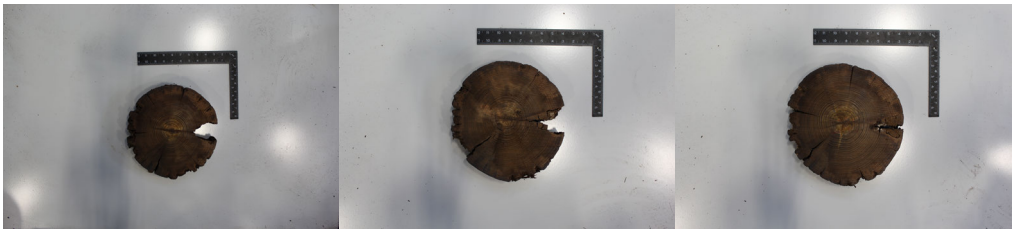

31.25 in. Below Ground 33.75 in. Below Ground 36.25 in. Below Ground

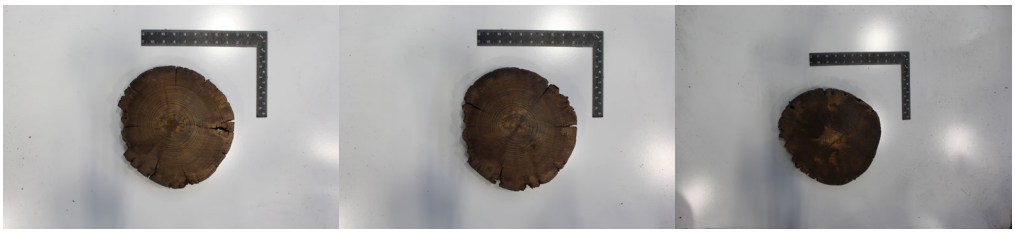

39.0 in. Below Ground 41.5 in. Below Ground 44 in. Below Ground

46.5 in. Below Ground 49.0 in. Below Ground 51.5 in. Below Ground

54.0 in. Below Ground 56.5 in. Below Ground 59.0 in. Below Ground

61.5 in. Below Ground 64.0 in. Below Ground 66.5 in. Below Ground

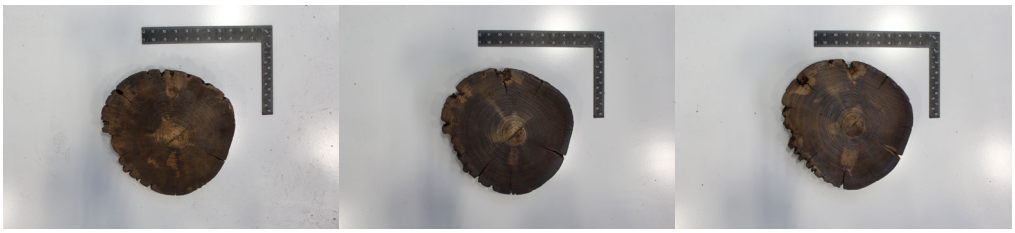

68.75 in. Below Ground 71.25 in. Below Ground

Pole 20

6.125 in. Above Ground | 9.0 in. Above Ground | 12.0 Below Ground

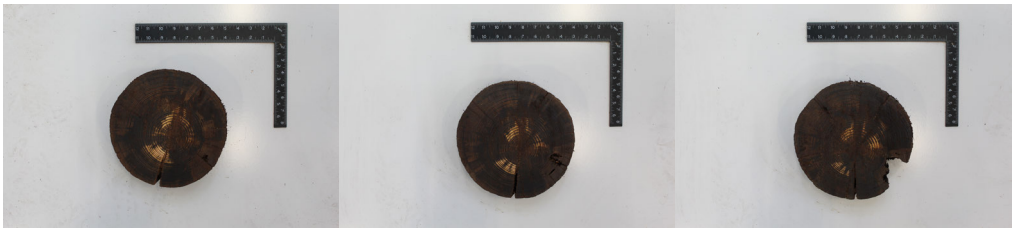

3.5 in. Above Ground | 0.5 in. Above Ground | 2.5 Below Ground

5.5 in. Below Ground | 8.25 in. Below Ground | 11.0 in. Below Ground

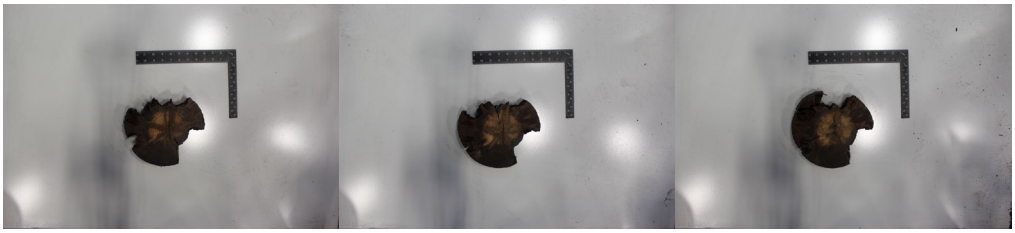

14.0 in. Below Ground | 16.75 in. Below Ground | 19.5 in. Below Ground

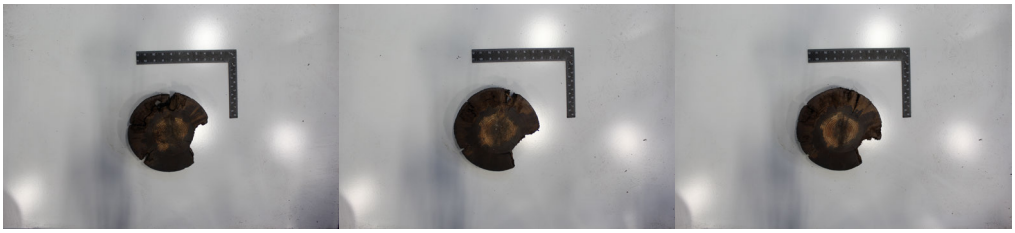

22.25 in. Below Ground 25.0 in. Below Ground 27.75 in. Below Ground

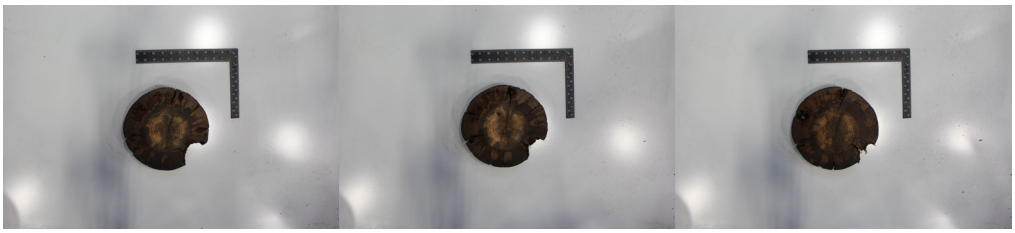

30.5 in. Below Ground 33.25 in. Below Ground 36.0 in. Below Ground

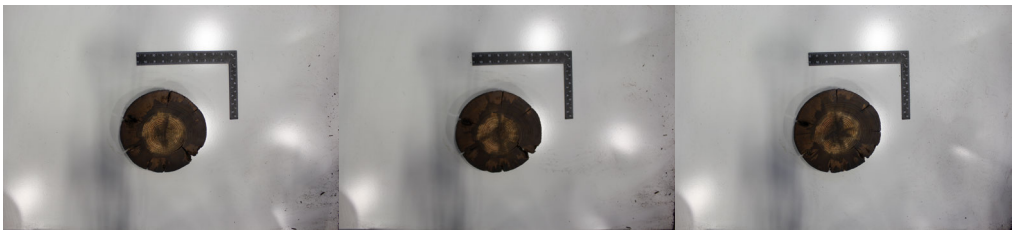

38.75 in. Below Ground 41.5 in. Below Ground 44.25 in. Below Ground

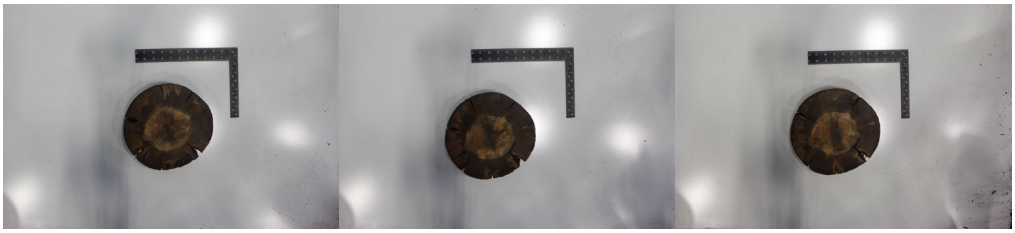

47.0 in. Below Ground 49.75 in. Below Ground 52.5 in. Below Ground

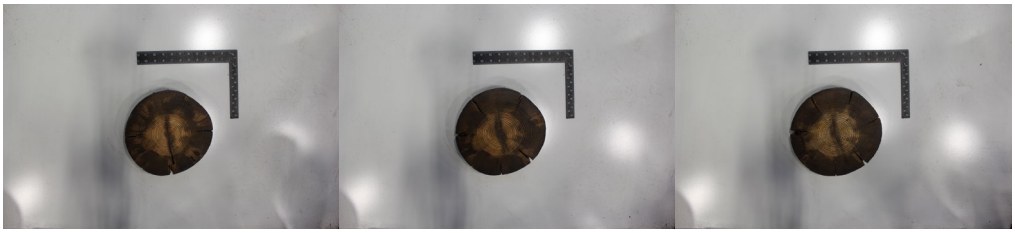

55.25 in. Below Ground 58.0 in. Below Ground 60.75 in. Below Ground

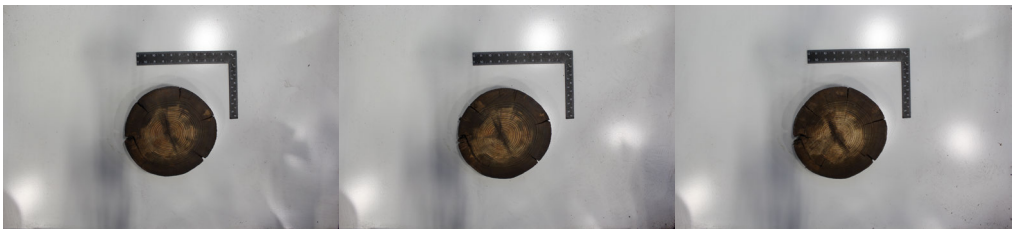

63.5 in. Below Ground 66.25 in. Below Ground 69.25 in. Below Ground

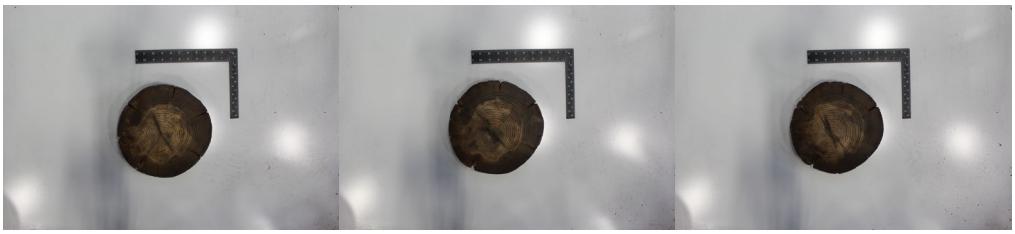

72 in. Below Ground

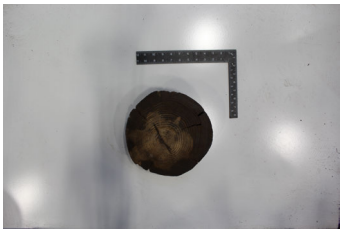

APPENDIX C: IMAGE ANALYSIS OF POLE SLICES

Pole 11

Depth	**A** (in^2)	$d_{eff}(in)$	$C_{eff}(in)$	$I_x(in^4)$	$I_y(in^4)$
13.125 in (A.G.)	80.81	10.14	31.87	523.1	518.9
10.125 in (A.G.)	82.92	10.28	32.28	560.3	539.0
7.125 in (A.G.)	84.08	10.35	32.51	589.0	539.7
4 in (A.G.)	85.89	10.46	32.85	616.0	561.4
0.75 in (A.G.)	85.03	10.41	32.69	585.3	567.6
2.25 in (B.G.)	87.33	10.54	33.13	634.7	583.0
5.25 in (B.G.)	54.18	8.31	26.09	311.0	201.3
8.125 in (B.G.)	54.36	8.32	26.14	314.7	199.5
11.125 in (B.G.)	57.62	8.57	26.91	369.4	218.9
14.375 in (B.G.)	60.64	8.79	27.60	422.3	231.9
17.5 in (B.G.)	66.23	9.18	28.85	431.8	367.9
20.625 in (B.G.)	76.29	9.86	30.96	553.2	492.7
23.875 in (B.G.)	78.66	10.01	31.44	624.8	481.6
26.875 in (B.G.)	96.70	11.10	34.86	768.6	722.2
29.875 in (B.G.)	96.99	11.11	34.91	763.2	737.0
32.875 in (B.G.)	97.37	11.13	34.98	763.3	748.6
35.875 in (B.G.)	98.54	11.20	35.19	786.4	762.1
38.875 in (B.G.)	99.49	11.26	35.36	790.2	789.5
41.875 in (B.G.)	99.96	11.28	35.44	792.4	802.6
44.75 in (B.G.)	101.24	11.35	35.67	798.2	839.3
47.625 in (B.G.)	101.72	11.38	35.75	794.7	858.8
50.625 in (B.G.)	102.36	11.42	35.86	798.7	876.5
53.625 in (B.G.)	104.02	11.51	36.15	821.7	909.2
56.625 in (B.G.)	103.91	11.50	36.14	811.5	915.8
59.5 in (B.G.)	106.66	11.65	36.61	845.0	976.5
62.5 in (B.G.)	108.22	11.74	36.88	864.6	1013.5
65.75 in (B.G.)	104.33	11.53	36.21	788.8	960.9
68.5 in (B.G.)	105.45	11.59	36.40	794.7	997.6
71.25 in (B.G.)	109.40	11.80	37.08	1047.0	887.9

Pole 12

Depth	**A** (in^2)	$d_{eff}(in)$	$C_{eff}(in)$	$I_x(in^4)$	$I_y(in^4)$
19.25 in (A.G.)	64.63	9.07	28.50	310.2	358.1
16.25 in (A.G.)	64.48	9.06	28.46	306.7	360.0
13.25 in (A.G.)	66.02	9.17	28.80	324.3	372.5
10.25 in (A.G.)	49.60	7.95	24.97	232.6	169.6
7.5 in (A.G.)	50.79	8.04	25.26	246.6	176.0
4.375 in (A.G.)	52.12	8.15	25.59	254.3	188.7
1.375 in (A.G.)	23.89	5.51	17.33	48.5	43.2
1.625 in (B.G.)	23.04	5.42	17.02	47.1	38.2
4.625 in (B.G.)	22.83	5.39	16.94	46.3	38.0
7.625 in (B.G.)	22.17	5.31	16.69	44.3	34.8
10.625 in (B.G.)	21.84	5.27	16.57	41.9	34.5
13.75 in (B.G.)	21.91	5.28	16.59	42.5	34.5
16.875 in (B.G.)	25.55	5.70	17.92	58.2	47.9
19.875 in (B.G.)	27.45	5.91	18.57	66.4	55.5
23 in (B.G.)	26.14	5.77	18.12	62.8	48.3
26 in (B.G.)	28.73	6.05	19.00	69.7	64.1
29 in (B.G.)	29.37	6.12	19.21	71.0	67.9
32.25 in (B.G.)	40.97	7.22	22.69	109.9	165.7
35.375 in (B.G.)	38.08	6.96	21.88	110.3	135.9
38.625 in (B.G.)	67.14	9.25	29.05	379.2	359.4
42 in (B.G.)	83.37	10.30	32.37	506.9	611.7
45.5 in (B.G.)	75.19	9.78	30.74	449.7	488.1
48.875 in (B.G.)	87.89	10.58	33.23	551.0	697.2
52.25 in (B.G.)	90.78	10.75	33.77	586.9	748.4
55.625 in (B.G.)	95.81	11.04	34.70	675.3	795.1
58.875 in (B.G.)	100.74	11.33	35.58	737.3	888.5
62.375 in (B.G.)	102.40	11.42	35.87	767.0	914.1
65.5 in (B.G.)	105.69	11.60	36.44	817.3	969.9
68.625 in (B.G.)	107.59	11.70	36.77	855.3	995.7
71.5 in (B.G.)	114.41	12.07	37.92	966.1	1126.1

Pole 13

Depth	**A** (in^2)	$d_{eff}(in)$	$C_{eff}(in)$	$I_x(in^4)$	$I_y(in^4)$
6.5 in (A.G.)	47.09	7.74	24.32	183.7	170.8
3.75 in (A.G.)	46.48	7.69	24.17	183.9	163.4
0.875 in (A.G.)	48.85	7.89	24.78	203.5	179.6
2.125 in (B.G.)	53.46	8.25	25.92	225.7	231.1
5 in (B.G.)	55.88	8.43	26.50	252.3	245.6
7.875 in (B.G.)	53.02	8.22	25.81	209.4	246.1
11 in (B.G.)	44.66	7.54	23.69	131.7	221.0
14.125 in (B.G.)	44.06	7.49	23.53	133.9	213.0
17.125 in (B.G.)	43.83	7.47	23.47	122.7	215.4
20.25 in (B.G.)	42.89	7.39	23.22	115.4	216.0
23.25 in (B.G.)	41.40	7.26	22.81	109.9	196.1
26.375 in (B.G.)	40.00	7.14	22.42	101.2	185.0
29.625 in (B.G.)	39.63	7.10	22.32	98.3	189.5
32.875 in (B.G.)	38.52	7.00	22.00	92.1	185.3
36.125 in (B.G.)	37.88	6.95	21.82	91.2	176.7
39.375 in (B.G.)	40.40	7.17	22.53	93.7	211.8
42.625 in (B.G.)	41.78	7.29	22.91	105.8	222.7
46.125 in (B.G.)	44.48	7.53	23.64	118.7	253.1
49.625 in (B.G.)	44.95	7.57	23.77	132.3	253.0
53.125 in (B.G.)	47.63	7.79	24.46	132.3	298.6
56.625 in (B.G.)	46.10	7.66	24.07	123.9	282.1
60 in (B.G.)	45.70	7.63	23.96	108.5	291.7
63.5 in (B.G.)	45.12	7.58	23.81	109.5	262.0
67 in (B.G.)	39.91	7.13	22.39	115.2	190.6

Pole 14

Depth	**A** (in^2)	$d_{eff}(in)$	$C_{eff}(in)$	$I_x(in^4)$	$I_y(in^4)$
2.50 in (A.G.)	92.92	10.88	34.17	713.9	677.6
1.00 in (B.G.)	95.15	11.01	34.58	723.2	735.1
4.50 in (B.G.)	96.66	11.09	34.85	735.8	767.7
7.88 in (B.G.)	98.47	11.20	35.18	750.8	809.3
11.38 in (B.G.)	98.64	11.21	35.21	774.0	790.4
14.63 in (B.G.)	101.02	11.34	35.63	753.2	893.0
18.25 in (B.G.)	103.05	11.45	35.99	805.7	904.4
21.75 in (B.G.)	102.63	11.43	35.91	783.9	911.8
25.00 in (B.G.)	106.59	11.65	36.60	867.7	955.7
28.75 in (B.G.)	107.43	11.70	36.74	867.6	985.0
32.13 in (B.G.)	106.50	11.64	36.58	841.9	978.9
34.75 in (B.G.)	110.29	11.85	37.23	910.0	1041.7
38.00 in (B.G.)	111.07	11.89	37.36	906.3	1072.4
40.88 in (B.G.)	113.12	12.00	37.70	927.6	1125.4
43.75 in (B.G.)	116.85	12.20	38.32	992.8	1196.9
46.88 in (B.G.)	118.51	12.28	38.59	1029.9	1222.5
49.75 in (B.G.)	118.68	12.29	38.62	1041.2	1218.3
52.50 in (B.G.)	120.69	12.40	38.94	1086.2	1250.6
55.25 in (B.G.)	118.09	12.26	38.52	1033.8	1207.4
57.75 in (B.G.)	120.37	12.38	38.89	1080.0	1245.4

Pole 15

Depth	**A** (in^2)	$d_{eff}(in)$	$C_{eff}(in)$	$I_x(in^4)$	$I_y(in^4)$
6.75 in (A.G.)	100.63	11.32	35.56	860.3	758.2
4.25 in (A.G.)	100.93	11.34	35.61	866.8	761.3
1.75 in (A.G.)	101.53	11.37	35.72	880.2	768.3
0.75 in (B.G.)	102.25	11.41	35.85	890.9	782.9
3.25 in (B.G.)	102.97	11.45	35.97	808.3	892.1
5.75 in (B.G.)	105.25	11.58	36.37	859.0	913.7
8.25 in (B.G.)	104.00	11.51	36.15	850.1	879.5
11.00 in (B.G.)	102.38	11.42	35.87	824.7	852.0
13.50 in (B.G.)	109.27	11.80	37.06	1004.5	907.0
16.00 in (B.G.)	107.51	11.70	36.76	916.3	934.5
18.50 in (B.G.)	111.86	11.93	37.49	985.6	1018.8
21.00 in (B.G.)	110.84	11.88	37.32	984.5	983.4
23.50 in (B.G.)	114.93	12.10	38.00	1072.7	1047.1
26.25 in (B.G.)	113.36	12.01	37.74	1041.7	1022.4
28.75 in (B.G.)	116.06	12.16	38.19	1090.3	1071.8
31.50 in (B.G.)	118.20	12.27	38.54	1132.5	1107.5
34.25 in (B.G.)	120.60	12.39	38.93	1166.4	1167.6
37.00 in (B.G.)	121.05	12.41	39.00	1202.5	1151.6
39.75 in (B.G.)	123.00	12.51	39.32	1273.2	1157.6
42.50 in (B.G.)	127.95	12.76	40.10	1350.6	1278.5
45.00 in (B.G.)	129.16	12.82	40.29	1378.4	1302.5
47.50 in (B.G.)	129.02	12.82	40.27	1396.6	1282.3
50.00 in (B.G.)	134.33	13.08	41.09	1515.6	1389.4
52.75 in (B.G.)	130.79	12.90	40.54	1462.1	1291.3
55.25 in (B.G.)	128.92	12.81	40.25	1412.2	1271.0
57.75 in (B.G.)	122.42	12.48	39.22	1333.5	1123.7

Pole 16

Depth	**A** (in^2)	$d_{eff}(in)$	$C_{eff}(in)$	$I_x(in^4)$	$I_y(in^4)$
1.125 in (A.G.)	113.22	12.01	37.72	1018.0	1026.0
2.125 in (B.G.)	114.00	12.05	37.85	1052.3	1018.6
5.25 in (B.G.)	114.56	12.08	37.94	1087.9	1004.8
8.25 in (B.G.)	116.78	12.19	38.31	1119.7	1053.4
11.25 in (B.G.)	115.31	12.12	38.07	1077.2	1042.4
14 in (B.G.)	116.98	12.20	38.34	1124.4	1057.4
17.50 in (B.G.)	116.51	12.18	38.26	1093.5	1068.9
20.50 in (B.G.)	115.36	12.12	38.07	1084.9	1035.4
23.50 in (B.G.)	114.70	12.08	37.97	1050.6	1044.8
26.50 in (B.G.)	113.47	12.02	37.76	1022.7	1028.0
29.50 in (B.G.)	116.28	12.17	38.23	1081.0	1072.4
32.50 in (B.G.)	116.28	12.17	38.23	1084.4	1069.0
35.50 in (B.G.)	115.12	12.11	38.04	1081.3	1031.0
38.75 in (B.G.)	114.73	12.09	37.97	1066.6	1031.0
41.75 in (B.G.)	114.76	12.09	37.97	1068.3	1029.2
44.75 in (B.G.)	117.90	12.25	38.49	1117.8	1095.9
47.75 in (B.G.)	118.40	12.28	38.57	1141.5	1091.9
50.75 in (B.G.)	116.44	12.18	38.25	1065.5	1096.0
53.63 in (B.G.)	115.59	12.13	38.11	1055.6	1075.6
56.50 in (B.G.)	116.48	12.18	38.26	1071.9	1090.0
59.25 in (B.G.)	113.65	12.03	37.79	991.9	1069.4
61.75 in (B.G.)	112.13	11.95	37.54	944.4	1068.5
64.25 in (B.G.)	110.53	11.86	37.27	932.5	1022.5
66.25 in (B.G.)	110.95	11.89	37.34	923.8	1050.8
68.50 in (B.G.)	118.61	12.29	38.61	1058.8	1202.8

Pole 17

Depth	**A** (in^2)	$d_{eff}(in)$	$C_{eff}(in)$	$I_x(in^4)$	$I_y(in^4)$
7.5 in (A.G.)	97.64	11.15	35.03	767.2	751.1
4.5 in (A.G.)	97.00	11.11	34.91	748.0	750.9
1.75 in (A.G.)	93.79	10.93	34.33	693.1	707.6
1 in (B.G.)	94.65	10.98	34.49	702.5	724.3
3.75 in (B.G.)	94.46	10.97	34.45	691.0	730.1
6.5 in (B.G.)	95.78	11.04	34.69	709.1	752.5
9.25 in (B.G.)	91.00	10.76	33.82	649.5	674.5
12.25 in (B.G.)	99.10	11.23	35.29	758.5	808.3
15.00 in (B.G.)	100.61	11.32	35.56	780.1	833.2
18.00 in (B.G.)	100.16	11.29	35.48	778.1	820.0
21.00 in (B.G.)	101.64	11.38	35.74	798.4	847.1
24.25 in (B.G.)	101.58	11.37	35.73	797.4	846.3
27.25 in (B.G.)	102.93	11.45	35.96	808.9	879.6
30.25 in (B.G.)	104.27	11.52	36.20	831.6	901.1
33.25 in (B.G.)	104.93	11.56	36.31	840.9	914.1
36.25 in (B.G.)	105.71	11.60	36.45	860.3	920.8
39.25 in (B.G.)	98.92	11.22	35.26	746.3	814.4
42.00 in (B.G.)	97.37	11.13	34.98	734.8	778.6
44.75 in (B.G.)	101.79	11.38	35.76	798.4	853.5
47.25 in (B.G.)	103.76	11.49	36.11	824.0	893.1
50.00 in (B.G.)	102.63	11.43	35.91	802.7	878.4
52.75 in (B.G.)	100.96	11.34	35.62	775.7	851.2
55.75 in (B.G.)	103.86	11.50	36.13	819.1	902.5
58.25 in (B.G.)	104.64	11.54	36.26	828.6	919.1
60.75 in (B.G.)	105.44	11.59	36.40	842.4	931.7
63.25 in (B.G.)	106.59	11.65	36.60	867.1	945.4
66.00 in (B.G.)	106.79	11.66	36.63	878.3	939.5
68.75 in (B.G.)	109.44	11.80	37.08	932.0	975.8
72.00 in (B.G.)	103.70	11.49	36.10	864.1	849.9

Pole 18

Depth	**A** (in^2)	$d_{eff}(in)$	$C_{eff}(in)$	$I_x(in^4)$	$I_y(in^4)$
7 in (A.G.)	122.00	12.46	39.15	1106.9	1275.2
3.25 in (A.G.)	113.58	12.03	37.78	1102.0	995.0
0.5 in (A.G.)	121.51	12.44	39.08	1135.7	1236.3
2.25 in (B.G.)	123.69	12.55	39.43	1144.6	1303.2
5 in (B.G.)	121.80	12.45	39.12	1109.6	1266.6
7.75 in (B.G.)	124.64	12.60	39.58	1145.9	1342.1
10.50 in (B.G.)	127.25	12.73	39.99	1202.4	1391.6
13.50 in (B.G.)	125.80	12.66	39.76	1187.9	1344.2
16.50 in (B.G.)	130.69	12.90	40.52	1273.8	1457.8
19.25 in (B.G.)	130.47	12.89	40.49	1262.9	1460.7
22.00 in (B.G.)	119.72	12.35	38.79	1114.4	1186.1
24.75 in (B.G.)	129.22	12.83	40.30	1220.5	1454.4
27.50 in (B.G.)	129.90	12.86	40.40	1229.7	1474.8
30.50 in (B.G.)	123.25	12.53	39.35	1103.8	1331.2
33.25 in (B.G.)	130.88	12.91	40.55	1247.1	1498.0
36.00 in (B.G.)	127.39	12.74	40.01	1196.3	1401.3
38.75 in (B.G.)	130.75	12.90	40.54	1246.4	1492.9
41.25 in (B.G.)	132.21	12.97	40.76	1292.1	1504.3
43.75 in (B.G.)	127.88	12.76	40.09	1220.0	1395.1
46.25 in (B.G.)	135.36	13.13	41.24	1356.6	1574.9
49.00 in (B.G.)	136.62	13.19	41.43	1374.2	1612.8
51.50 in (B.G.)	137.84	13.25	41.62	1410.0	1629.2
54.00 in (B.G.)	140.00	13.35	41.94	1468.9	1666.0
57.00 in (B.G.)	144.73	13.58	42.65	1546.7	1809.7
59.75 in (B.G.)	139.91	13.35	41.93	1453.8	1683.7
62.25 in (B.G.)	139.48	13.33	41.87	1454.1	1663.0
64.75 in (B.G.)	144.28	13.55	42.58	1567.4	1767.9
67.25 in (B.G.)	143.35	13.51	42.44	1534.3	1760.5
70.00 in (B.G.)	141.09	13.40	42.11	1506.5	1688.7
72.50 in (B.G.)	130.31	12.88	40.47	1236.2	1496.2

Pole 19

Depth	**A** (in^2)	$d_{eff}(in)$	$C_{eff}(in)$	$I_x(in^4)$	$I_y(in^4)$
38 in (A.G.)	81.39	10.18	31.98	520.9	534.9
35 in (A.G.)	82.30	10.24	32.16	528.0	551.0
31.75 in (A.G.)	80.45	10.12	31.80	507.4	563.6
28.5 in (A.G.)	74.16	9.72	30.53	378.5	560.8
25.25 in (A.G.)	72.21	9.59	30.12	352.4	559.3
22 in (A.G.)	74.12	9.71	30.52	366.9	571.1
18.75 in (A.G.)	73.61	9.68	30.41	354.6	582.6
15.50 in (A.G.)	73.98	9.71	30.49	390.3	547.5
12.25 in (A.G.)	69.58	9.41	29.57	351.7	472.3
9.00 in (A.G.)	76.12	9.84	30.93	416.3	545.2
6.00 in (A.G.)	77.08	9.91	31.12	437.3	536.5
3.25 in (A.G.)	79.35	10.05	31.58	472.7	561.0
0.50 in (A.G.)	83.34	10.30	32.36	534.2	582.0
2.25 in (B.G.)	81.61	10.19	32.02	545.3	523.6
5.00 in (B.G.)	87.06	10.53	33.08	642.4	575.4
7.75 in (B.G.)	87.31	10.54	33.12	651.7	573.7
10.50 in (B.G.)	81.83	10.21	32.07	544.9	538.4
13.00 in (B.G.)	82.06	10.22	32.11	548.6	541.0
15.50 in (B.G.)	77.99	9.97	31.31	458.0	560.2
18.25 in (B.G.)	82.14	10.23	32.13	509.4	626.5
20.75 in (B.G.)	86.99	10.52	33.06	549.0	714.2
23.50 in (B.G.)	89.63	10.68	33.56	611.7	711.7
26.00 in (B.G.)	90.88	10.76	33.79	601.5	742.3
28.75 in (B.G.)	96.93	11.11	34.90	715.1	787.0
31.25 in (B.G.)	98.13	11.18	35.12	719.0	824.8
33.75 in (B.G.)	100.17	11.29	35.48	753.3	856.7
36.25 in (B.G.)	107.53	11.70	36.76	966.5	891.8
39.00 in (B.G.)	93.39	10.90	34.26	696.6	706.4
41.50 in (B.G.)	97.11	11.12	34.93	759.4	762.3
44 in (B.G.)	100.26	11.30	35.50	797.7	820.0
46.5 in (B.G.)	102.44	11.42	35.88	823.8	868.7
49 in (B.G.)	102.35	11.42	35.86	855.4	833.7
51.5 in (B.G.)	107.53	11.70	36.76	925.7	937.7
54 in (B.G.)	110.09	11.84	37.20	981.1	971.4
56.5 in (B.G.)	113.33	12.01	37.74	1035.1	1029.9
59 in (B.G.)	113.98	12.05	37.85	1055.9	1030.2
61.5 in (B.G.)	106.24	11.63	36.54	942.5	873.9
64 in (B.G.)	112.37	11.96	37.58	1037.6	992.0
66.5 in (B.G.)	116.54	12.18	38.27	1091.3	1090.1
68.75 in (B.G.)	116.91	12.20	38.33	1087.0	1105.4
71.25 in (B.G.)	114.98	12.10	38.01	1072.0	1050.4

Pole 20

Depth	**A** (in^2)	$d_{eff}(in)$	$C_{eff}(in)$	$I_x(in^4)$	$I_y(in^4)$
12 in (A.G.)	64.98	9.10	28.58	333.7	338.8
9 in (A.G.)	65.09	9.10	28.60	336.5	338.2
6.125 in (A.G.)	63.76	9.01	28.31	322.1	333.4
3.5 in (A.G.)	64.05	9.03	28.37	321.7	347.0
0.5 in (A.G.)	61.67	8.86	27.84	293.3	345.0
2.5 in (B.G.)	52.28	8.16	25.63	249.9	241.9
5.50 in (B.G.)	51.58	8.10	25.46	269.4	206.4
8.25 in (B.G.)	53.97	8.29	26.04	300.9	216.2
11.00 in (B.G.)	59.73	8.72	27.40	329.3	292.5
14.00 in (B.G.)	65.53	9.13	28.70	328.5	383.6
16.75 in (B.G.)	68.03	9.31	29.24	370.6	395.5
19.50 in (B.G.)	70.85	9.50	29.84	412.0	409.9
22.25 in (B.G.)	71.78	9.56	30.03	426.4	409.6
25.00 in (B.G.)	73.07	9.65	30.30	441.4	416.8
27.75 in (B.G.)	75.66	9.81	30.83	475.5	441.6
30.50 in (B.G.)	78.00	9.97	31.31	506.8	464.0
33.25 in (B.G.)	79.62	10.07	31.63	534.3	478.0
36.00 in (B.G.)	80.47	10.12	31.80	539.9	493.5
38.75 in (B.G.)	82.13	10.23	32.13	560.5	516.6
41.50 in (B.G.)	82.89	10.27	32.27	573.4	523.9
44.25 in (B.G.)	85.51	10.43	32.78	608.2	558.5
47.00 in (B.G.)	82.20	10.23	32.14	557.5	520.7
49.75 in (B.G.)	86.72	10.51	33.01	621.1	578.6
52.50 in (B.G.)	89.81	10.69	33.59	664.6	621.7
55.25 in (B.G.)	92.72	10.87	34.13	700.1	670.3
58.00 in (B.G.)	94.31	10.96	34.43	730.3	687.8
60.75 in (B.G.)	92.39	10.85	34.07	690.9	670.0
63.50 in (B.G.)	93.97	10.94	34.36	714.6	692.5
66.25 in (B.G.)	94.97	11.00	34.55	726.9	710.6
69.25 in (B.G.)	90.66	10.74	33.75	665.0	645.2
72 in (B.G.)	83.11	10.29	32.32	564.7	536.3

Pole 11

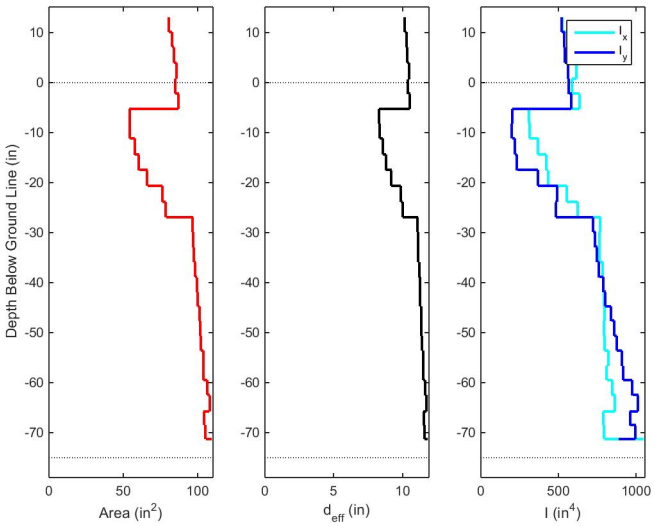

Pole 12

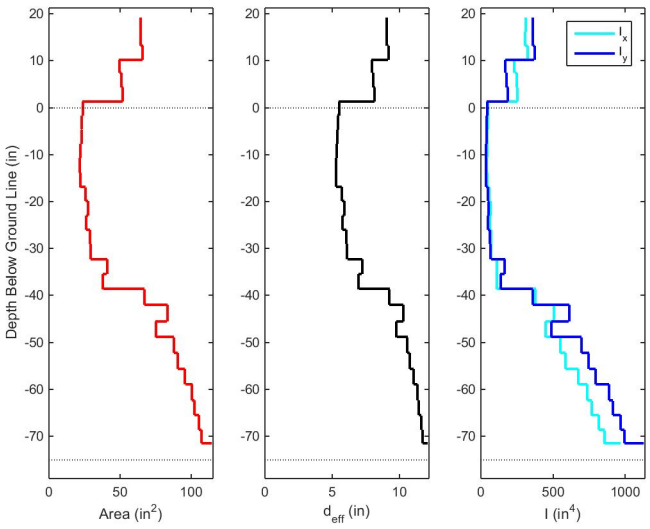

Pole 13

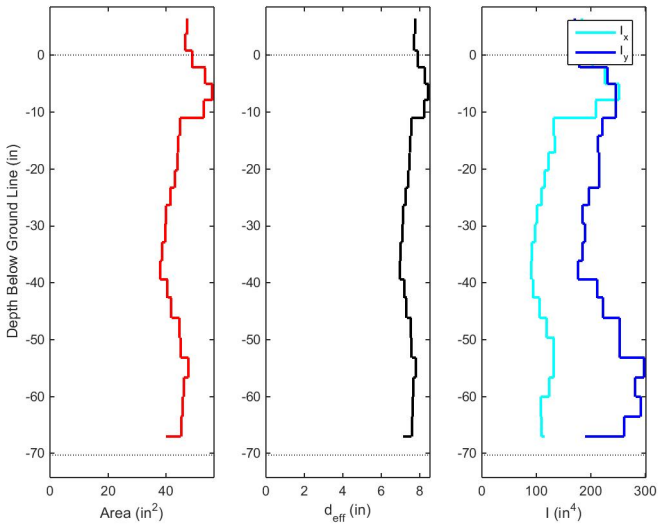

Pole 14

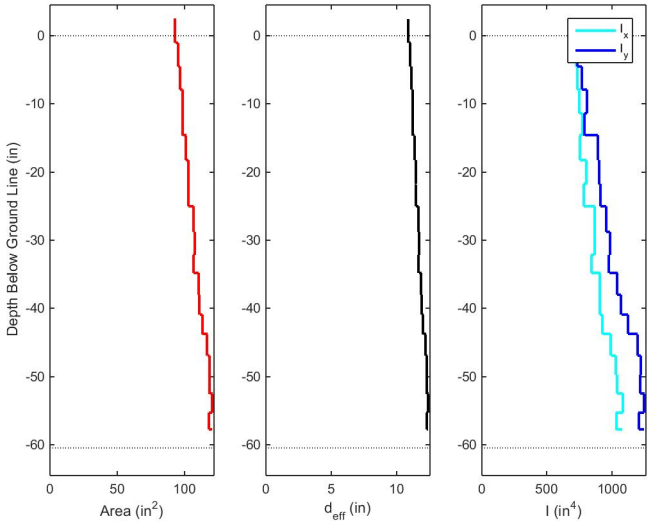

Pole 15

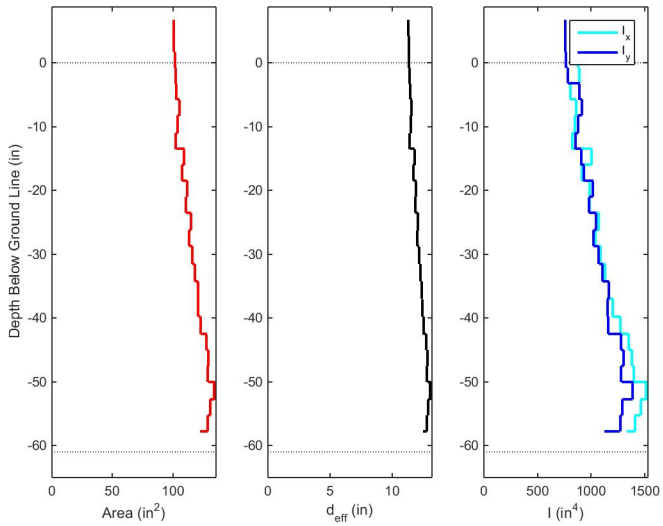

Pole 16

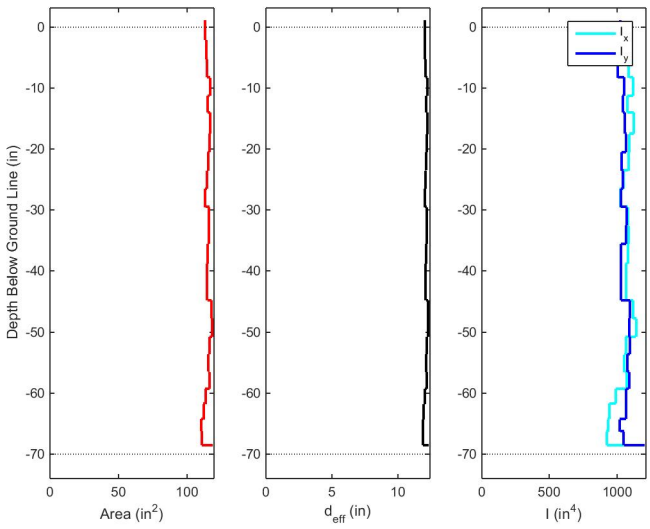

Pole 17

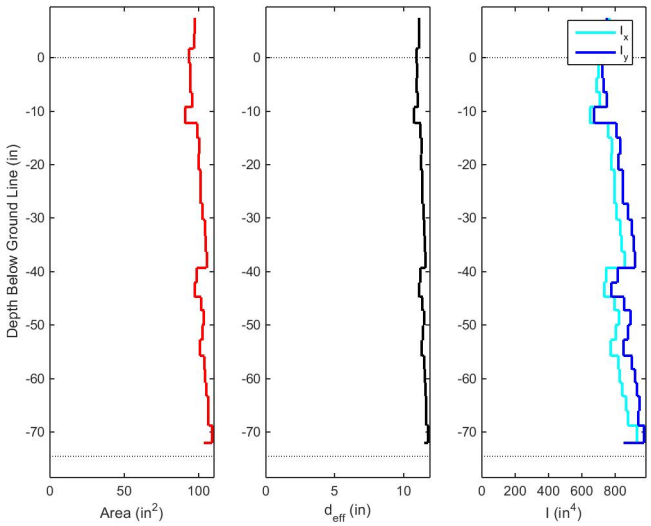

Pole 18

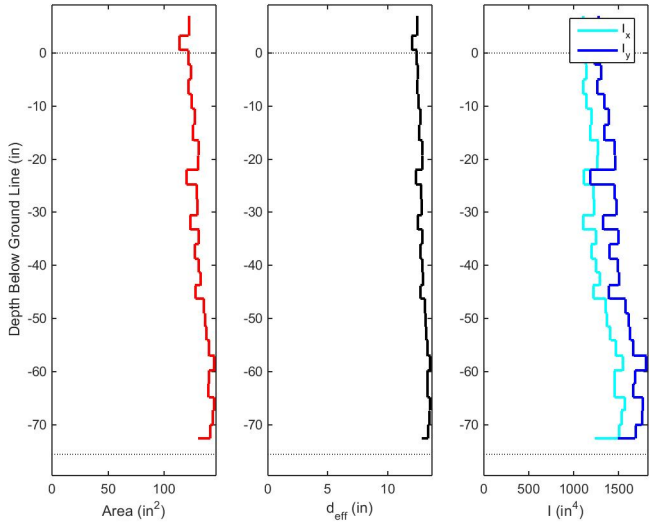

Pole 19

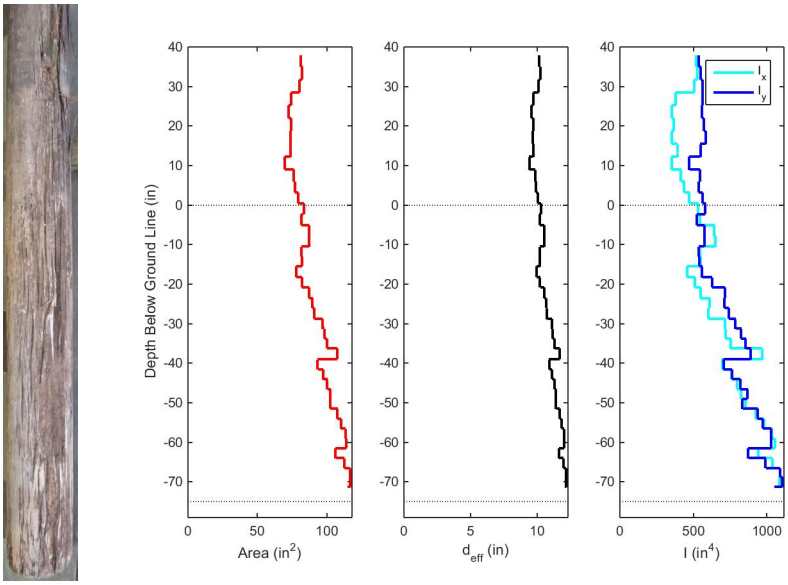

Pole 20

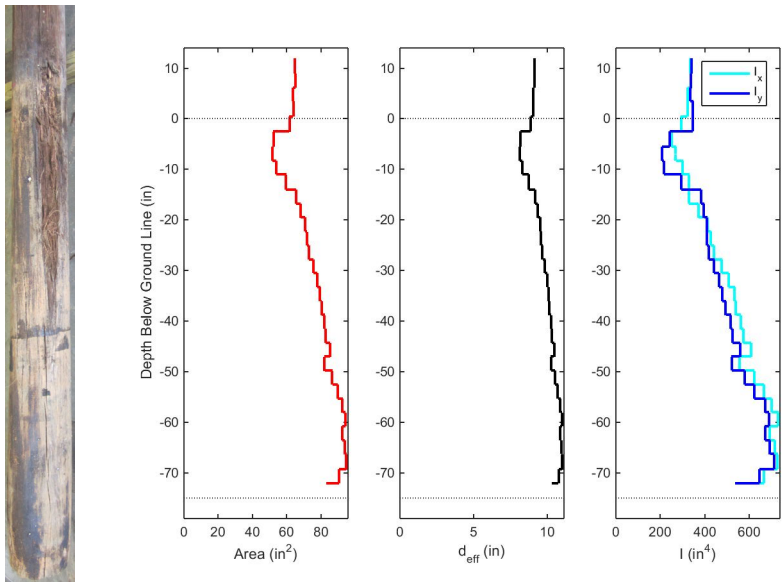

APPENDIX D: SET 1 NATURAL FREQUENCY ESTIMATES

TABLE 10: Experimental estimates of natural frequencies (f_n) and damping ratios (ζ) from Axis 1 excitations

Pole 1			Pole 2			Pole 3		
Mode	f_n **(Hz)**	ζ (%)	**Mode**	f_n **(Hz)**	ζ (%)	**Mode**	f_n **(Hz)**	ζ (%)
1	3.51	9.4	1	2.33	15.0	1	4.12	8.0
2	16.11	3.0	2	13.46	3.2	2	20.15	2.6
3	40.68	2.1	3	36.21	2.4	3	51.53	1.4
4	75.94	3.2	4	68.94	2.0	4	105.59	8.7
5	119.07	7.7	5	110.53	3.1	5	150.75	5.9
6	172.83	3.8	6	156.24	3.4	6	215.01	5.2
7	236.50	3.4	7	210.42	5.0	7	295.55	11.8
8	-	-	8	270.81	6.5	8	-	-

Pole 4			Pole 5			Pole 6		
Mode	f_n **(Hz)**	ζ (%)	**Mode**	f_n **(Hz)**	ζ (%)	**Mode**	f_n **(Hz)**	ζ (%)
1	2.41	26.0	1	3.03	15.9	1	3.63	6.5
2	14.17	2.2	2	15.61	2.6	2	17.85	2.1
3	35.56	1.8	3	41.43	1.7	3	44.62	2.2
4	66.91	2.7	4	79.02	2.4	4	84.23	3.1
5	106.29	4.7	5	122.28	3.4	5	128.66	4.1
6	157.31	3.5	6	180.99	6.5	6	177.11	2.7
7	204.91	5.1	7	250.69	9.1	7	236.74	7.9
8	255.29	4.8	8	-	-	8	-	-

Pole 7			Pole 8			Pole 9		
Mode	f_n **(Hz)**	ζ (%)	**Mode**	f_n **(Hz)**	ζ (%)	**Mode**	f_n **(Hz)**	ζ (%)
1	2.79	5.6	1	2.50	44.0	1	1.66	20.7
2	15.40	2.6	2	14.53	4.9	2	9.08	4.4
3	41.62	1.7	3	40.10	2.7	3	24.87	2.2
4	76.86	1.8	4	75.41	2.2	4	48.15	2.4
5	123.77	3.1	5	123.95	6.4	5	78.28	3.5
6	173.40	2.2	6	153.98	2.1	6	113.93	3.6
7	240.94	3.3	7	-	-	7	154.55	3.8

Pole 10		
Mode	f_n **(Hz)**	ζ (%)
1	2.36	17.9
2	12.13	4.3
3	34.23	3.0
4	63.74	2.2
5	101.84	4.6
6	143.73	4.0
7	194.55	6.9

TABLE 11: Experimental estimates of natural frequencies (f_n) and damping ratios (ζ) from Axis 2 excitations

Pole 1			Pole 2			Pole 3		
Mode	f_n **(Hz)**	ζ (%)	**Mode**	f_n **(Hz)**	ζ (%)	**Mode**	f_n **(Hz)**	ζ (%)
1	3.37	9.2	1	2.32	10.3	1	4.51	17.3
2	15.21	2.2	2	13.35	3.9	2	20.76	3.6
3	39.52	2.3	3	36.04	1.6	3	52.62	3.1
4	79.07	2.3	4	68.49	1.9	4	-	-
5	120.46	10.4	5	108.51	3.2	5	155.88	5.6
6	158.82	2.3	6	157.51	3.2	6	215.58	7.9
7	195.23	2.8	7	211.00	5.1	7	299.27	14.6
8	231.90	3.1	8	279.29	7.0	8	-	-

Pole 4			Pole 5			Pole 6		
Mode	f_n **(Hz)**	ζ (%)	**Mode**	f_n **(Hz)**	ζ (%)	**Mode**	f_n **(Hz)**	ζ (%)
1	2.63	11.4	1	2.89	11.3	1	3.68	9.2
2	13.28	2.6	2	16.05	2.5	2	17.81	1.8
3	35.26	1.7	3	42.40	2.1	3	43.82	2.7
4	67.35	2.8	4	79.88	3.4	4	85.11	3.1
5	105.87	3.6	5	128.78	4.1	5	128.43	6.9
6	153.50	3.6	6	185.82	4.8	6	188.08	3.9
7	206.42	5.0	7	256.41	7.1	7	256.07	14.8
8	266.48	5.0	8	-		8	-	-

Pole 7			Pole 8			Pole 9		
Mode	f_n **(Hz)**	ζ (%)	**Mode**	f_n **(Hz)**	ζ (%)	**Mode**	f_n **(Hz)**	ζ (%)
1	2.82	11.9	1	2.38	24.9	1	1.83	12.7
2	15.74	2.8	2	14.13	3.2	2	9.78	4.2
3	41.27	1.5	3	38.91	2.0	3	26.09	2.3
4	75.52	2.3	4	78.59	1.8	4	50.60	2.1
5	124.88	3.1	5	110.95	1.9	5	80.42	4.8
6	177.42	2.9	6	154.78	4.5	6	117.22	3.7
7	243.75	3.8	7	-	-	7	158.49	3.9

Pole 10		
Mode	f_n **(Hz)**	ζ (%)
1	2.10	12.3
2	12.32	3.2
3	33.76	2.3
4	65.82	2.6
5	104.08	3.1
6	148.37	3.5
7	193.75	4.8

Pole 10

3.375 in. Above Ground

0.125 in. Above Ground

3.0 Below Ground

6.25 in. Below Ground

9.375 in. Below Ground

13.375 in. Below Ground

17.125 in. Below Ground

20.875 in. Below Ground

25.5 in. Below Ground

29.625 in. Below Ground

34.375 in. Below Ground

39.125 in. Below Ground

43.75 in. Below Ground 48.125 in. Below Ground 52.625 in. Below Ground

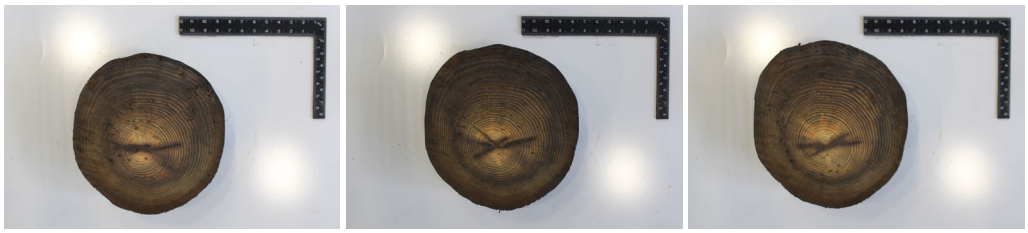

57.125 in. Below Ground 61.75 in. Below Ground 66.125 in. Below Ground

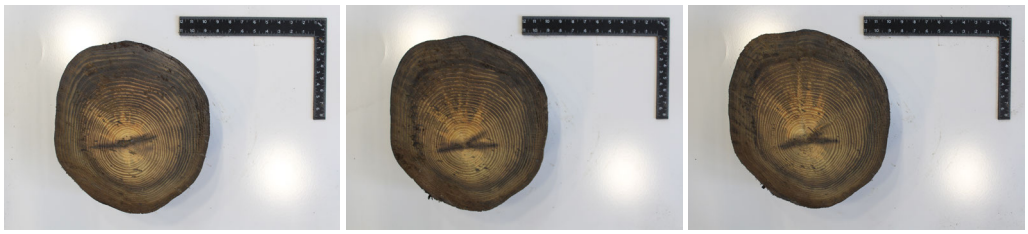

70.5 in. Below Ground 74.75 in. Below Ground 79.0 in. Below Ground

Pole 11

4.875 in. Above Ground

1.75 in. Above Ground

1.25 Below Ground

4.375 in. Below Ground

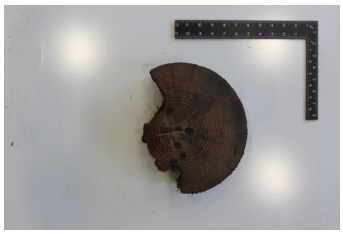

7.75 in. Below Ground

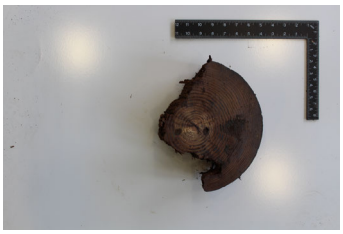

10.125 in. Below Ground

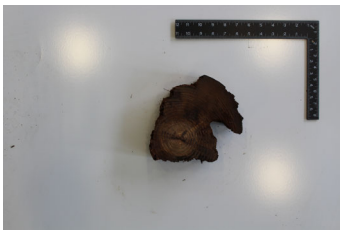

13.0 in. Below Ground

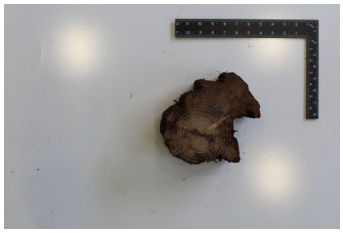

16.125 in. Below Ground

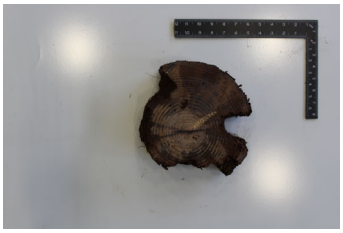

19.625 in. Below Ground

22.875 in. Below Ground

26.0 in. Below Ground

29.125 in. Below Ground

32.25 in. Below Ground

35.375 in. Below Ground

38.375 in. Below Ground

41.5 in. Below Ground

44.625 in. Below Ground

47.875 in. Below Ground

51.5 in. Below Ground

54.5 in. Below Ground

57.625 in. Below Ground

60.625 in. Below Ground

63.5 in. Below Ground

66.375 in. Below Ground

68.5 in. Below Ground 69.875 in. Below Ground 72.5 in. Below Ground

Pole 14

0.875 in. Above Ground

4.0 in. Below Ground

8.5 Below Ground

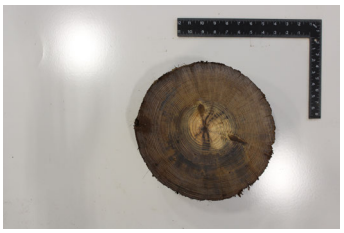

13.375 in. Below Ground

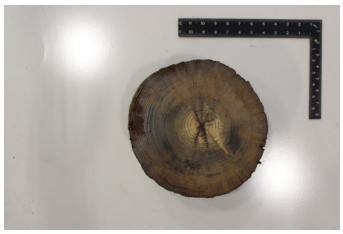

17.375 in. Below Ground

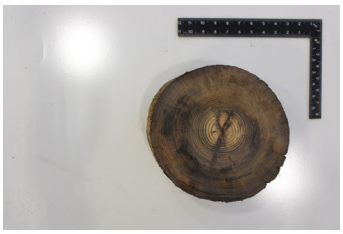

21.125 in. Below Ground

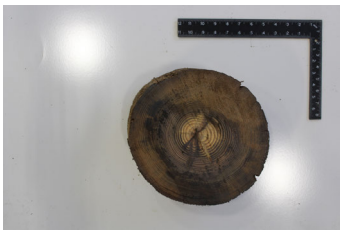

25.375 in. Below Ground

29.625 in. Below Ground

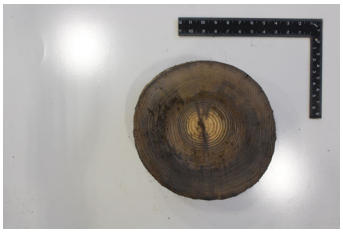

34.125 in. Below Ground

38.25 in. Below Ground

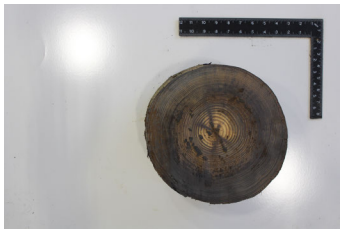

42.5 in. Below Ground

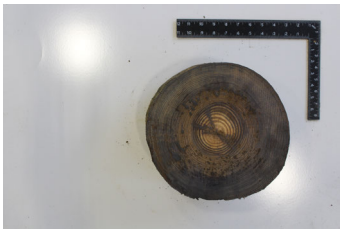

46.75 in. Below Ground

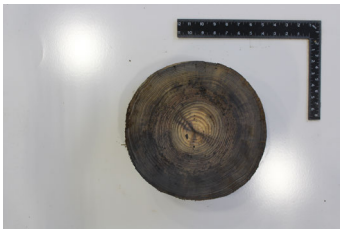

50.625 in. Below Ground

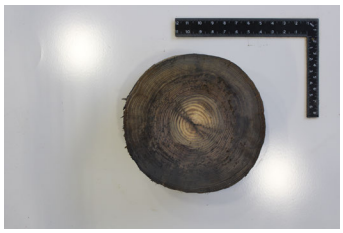

54.375 in. Below Ground

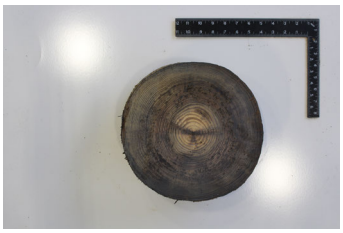

57.625 in. Below Ground

61.5 in. Below Ground

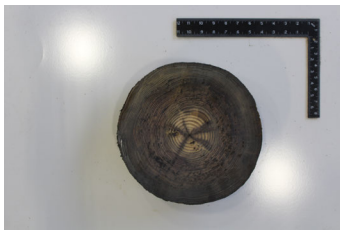

64.75 in. Below Ground

67.875 in. Below Ground

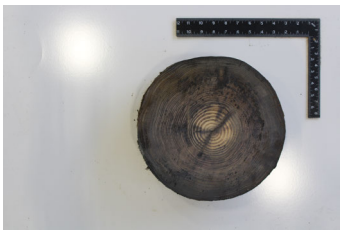

70.875 in. Below Ground

74.75 in. Below Ground

78.125 in. Below Ground